Mechanistic Insights for Magnetic Imaging and Control of Cellular Function

Thesis by
Hunter C Davis

In Partial Fulfillment of the Requirements for the
degree of
Doctor of Philosophy in Chemistry

CALIFORNIA INSTITUTE OF TECHNOLOGY
Pasadena, California

2020
(Defended September 30, 2019)

Hunter C Davis
ORCID: 0000-0003-1655-692X

ACKNOWLEDGEMENTS

No man is an island, least of all me. My work was made possible by the incredible scientific ecosystem that has supported me for the last five years. The nexus of this support was my advisor, Professor Mikhail Shapiro. Mikhail, I will never be able to thank you for taking a chance on a student who confessed in your first meeting that he knew nothing about biology. Your curiosity and grounded optimism inspire my own, pushing me to explore deep and impactful questions while regulating the more stochastic tendencies of my intellect. Thank you for valuing my insight and providing corrective guidance when I lose track of the larger scientific picture. I take profound pride in having worked with you from the early stages of your now burgeoning lab. I am also deeply grateful to Professor Greg Engel, who gave me a chance to prove myself as an undergraduate researcher when I knew less than nothing. Providing me with substantial independence early in my scientific career cultivated my confidence in device fabrication which has become a cornerstone of my research. I'm additionally indebted to Professor Markus Meister. Markus, I am incredibly grateful for your guidance and support over the past few years as we struggled to correct the scientific record. I hope that you feel, as I do, that it has been worth the headache. Exceptional claims require exceptional evidence. Thank you for helping to enforce that requirement. While the full list of my scientific mentors is too long to tell, I would also like to thank Professor Thomas Miller and Professor Scott Cushing for sitting on my thesis committee and for their continued council.

On my first day of undergraduate study, I stepped into a physics lecture mortified at my ill-preparedness for the challenges ahead. It was in this state of horror that I met Tankut Can, a TA who took the time to help me fill in the gaps in my knowledge that would have otherwise stalled my scientific career before it began. It is in a similar vein that I acknowledge Professor Graham Griffin, who spent years teaching me practical optics when I was an undergraduate researcher. His patience with my hours of questions as we built complex optical systems astounds me to this day, and I would not be the scientist I am today without his generosity.

It is hard to imagine what my doctoral work would have been like without the exceptional people in the Shapiro Group. The driven and intellectually curious environment

we built has given me a sense of community that I never thought was possible. It has been an incredible privilege to explore strange new ideas with you. You're my team. I am particularly grateful to Pradeep Ramesh, who I count among my dearest friends and most impressive colleagues. Thank you for recruiting me into the group and guiding me through my early days in biology. I am also grateful to my dear friend and next-door neighbor in the office, Arash Farhadi. You've made it so much fun to come into the office for the past few years. Thanks for always being willing to spend a few hours on an intellectual tangent. Many of the best ideas I've had have come out of our circuitous talks. An additional thanks is due for your constant willingness to travel with me through the joy, sadness, and frustration that pervades the daily life of graduate research. I have also been blessed by wonderful support from friends outside of the lab, chief among them being Alysha de Souza. Lysh, thank you for always being available to grab a cup of coffee and talk about the world. I'll miss our protracted discussions about science, politics, and life, but I know we'll find a way to stay in each other's orbit.

Finally, I would like to thank my family, without whom none of this is possible. Mom and Dad, I don't know how you managed to parent me when you were both still children, but you excelled. My early childhood was filled with love and encouragement. As my time as a student comes to an end, I'm reminded of your continued dedication to giving me every educational opportunity. My gratitude is boundless. Parker, I am so proud to be your brother. Your strength through challenges that I cannot fathom inspires me. Thank you for being my constant friend. Katherine, you have been my friend since we were teenagers, my partner since 2015, and my wife since that beautiful October night. I am who I am today because of you. Our creative harmony is a continuous source of joy, and your positivity brings a smile to my face on even my most frustrating days. Being the partner of a scientist comes with a unique set of challenges, and you handle them all with grace. I cannot wait to continue exploring the world with you.

ABSTRACT

The vast biomolecular toolkit for optical imaging and control of cellular function has revolutionized the study of *in vitro* samples and superficial tissues in living organisms but leaves deep tissue unexplored. To look deeper in tissue and observe system-level biological function in large organisms requires a modality that exploits a more penetrant form of energy than visible light. Magnetic imaging with MRI reveals the previously unseen, with endogenous tissue contrast and practically infinite penetration depth. While these clear advantages have made MRI a cornerstone of modern medical imaging, the sparse library of molecular agents for MRI have severely limited its utility for studies of cellular function *in vivo*. The development of new molecular agents for MRI has suffered from a lack of tools to study the connection between changes in the microscale cellular environment and the corresponding millimeter-scale MRI contrast. Bridging this gap requires revisiting the mechanistic underpinnings of MRI contrast, casting aside some of the simplifications that smooth over sub-voxel heterogeneity that is rich with information pertinent to the underlying cell state.

Here, we will demonstrate theoretical, computational, and experimental connections between subtle changes in microscale cellular environment and resultant MRI contrast. After reviewing some foundational principles of MRI physics in the first chapter, the second chapter of the thesis will explore computational models that have significantly enhanced the development of genetically encoded agents for MRI, including the first genetically encoded contrast agent for diffusion weighted imaging. By improving the efficacy of these genetically encoded agents, we unlock MRI reporter genes for *in vivo* studies of cellular dynamics much

in the same way that the engineering of Green Fluorescent Protein has dramatically improved *in vitro* studies of cellular function.

In the third chapter, we introduce our study that maps microscale magnetic fields in cells and tissues and connects those magnetic fields to MRI contrast. Such a connection has previously been experimentally intractable due to the lack of methods to resolve small magnetic perturbations with microscale resolution. To overcome this challenge, we leverage nitrogen vacancy diamond magnetometry to optically probe magnetic fields in cells with sub-micron resolution and nanotesla sensitivity, together with iterative localization of field sources and Monte Carlo simulation of nuclear spins to predict the corresponding MRI contrast. We demonstrate the utility of this technology in an *in vitro* model of macrophage iron uptake and histological samples from a mouse model of hepatic iron overload. In addition, we show that this technique can follow dynamic changes in the magnetic field occurring during contrast agent endocytosis by living cells. This approach bridges a fundamental gap between an MRI voxel and its microscopic constituents and provides a new capability for noninvasive imaging of opaque tissues.

In the fourth chapter, we focus on the use of magnetic fields to perturb, rather than image, biological function. Recent suggestions of nanoscale heat confinement on the surface of synthetic and biogenic magnetic nanoparticles during heating by radiofrequency alternating magnetic fields have generated intense interest due to the potential utility of this phenomenon in non-invasive control of biomolecular and cellular function. However, such confinement would represent a significant departure from classical heat transfer theory. We present an experimental investigation of nanoscale heat confinement on the surface of several types of iron oxide nanoparticles commonly used in biological research, using an all-optical

method devoid of potential artifacts present in previous studies. By simultaneously measuring the fluorescence of distinct thermochromic dyes attached to the particle surface or dissolved in the surrounding fluid during radiofrequency magnetic stimulation, we found no measurable difference between the nanoparticle surface temperature and that of the surrounding fluid for three distinct nanoparticle types. Furthermore, the metalloprotein ferritin produced no temperature increase on the protein surface, nor in the surrounding fluid. Experiments mimicking the designs of previous studies revealed potential sources of artifacts. These findings inform the use of magnetic nanoparticle hyperthermia in engineered cellular and molecular systems and can help direct future resources towards tractable avenues of magnetic control of cellular function.

PUBLISHED CONTENT AND CONTRIBUTIONS

Davis, H.C. et al. (2019). “Nanoscale fluorescent thermometry of magnetic nanoparticles and ferritin in an alternating magnetic field” *In preparation*.

HCD and MGS conceived the study. HCD designed the experiments, collected and analyzed the data, and wrote the *in silico* model for particle clustering. HCD and MGS prepared the manuscript.

Davis, H.C.[†] , Ramesh, P.[†] et al. (2018). “Mapping the microscale origins of MRI contrast with sub-cellular NV magnetometry”. In: Nature Communications 9, 131. doi:10.1038/s41467-017-02471-7

([†]Equal Contribution)

HCD conceived the study with PR, acquired and processed all optical magnetometry data, designed the Monte Carlo simulations with help from AB, performed the MRI experiments with PR, and prepared the manuscript with PR and MGS.

Mukherjee, A, Wu, D, **Davis, H.C.**, Shapiro, M.G. (2016) “Non-invasive imaging using reporter genes altering cellular water permeability” In: Nature Communications 7,13891. doi:10.1038/ncomms13891

HCD, AM, and MGS established the physical model for relaxation. HCD designed the Monte Carlo model for diffusion and signal attenuation and participated in the preparation of the manuscript.

Ramesh, P., Hwang, S.J., **Davis, H.C** et al. (2018). “Ultraparamagnetic Cells Formed through Intracellular Oxidation and Chelation of Paramagnetic Iron”. In: Angewandte Chemie Internation Edition 57, pp. 12385-12389. doi: 10.1002/anei.201805042

HCD worked with PR to establish the physical model for transverse relaxation. HCD designed the Monte Carlo simulations with help from VI.

Mukherjee, A, **Davis, H.C**., et al. (2017). “Biomolecular MRI reporters: evolution of new mechanisms”. In: Progress in Nuclear Magnetic Resonance Spectroscopy, 102-103, pp. 32-42. doi: 10.1016/j.pnmrs.2017.05.002

HCD participated in the preparation of the manuscript.

Piranar, D, Farhadi, A, **Davis, H.C.** et al. (2017). “Going Deeper: Biomolecular Tools for Acoustic and Magnetic Imaging and Control of Cellular Function” In: Biochemistry 56(39): pp. 5202-5209. doi: 10.1021/acs.biochem.7b00443

HCD participated in the preparation of the manuscript

TABLE OF CONTENTS

LIST OF FIGURES

Figure *Page*

Chapter 1

FOUNDATIONAL PHYSICS OF MAGNETIC RESONANCE IMAGING

1.1 Introduction

Owing to the noninvasiveness and practically unlimited penetration depth of magnetic fields in tissue, magnetic resonance imaging (MRI) has become a staple of biological imaging for medical and research applications. By providing strong anatomical contrast, it gives radiologists and researchers millimeter-scale insights into the magnetic behavior of water in tissue, which can be sensitized to a variety of biologically relevant parameters including brain activity [1], iron content [2], water diffusion [3], and axonal tract orientation [4], all without the addition of contrast agents. However, the relative dearth of molecular reporters for MRI compared to fluorescent imaging has significantly limited its utility for studies of the genetic and molecular states of cells. Among the principal limitations for the development of these molecular agents is the large mismatch between micron-level length scale that is relevant for biomolecular and cellular interactions and the millimeter resolution of MRI. Much of this thesis will focus on bridging this gap by exploring the microscale origins of MRI contrast. In this chapter, we provide a brief introduction to the foundational physics of nuclear magnetic resonance and relaxation, with a focus on how molecular interactions, microscale magnetic fields, and water diffusion all contribute to MRI contrast. While it is by no means an exhaustive summary, it provides an intuitive model for understanding the magnetic relaxation of water-bound protons that will be instructive for understanding the remainder of this thesis and advancing the burgeoning field of biomolecular reporters for MRI [5, 6].

1.2 The magnetic behavior of nuclear spins

MRI signal is derived from nuclear magnetic resonance (NMR), a spin-state transition resonance for the magnetic moment of nuclei. For most biological cases, the nuclei of interest are protons bound to water in tissue. As protons have spin angular momentum S=1/2, their magnetization operator can be defined by:

$$\hat{\boldsymbol{m}} = \gamma \hat{\boldsymbol{S}}$$

Here γ is the gyromagnetic ratio for the proton and $\hat{\boldsymbol{S}}$ is the spin angular momentum operator, which has components in x, y, and z given by:

$$\hat{S}_z = \frac{\hbar}{2}\begin{pmatrix} 1 & 0 \\ 0 & -1 \end{pmatrix}, \hat{S}_y = \frac{\hbar}{2}\begin{pmatrix} 0 & i \\ i & 0 \end{pmatrix}, \hat{S}_x = \frac{\hbar}{2}\begin{pmatrix} 0 & 1 \\ 1 & 0 \end{pmatrix}$$

The hamiltonian of a magnetic dipole in an externally applied magnetic field $\boldsymbol{B}$ is given by

$$\hat{H} = -\hat{\boldsymbol{m}} \cdot \boldsymbol{B}$$

In NMR and MRI, a strong bias field B_0 is applied, and the direction of this field is taken by convention to be in the +z direction. Thus,

$$\hat{H} = -\hat{m}_z B_0 = -\gamma \hat{S}_z B_0 = -\frac{\gamma \hbar B_0}{2}\begin{pmatrix} 1 & 0 \\ 0 & -1 \end{pmatrix}$$

The orthonormal basis for this hamiltonian is formed by two states, $|+\rangle = \begin{pmatrix} 1 \\ 0 \end{pmatrix}$ and $|-\rangle = \begin{pmatrix} 0 \\ 1 \end{pmatrix}$, with energy levels $H|\pm\rangle = \mp\frac{\gamma\hbar B_0}{2}$. This magnetic field dependent energy splitting of these spin states is known as Zeeman splitting and causes a preferential alignment of the magnetic moment of the proton with the magnetic field. An arbitrary state in this system can be written as $|\psi\rangle = a|+\rangle + b|-\rangle = \begin{pmatrix} a \\ b \end{pmatrix}$. Under normal circumstances, the Zeeman energy splitting is much less than the thermal energy of the system ($\Delta E_{Zeeman} \ll k_B T$), and as a result, the excess alignment of proton magnetic moments along the bias field is only a few protons per million. In thermal equilibrium, the density matrix for this two-level system is:

$$\rho = \begin{pmatrix} \frac{1}{2} + \frac{\hbar\gamma B_0}{4kT} & 0 \\ 0 & \frac{1}{2} - \frac{\hbar\gamma B_0}{4kT} \end{pmatrix}$$

As would be expected, the off-diagonal terms representing superposition states are zero at thermal equilibrium and as a result, so too are the expectation values of the magnetization in the x and y dimensions.

1.3 The Bloch model and Nuclear Magnetic Resonance

As demonstrated by Richard Feynman in his landmark paper on two-level systems [7], the dynamics of the expectation value of the magnetization of an isolated nuclear spin in a magnetic field can be calculated using the Liouville equation for quantum mechanical observables:

$$\frac{d}{dt}\langle\widehat{\boldsymbol{m}}\rangle = \frac{1}{i\hbar}\left\langle\left[\widehat{\boldsymbol{m}}, \widehat{H}\right]\right\rangle = \gamma\langle\widehat{\boldsymbol{m}}\rangle \times \boldsymbol{B}$$

This solution is equivalent to the equation of motion for a classical magnetic dipole **m** with intrinsic angular momentum **S** in a magnetic field **B**. If the magnetic moment of the dipole is $\boldsymbol{m} = \gamma\boldsymbol{S}$, it will experience a torque $\boldsymbol{\tau} = \boldsymbol{m} \times \boldsymbol{B}$**.** The equation of motion for $\boldsymbol{m}$ is thus,

$$\frac{d\boldsymbol{m}}{dt} = \frac{d(\gamma\boldsymbol{S})}{dt} = \gamma(\boldsymbol{\tau}) = \gamma\boldsymbol{m} \times \boldsymbol{B}.$$

Qualitatively, this equation predicts that the magnetic moment will precess about the applied magnetic field $\boldsymbol{B}$ with a precession frequency $\omega = \gamma B$. For the precession of the magnetic moment of nuclei, this process is called Larmor precession and the frequency ω is called the Larmor frequency. Felix Bloch demonstrated the predictive power of this intuitive semi-classical model for

NMR, and it is still widely used today [8]. We will rely heavily on Bloch's simple model for the remainder of this thesis.

1.4 RF Pulses and Rotating Reference Frames

As the transverse component of the magnetic moment of a water bound proton in a strong bias field is zero at equilibrium, a perturbation is necessary to induce precession. Let's examine the response of our semi-classical model of a proton magnetic dipole $\boldsymbol{m}$ in a strong longitudinal bias field $\boldsymbol{B_0}$ to a second magnetic field $\boldsymbol{B_1}$ applied orthogonal to $\boldsymbol{B_0}$. If $\boldsymbol{B_1}$ is constant and much weaker than $\boldsymbol{B_0}$, there will be no net effect as the precession of the dipole around the $\boldsymbol{B_0}$ field will average out any torque applied by $\boldsymbol{B_1}$ in a single revolution. If instead our magnetic perturbation is an oscillating field $\boldsymbol{B_1} = 2B_1 \sin(\omega_0 t + \phi)\,\hat{\boldsymbol{y}}$ the proton magnetic moment will tip off of the z axis. RF excitations are generally referred to by magnitude of the induced rotation of the nuclear spin with the angle $\theta = t\gamma B_1$. If the oscillating field is held on for $t = \frac{\pi}{2\omega_1}$ where $\omega_1 = \gamma B_1$, a magnetic moment that starts aligned with the B_0 bias field will be rotated into the xy plane, where it will precess at the Larmor frequency ω_0, driven by the torque from B_0. The precession of an ensemble of nuclear magnetic dipole moments in the transverse plane will form an AC magnetic signal that can be measured by way of an induced voltage on a receiver coil according to Farraday's law [9].

This picture is greatly simplified in a rotating reference frame that rotates at a frequency equal to the Larmor precession frequency in the transverse plane. If we decompose the linearly polarized $\boldsymbol{B_1}$ field into an equal sum of two counter-rotating circularly polarized fields rotating at $\omega_{RF} = \omega_0 = \gamma B_0$ in the lab frame, one of these fields will be static in the rotating reference frame and the other will rotate at $-2\omega_{RF}$. As the $-2\omega_{RF}$ field has a mean zero effect on the dipole, only the static field in the rotating frame contributes to the rotation of the dipole. The rotation of the nuclear dipole in this perturbing field is then simply a rotation around the y axis, with rotation frequency $\omega_1 = \gamma B_1$. Once in the transverse plane, a magnetic dipole precessing at the Larmor frequency $\omega_0 = \gamma B_0$ will remain static.

1.5 Phenomenological relaxation equations

The excitation of an ensemble of nuclear spins by a perturbing $\boldsymbol{B_1}$ field generates only a transient perturbation to the equilibrium magnetic state. The perturbation to the longitudinal magnetization (m_z) of our spin ensemble will relax to the thermal equilibrium through a process known as *spin-lattice relaxation* with a characteristic time T_1 such that after an RF pulse rotates the magnetic moment of the proton into the transverse plane,

$$M_z(t) = M_0(1 - e^{-\frac{t}{T1}}).$$

Immediately after the RF pulse is applied, the magnetic moments of the spins inside of a given ensemble will precess in phase around B_0. The precession of these spins will decohere over time and as a result, the transverse magnetization will relax to zero with a characteristic time T_2 such that

$$M_{xy} = \sqrt{M_x^2 + M_y^2} = M_0 e^{-\frac{t}{T2}}$$

Both the longitudinal and transverse relaxation times are heavily affected by the chemical and magnetic environment experienced by the water-bound protons and combined they represent the basis of image contrast in MRI. The model of Felix Bloch was adapted with phenomenological terms to account for these relaxation dynamics and the effects of water diffusion in the Bloch-Torrey Equation [10]:

$$\frac{d\boldsymbol{M}}{dt} = \gamma \boldsymbol{M} \times \boldsymbol{B} - D\nabla^2 \boldsymbol{M} - \frac{\boldsymbol{M_x} + \boldsymbol{M_y}}{T_2} - \frac{\boldsymbol{M_z} - \boldsymbol{M_0}}{T_1}$$

Here D is the diffusion constant for the nuclei of interest. This simple equation is incredibly powerful for predicting the magnetic response of a large ensemble of water molecules in a homogeneous environment to an exogenously imposed magnetic field and is extensively used as a first pass approximation for everything from basic pulse sequence design to advanced techniques like compressed sensing and MRI fingerprinting[11]. However, the phenomenological relaxation parameters are of limited utility for molecular-scale insights without significant further development. In the remainder of this chapter, I will examine the molecular magnetic perturbations that undergird the relaxation of water-bound protons in MRI, demonstrating the pitfalls of assuming phenomenological relaxation rates on the millimeter scale along the way.

1.6 Longitudinal ($\boldsymbol{T_1}$) Relaxation

While this thesis will heavily focus on the rich physical underpinnings of transverse (T_2) relaxation, it is also useful to consider the significance of longitudinal relaxation both for understanding the magnetodynamcis of the water-bound proton and the significant practical applications of molecular agents that enhance T_1 contrast for research and clinical applications.

1.6.1 Relaxation of pure water

In order to re-establish the Boltzmann distribution of spin states for protons in a fluid after our perturbing $\boldsymbol{B_1}$ field rotates them into the transverse plane, the magnetic dipoles need a mechanism to couple to the surrounding heat bath. We can immediately eliminate the direct emission or absorption of thermal radiation as a candidate as the lifetime for such a process would be on the order of 10^{22} seconds [12]. While magnetic quadrapolar interactions could be relevant for larger nuclei, they are zero for spin ½ particles like protons, and as a result there is no coupling between the electric field environment and the magnetic dipole of the proton. This leaves only the magnetic field produced by sources inside of the lattice as a mechanism to couple to the bath. As discussed during the introduction to excitation RF pulses, exciting changes in the longitudinal magnetization requires a perturbing magnetic field that is resonant with the Larmor precession frequency of the proton in the bias field. In pure water, this perturbing field can be generated by the Brownian motion of neighboring water-bound protons. This dipolar coupling with neighboring molecules scales as $\frac{1}{r^6}$ where r is the distance between the two molecules, so it is a very near-field interaction. In the case of water, each proton has a corresponding partner bound to the same molecule. The precession of this nearest neighbor proton combined with the tumbling of the water molecule leads to a complex spectral density of magnetic field dependent both on the Brownian motion of the water and on the magnetic dynamics of the proton. Using these relationships, Bloembergen, Purcell, and Pound came up with a simple model for predicting the T_1 relaxation rate of a water-bound proton due only to this nearest neighbor proton [12]. This solution is referred to as the BPP equation for longitudinal relaxation and states:

$$\frac{1}{T_1} = \frac{3}{10}\left(\frac{\gamma^4\hbar^2}{b^6}\right)\left[\frac{\tau_c}{1 + 4\pi^2\nu_0^2\tau_c^2} + \frac{2\tau_c}{1 + 16\pi^2\nu_0^2\tau_c^2}\right]$$

Here b is the interproton distance, ν_0 is the Larmor frequency of the proton in Hz (~42.58 MHz/Tesla), and τ_c is the correlation time for the orientation of the molecule. In pure water at 20° C, the correlation time is around 3.5 ps, so $16\pi^2\nu_0^2\tau_c^2 \ll 1$ and $\frac{1}{T_1} = .19\ s^{-1}$. In this regime, the longitudinal relaxation rate from the nearest neighbor proton is proportional to the correlation time of the water molecule. Here we can already see that the molecular environment can dramatically affect the magnetic relaxation dynamics as water molecules coordinated to macromolecules will have a substantially increased correlation time. This relaxation rate is maximized when

$$\omega_0 \cdot \tau_c = \frac{1}{\sqrt{2}}.$$

The contribution of neighboring water molecules to the relaxation of a water bound proton can also be calculated as:

$$\frac{1}{T_1} = \frac{9\pi^2\gamma^4\hbar^2\eta N_0}{5k_B T}$$

Here N_0 is the number density of water molecules and η is the viscosity of the fluid. In pure water at 20° C, this corresponds to $\frac{1}{T_1} = .1\ s^{-1}$. This implies that the majority of the longitudinal magnetic relaxation for a proton in pure water comes from the partner proton bound to the same water molecule. Combining the two relaxation rates, the predicted T_1 for pure water comes to 3.4 seconds, which corresponds well with experimental values [13].

1.6.2 Relaxation from interaction with paramagnetic molecules

The addition of paramagnetic species to a water sample can significantly enhance the T_1 relaxation rate. As the gyromagnetic ratio of the electron is much greater than that of the proton, the magnetic moment of unpaired electrons in paramagnetic solutes is much higher than water-bound protons. As a result, longitudinal relaxation from intermolecular magnetic dipolar coupling of an unpaired electron to a water-bound proton is much more intense than between protons on neighboring water molecules. In addition to this “through-space” relaxation effect, paramagnetic centers can contribute to relaxation via a “through-bond” mechanism, wherein a water molecule coordinates to a metal chelating molecule and brings its proton close enough to couple its spin with the spin of the unpaired electron (J-coupling). This coupling allows for direct spin exchange between the electron and the proton, enhancing the equilibration of the proton spin temperature to the temperature of the bath.

The quantitative model for the combined relaxation enhancement from a paramagnetic center is described by the Solomon-Bloembergen-Morgan (SBM) equations [12].

$$\frac{1}{T_1} = \frac{P_M q}{T_{1M} + \tau_M}$$

Here T_{1M} is the relaxation rate of water molecules bound to a site near the metal ion, τ_M is the residence lifetime of water bound to a site near the metal ion, P_M is the mole fraction of metal ions, and q is the number of coordination sites for water per metal ion. The relaxation rate for coordinated water can be approximated by [12 14]:

$$\frac{1}{T_{1M}} = \frac{2}{15}\left(\frac{\gamma_I^2 g^2 S(S+1)\beta^2}{r^6}\right)\left[\frac{7\tau_c}{1+\omega_S^2\tau_c^2} + \frac{3\tau_c}{1+\omega_I^2\tau_c^2}\right] + \frac{2}{3}S(S+1)\left(\frac{A}{\hbar}\right)^2\left[\frac{\tau_e}{1+\omega_S^2\tau_c^2}\right]$$

$$\frac{1}{\tau_e} = \frac{1}{T_{1e}} + \frac{1}{\tau_M}$$

Here,γ_I is the proton gyromagnetic ratio, g is the electronic g-factor, S is the total electron spin of the metal ion, β is the Bohr magneton, r is the distance between the water-bound proton and the metal ion, ω_S is the electronic Larmor precession frequency of the metal ion, ω_I is the proton Larmor precession frequency, $\frac{A}{\hbar}$ is the electron-nuclear hyperfine coupling constant, and τ_c is the correlation time of the magnetic field experienced by the water-bound proton given by:

$$\frac{1}{\tau_c} = \frac{1}{T_{1e}} + \frac{1}{\tau_M} + \frac{1}{\tau_R}$$

Here, T_{1e} is the longitudinal relaxation time of the electron on the paramagnetic center and τ_R is the rotational tumbling time of the water-bound paramagnetic complex.

As with spin-lattice relaxation, we expect the maximum enhancement in longitudinal relaxation rate (minimum T_1) to occur when $\frac{1}{\tau_c}$ is near the Larmor frequency for the nucleus in the bias field ($\boldsymbol{B_0}$).

The vast majority of T_1 contrast agents are small molecules with paramagnetic metal centers like gadolinium. As a result, the rate of molecular tumbling $(\frac{1}{\tau_R})$ tends to dominate the correlation time, with $\tau_R \approx .1\, ns$, $T_{1e} \approx$ .54 ns, and $\tau_M \approx 1\, \mu s$ at 20° C and in a 2 Tesla bias field [15, 16]. Improved T1 agents with substantially increased molecular tumbling time have been developed that use protein macromolecules with paramagnetic metal centers as T1 agents. These agents have proven particularly effective for low-field MRI, where the low proton Larmor frequency requires T_1 contrast agents with long correlation times [17, 18].

1.7 Transverse (T_2) relaxation

Transverse relaxation is driven by a dephasing of the precession of the magnetic dipoles of an ensemble of water-bound protons. After perturbing an ensemble of these dipoles that reside in a homogeneous static field with a resonant $\boldsymbol{B_1}$ field that tips the magentizations into the transverse plane, the dipoles will begin to precess in-phase with each other and will generate a macroscopic and measurable signal:

$$S(t) = S_0 \cos(\omega_0 t)$$

The coherence of precession of the dipoles will tend to decay overtime, with the expectation value for the transverse magnetization exponentially decaying to zero with the time constant T_2. This decoherence is principally driven by inhomogeneities in the local field experienced by the different protons inside of a solution. Much like T_1 relaxation, an ensemble of water molecules can decohere each other by providing a random perturbing field. It is worth noting at this point that while T_1 relaxation will always induce T_2 relaxation, it is possible to achieve T_2 relaxation without T_1

relaxation. The rate of this T_2 decay for pure water is given by the BPP equation for transverse relaxation [12]:

$$\frac{1}{T_2} = \frac{3\gamma^4\hbar}{20r^6}\left[3\tau_c + \frac{5\tau_c}{1+\omega_0^2\tau_c^2} + \frac{2\tau_c}{1+4\omega_0^2\tau_c^2}\right]$$

While BPP theory can be instructive for understanding T_1 relaxation, it suffers from severely reduced predictive power for T_2 relaxation studies, where inhomogeneities and magnetic inclusions are a much stronger contributor to relaxation than dipolar couplings between protons. In order to analyze the effect of a heterogeneous magnetic environment on the coherence of the oscillation of the transverse magnetization of an ensemble of protons, it is instructive to return to the Bloch model. Immediately after a perturbing RF field (B_1) is applied to rotate the magnetization of an ensemble of dipoles into the transverse plane, the dipoles will precess at a rate that is proportional to the local field experienced by each proton. For the j^{th} proton in a solution:

$$\omega_j(t) = \omega_0 + \delta\omega_j(t)$$

Where $\omega_0 = \gamma B_0$ is the proton Larmor frequency at the bias field B_0 and $\delta\omega_j = \gamma\ \delta B_z(\boldsymbol{r}_j, t)$ is the change in Larmor precession frequency due to local inhomogeneities in the longitudinal field at the coordinates of the j^{th} proton. The complex signal generated by this ensemble is then:

$$S(t) = S_0\Sigma_j \mathrm{e}^{\mathrm{i}\int_0^t \omega_j(t')dt'} = S_0 e^{i\omega_0 t}\Sigma_j e^{i\int_0^t \delta\omega_j(t')dt'} = S_0 A(t) e^{i\omega_0 t}$$

In a reference frame rotating at the Larmor frequency, dipoles precess at $\delta\omega_j$. This small variation in precession frequency will, over time, reduce the summed signal of the precessing dipoles. The amplitude of the measured voltage in a receiver coil from the oscillating transverse magnetization of the ensemble of spins can then be calculated as:

$$Re\{A(t)\} = \Sigma_j \cos\left(\delta\phi_j(t)\right)$$

Where

$$\delta\phi_j(t) = \int_0^t \delta\omega_j(t')dt' = \gamma\int_0^t \delta B\big(\boldsymbol{r_j}(t'), t'\big)dt'$$

In the following sections, we will discuss a few examples of field perturbations and the mechanism through which they decohere precessing protons.

The signal that an ensemble of water molecules will produce immediately after being perturbed from equilibrium by a $\frac{\pi}{2}$ pulse is referred to as the free induction decay (FID). The Fourier transform of this FID will recover the spectral density $P(\omega)$ which will, in general, be a Lorentzian centered on ω_0 with a linewidth dictated by the heterogeneity of the magnetic environment experienced by protons in the ensemble. The finite width of the distribution of Larmor frequencies will cause the amplitude of the oscillating transverse magnetization to exponentially decay to zero with a time constant T_2^*.

In the limiting condition where the protons are static and the perturbing field δB_j is not time dependent, the dephased signal can be perfectly recovered into an “echo” by applying a resonant RF pulse in the transverse plane that rotates the magnetic dipoles by π radians. For a simple model of why such a pulse would be effective, we return to our rotating reference frame. If a $\frac{\pi}{2}$ pulse is applied to excite an ensemble of dipoles into the transverse plane, then after waiting time τ_{cp}, the phase accumulation of the j^{th} dipole in the rotating reference frame will be:

$$\delta\phi_j(\tau_{cp}) = \gamma \cdot \delta\mathrm{B_j} \cdot \tau_{cp}$$

A resonant π pulse rotates all dipoles around the x axis, turns positive phase accumulation into negative phase accumulation, so after the pi pulse has been applied:

$$\delta\phi_j = -\gamma \cdot \delta \mathrm{B}_\mathrm{j} \cdot \tau_{cp}$$

As the magnetic field and position of all protons is constant, after another waiting time τ_{cp}, the net phase accumulation of all dipoles will be zero in the rotating frame, resulting in a signal maximum in the lab frame. This simple case fails to account for the realities of biological tissue, where the diffusion of water causes a substantial time dependence for the local field experienced by a given proton. Accounting for this motion, the signal of an echo of an ensemble of spins is:

$$A(2\tau_{cp}) = \Sigma_j \cos\left(\delta\phi_j(2\tau_{cp})\right)$$

$$\delta\phi_j(2\tau_{cp}) = -\gamma \int_0^{\tau_{cp}} \delta B(\boldsymbol{r_j}(t'), t')dt' + \gamma \int_{\tau_{cp}}^{2\tau_{cp}} \delta B(\boldsymbol{r_j}(t'), t')dt'$$

Though the spin echo can mitigate the effect of static magnetic perturbations, it is unable to fully negate the effect of dynamic magnetic perturbations such as those experienced by protons diffusing past magnetic inclusions in tissue. As a result, the signal of echoes from repeated refocusing π pulses will exponentially decay over time with a time constant T_2. It is worth noting that in biological samples this time constant will differ significantly from the intrinsic T_2 predicted by BPP theory and, as will be discussed in the next section, can also have a strong dependence on experimental parameters. While this model for relaxation is quite simple, it has great predictive power for relaxation in a variety of biologically relevant magnetic environments.

1.7.1 Diffusion and relaxation near strong magnetic sources

Owing to their strong surface field gradients, biocompatibility, and ease of synthesis, magnetic nanoparticles are a versatile contrast agent for MRI. These strong magnetic sources cause a local perturbation to the magnetic field in tissue. As the vast majority of nanoparticles used in MRI are approximately spherical, their contribution to the local longitudinal magnetic field can be calculated using the point dipole equation:

$$B_z = \frac{\mu_0}{4\pi} \cdot \left(\frac{3(\boldsymbol{r} \cdot \hat{\boldsymbol{z}})(\boldsymbol{m} \cdot \boldsymbol{r})}{r^5} - \frac{\boldsymbol{m} \cdot \hat{\boldsymbol{z}}}{r^3} \right)$$

Here $\boldsymbol{m}$ is the magnetic moment vector of the nanoparticle and $\boldsymbol{r}$ is the displacement vector from the center of the nanoparticle.

If precessing water-bound protons were to remain static in a solution with magnetic nanoparticles, the magnetic field perturbation from the nanoparticles would induce strong T_2^* relaxation. The rate of relaxation in this situation can be calculated as: [19]

$$\frac{1}{T_2^*} = \frac{\pi\sqrt{15}v\Delta\omega_r}{9}$$

Here ν is the volume fraction of nanoparticles in solution and $\Delta\omega_r$ is the rms shift in the angular Larmor frequency at the nanoparticle surface, which is a constant for a given material ($\Delta\omega_r \approx 3 \cdot 10^7 rad/s$ for the commonly used magnetite nanoparticles). This prediction for T_2^* relaxation is valid in the Static Dephasing Regime (SDR) where the motion of water is sufficiently slow. That is, the characteristic time for diffusion of water past the source $\tau_D = \frac{D}{R^2}$ is much greater than $\frac{1}{\Delta\omega_r}$. Here D is the diffusion constant for water and R is the radius of the magnetic source [20].

In the opposite extreme, the motion of water molecules is rapid compared to the size of the magnetic source or the strength of the magnetic source is small ($\Delta\omega_r\tau_D \ll 1$). This “motional-averaging regime” is well characterized by classical outer sphere theory provided that $\tau_{cp} \gg \tau_D$. Here the refocusing pulses are largely ineffective and the relaxation rate is given by [21]:

$$\frac{1}{T_2^*} \approx \frac{1}{T_2} \approx \frac{4}{9}\nu\tau_D(\Delta\omega_r)^2$$

The phase dispersion of water near magnetic sources can also be controlled by limiting the time between refocusing pulses. If $\tau_{cp} \ll \tau_D$, the water molecules only move a short distance between refocusing pulses, and the effect of the magnetic inhomogeneity is reduced. In this echo-limited regime, the T_2 time can be approximated as

$$\frac{1}{T_2} \approx 2.25\nu(\Delta\omega)^2\left(\frac{\tau_{cp}^2}{\tau_D}\right)$$

While these analytical approximates are instructive for the relaxation of solutions of spherical, monodisperse, and weakly-magnetized particles, computational techniques are required to predict transverse relaxation in more biologically relevant environments [22, 23]. The analytical models are nonetheless instructive for highlighting the sensitivity of MRI contrast to microscale features [24]. This insight has profound and wide-ranging applicability from the development of contrast agents that dynamically change their spatial frequency (and thus their level of induced contrast) in response to a molecular signal [25] to improving the diagnostic efficacy of MRI for conditions that change the distribution of magnetic material in tissue [26].

1.8 Diffusion Weighted MRI

In addition to RF pulse sequences that weight MRI signal intensity by T_1 or T_2 relaxation inside of a given voxel, there are a wide library of sequences that weight MRI images by the motion of water inside of tissue. These sequences have broad applications including diagnosis of acute ischemia [3], mapping axonal tracts in the brain [27], and locating the expression of reporter genes that alter cellular membrane permeability [28]. While different applications of DWI have specifically tailored pulse sequences, they all rely on the encoding of space into the phase of the proton magnetic dipoles in a voxel using strong magnetic field gradients. To see how this is possible, we can return to our model for transverse relaxation.

We choose to apply a magnetic field gradient to an ensemble of nuclear spins in the transverse plane such that:

$$B_z(x) = B_0 + \delta B_z(x) = B_0 + G * x$$

Here, B_z is the total longitudinal field as a function of the x coordinate, B_0 is the local bias field, and $\delta B_z(x)$ is a linear applied magnetic field gradient with slope G. If we leave the gradient applied for a short time t_G, then the phase accumulated for nuclear spins in the sample will be:

$$\delta\phi_j(x_j) = \int_0^{t_G} \delta\omega(t')dt' = \gamma C * x_j(0) * t_G$$

Here, $x_j(0)$ is the x coordinate of the j^{th} nuclear spin at the time the gradient is applied. We turn the gradient off after t_G and after a waiting time Δ apply the negative of the initial field gradient such that:

$$B_z(x) = B_0 + \delta B_z(x) = B_0 - G * x$$

Leaving this new second gradient on for time t_G, the total phase accumulated by the j^{th} proton will then be:

$$\delta\phi_j(x) = \int_0^{2t_G+\Delta} \delta\omega(t')dt' = \gamma C * t_G * \big(x_j(0) - x_j(\Delta)\big) = \gamma G t_G \delta x_j$$

where δx_j is the change in the x coordinate of the j^{th} proton. Thus, the motion of water in the sample is encoded into phase accumulation in the rotating reference frame. In the case of free diffusion with diffusion constant D:

$$\langle|\delta x_j(\Delta)|\rangle = \sqrt{2D\Delta}$$

Thus, a more diffusive environment will increase dephasing and reduce signal intensity. Quantitatively,

$$S = S_0 e^{-bD}$$

Here $b = \gamma^2 G^2 t_G^2 (\Delta - \frac{t_G}{3})$ is the so-called “b-value” coined by Stejskal and Tanner [29]. Improvements to the proposed sequence can eliminate the sensitivity of the signal to T_2^* [29] and T_2 [30] relaxation, which can be critical for experiments requiring long Δ.

Bibliography

1. Glover, G.H. Overview of functional magnetic resonance imaging. *Neurosurg Clin N Am* **22**, 133-vii (2011).
2. Hernando, D., Levin, Y.S., Sirlin, C.B. & Reeder, S.B. Quantification of liver iron with MRI: state of the art and remaining challenges. *J Magn Reson Imaging* **40**, 1003-1021 (2014).
3. Le Bihan, D. & Johansen-Berg, H. Diffusion MRI at 25: exploring brain tissue structure and function. *Neuroimage* **61**, 324-341 (2012).
4. Alexander, A.L., Lee, J.E., Lazar, M. & Field, A.S. Diffusion tensor imaging of the brain. *Neurotherapeutics* **4**, 316-329 (2007).
5. Mukherjee, A., Davis, H.C., Ramesh, P., Lu, G.J. & Shapiro, M.G. Biomolecular MRI reporters: Evolution of new mechanisms. *Progress in Nuclear Magnetic Resonance Spectroscopy* **102-103**, 32-42 (2017).
6. Piraner, D.I. et al. Going Deeper: Biomolecular Tools for Acoustic and Magnetic Imaging and Control of Cellular Function. *Biochemistry* **56**, 5202-5209 (2017).
7. Feynman, R.P., Vernon, F.L. & Hellwarth, R.W. Geometrical Representation of the Schrödinger Equation for Solving Maser Problems. *Journal of Applied Physics* **28**, 49-52 (1957).
8. Bloch, F. Nuclear induction. *Physical review* **70**, 460 (1946).
9. Griffiths, D.J. Introduction to Electrodynamics. (Pearson Education, 2014).
10. Torrey, H.C. Bloch Equations with Diffusion Terms. *Physical Review* **104**, 563-565 (1956).
11. Ma, D. et al. Magnetic resonance fingerprinting. *Nature* **495**, 187-192 (2013).
12. Bloembergen, N. Proton Relaxation Times in Paramagnetic Solutions. *The Journal of Chemical Physics* **27**, 572-573 (1957).
13. Krynicki, K. Proton spin-lattice relaxation in pure water between 0°C and 100°C. *Physica* **32**, 167-178 (1966).
14. Lauffer, R.B. Paramagnetic metal complexes as water proton relaxation agents for NMR imaging: theory and design. *Chemical Reviews* **87**, 901-927 (1987).
15. Belorizky, E. & Fries, P.H. Simple analytical approximation of the longitudinal electronic relaxation rate of Gd(iii) complexes in solutions. *Physical Chemistry Chemical Physics* **6**, 2341-2351 (2004).
16. Caravan, P., Farrar, C.T., Frullano, L. & Uppal, R. Influence of molecular parameters and increasing magnetic field strength on relaxivity of gadolinium- and manganese-based T1 contrast agents. *Contrast Media Mol Imaging* **4**, 89-100 (2009).
17. Lelyveld, V.S., Brustad, E., Arnold, F.H. & Jasanoff, A. Metal-Substituted Protein MRI Contrast Agents Engineered for Enhanced Relaxivity and Ligand Sensitivity. *Journal of the American Chemical Society* **133**, 649-651 (2011).
18. Shapiro, M.G. et al. Directed evolution of a magnetic resonance imaging contrast agent for noninvasive imaging of dopamine. *Nat Biotechnol* **28**, 264-270 (2010).
19. Vuong, Q.L., Berret, J.-F., Fresnais, J., Gossuin, Y. & Sandre, O. A Universal Scaling Law to Predict the Efficiency of Magnetic Nanoparticles as MRI T2-Contrast Agents. *Advanced Healthcare Materials* **1**, 502-512 (2012).
20. Gillis, P., Moiny, F. & Brooks, R.A. On T2-shortening by strongly magnetized spheres: A partial refocusing model. *Magnetic Resonance in Medicine* **47**, 257-263 (2002).
21. Brooks, R.A., Moiny, F. & Gillis, P. On T2-shortening by weakly magnetized particles: The chemical exchange model†. *Magnetic Resonance in Medicine* **45**, 1014-1020 (2001).

22. Novikov, D.S. & Kiselev, V.G. Transverse NMR relaxation in magnetically heterogeneous media. *Journal of Magnetic Resonance* **195**, 33-39 (2008).
23. Matsumoto, Y. & Jasanoff, A. T2 relaxation induced by clusters of superparamagnetic nanoparticles: Monte Carlo simulations. *Magnetic resonance imaging* **26**, 994-998 (2008).
24. Vuong, Q.L., Gillis, P. & Gossuin, Y. Monte Carlo simulation and theory of proton NMR transverse relaxation induced by aggregation of magnetic particles used as MRI contrast agents. *Journal of Magnetic Resonance* **212**, 139-148 (2011).
25. Sosnovik, D.E. & Weissleder, R. Emerging concepts in molecular MRI. *Current Opinion in Biotechnology* **18**, 4-10 (2007).
26. Ghugre, N.R. & Wood, J.C. Relaxivity-iron calibration in hepatic iron overload: Probing underlying biophysical mechanisms using a Monte Carlo model. *Magnetic Resonance in Medicine* **65**, 837-847 (2011).
27. O'Donnell, L.J. & Westin, C.-F. An introduction to diffusion tensor image analysis. *Neurosurg Clin N Am* **22**, 185-viii (2011).
28. Mukherjee, A., Wu, D., Davis, H.C. & Shapiro, M.G. Non-invasive imaging using reporter genes altering cellular water permeability. *Nature Communications* **7**, 13891 (2016).
29. Stejskal, E.O. & Tanner, J.E. Spin Diffusion Measurements: Spin Echoes in the Presence of a Time-Dependent Field Gradient. *The Journal of Chemical Physics* **42**, 288-292 (1965).
30. Merboldt, K.-D., Hänicke, W. & Frahm, J. Diffusion imaging using stimulated echoes. *Magnetic Resonance in Medicine* **19**, 233-239 (1991).

Chapter 2

SOME RANDOM WALKS IN COMPUTATIONAL MRI

2.1 Introduction

The clear advantages of MRI for biological imaging include its penetration depth, noninvasiveness, and strong endogenous anatomical contrast. However, the murky and multifactorial origins of MRI contrast limit the applicability of even the most complex analytical models. In order to accelerate the development of molecular reporters for MRI that operate on cellular length scales, we developed an *in silico* platform to simulate the effect of genetic perturbations to target cells on the magnetic relaxation of surrounding water molecules.

Our first application of this platform helped us understand the mechanism of contrast for the diffusion MRI reporter gene aquaporin, which enhances water mobility by increasing the water permeability of the plasma membrane. In addition to providing key insights to the physical mechanism of contrast for this reporter gene, the simulations in this study helped us optimize the pulse-sequence parameters to maximize contrast over background tissue. The first section of this chapter is an adapted excerpt from our publication on the study[1], focusing on the physical model and simulations.

In the second section of this chapter, we will discuss a recent application of computational MRI to UPMAG, a new ultraparamagnetic reporter gene for MRI of bacterial cellular agents [2]. UPMAG relies on highly disordered complexes of iron-binding proteins and paramagnetic iron oxide to decohere intracellular water-bound protons, which should not produce significant contrast according to classical outer-sphere relaxation theory. We were nonetheless able to account for the physical mechanism behind the observed transverse relaxation enhancement using a Monte Carlo simulation that simultaneously modeled the restricted diffusion and magnetic relaxation of water molecules in and around cells expressing UPMAG.

2.2 Non-invasive imaging using aquaporin

Adapted from: A . Mukherjee, D. Wu, **H.C. Davis**, M.G. Shapiro (2016). "Non-invasive imaging using reporter genes altering cellular water permeability." *Nature Communications* **7**(1): 13891.

The ability to image gene expression within the context of living mammalian organisms is critical for basic biological studies and the development of cellular and genetic therapeutics. However, most genetically encoded reporters, based on fluorescent and luminescent proteins[3-5] have limited utility in this context due to the poor penetration of light into deep tissues[3, 4, 6, 7]. In contrast to optical techniques, magnetic resonance imaging (MRI) enables the acquisition of *in vivo* images with excellent depth penetration and high spatial and temporal resolution. Consequently, there is intense interest in the development of genetically encoded reporters for MRI[8-30]. Previous efforts to develop such reporters have focused primarily on two classes of proteins. In one class, metalloproteins and metal ion transporters are overexpressed to enrich the paramagnetic content of cells, thereby enhancing nuclear relaxation rates and producing contrast in T_1 or T_2-weighted MRI[11, 14-21, 29-31]. In the second strategy, proteins with large numbers of basic amino acids are used to generate contrast through chemical exchange saturation transfer (CEST) between protein-bound and aqueous protons[8, 10, 23, 24, 27, 32]. Each of these pioneering approaches has significant limitations. Metal-based reporters can be hindered by metal ion bioavailability and toxicity[33-37], while CEST reporters tend to require high expression levels to achieve observable contrast[8, 23, 24, 32]. Hence, a major need exists for new MRI reporter genes that do not require metals and can be detected at low levels of expression.

Here, we introduce an entirely new class of non-metallic MRI reporter genes that work by modulating water diffusivity across cell membranes. Diffusion weighted imaging (DWI) is a well-established MRI modality used in a wide range of applications from basic biophysical studies to the diagnosis of diseases such as stroke[38-42]. Diffusion weighting is commonly achieved by applying a pair of pulsed magnetic field gradients, which dephase proton spins proportionally to their diffusion distance in the time interval between gradient applications[43-45]. Accordingly, tissue regions characterized by rapid water diffusion have reduced signal intensity compared to regions with restricted water mobility. In biological tissues, the effective diffusion coefficient of water depends on several parameters including the local diffusivity in intracellular and extracellular compartments, the relative volume fraction occupied by cells, and the diffusion of water across the plasma membrane[46-51]. Noting the strong influence of the last factor[46, 52], we hypothesized that facilitating the transmembrane diffusion of water by overexpressing water-permeable channels would result in enhanced contrast in DWI. Towards this end, aquaporins are a highly conserved family of tetrameric integral membrane proteins that mediate the selective exchange of water molecules across the plasma membrane in a wide range of cell types including erythrocytes, astrocytes, and kidney cells[53-55]. Previously, endogenous aquaporin expression has been correlated with water diffusivity and DWI signals in several disease states[54, 56, 57]. However, to the best of our knowledge, aquaporins have not hitherto been described as MRI reporter genes. In this work, we introduce human aquaporin 1 (AQP1) as a new genetically encoded reporter for diffusion weighted MRI. This reporter gene requires no metals, is nontoxic in a wide range of cells, produces contrast orthogonal to paramagnetic and CEST reporters and is detectable when expressed at low levels and in small subsets of cells. We characterize the imaging performance and mechanisms of AQP1 through live cell experiments and Monte Carlo models and demonstrate its utility by imaging tumor gene expression *in vivo*.

2.2.1 Physical Model and simulation of DWI contrast

A key parameter in diffusion weighted pulse sequences is the effective diffusion time, Δ_{eff}, corresponding to the time interval between dephasing and rephasing gradient pulses[38, 39, 45, 46, 48, 58]. Long Δ_{eff} times are important for probing the effects of water exchange between intracellular and extracellular pools because longer times allow a larger proportion of cytoplasmic molecules to interact with the cell membrane and experience the effects of restriction and exchange[38, 39, 48, 51]. In order to simulate the effects of the effects of this restricted diffusion on MRI signal, we developed a model for restricted water diffusion and exchange in cells, building on the previously described Karger and Szafer[48, 51, 59] models of tissue water diffusion. We modeled our experimental cell pellets as a face-centered cubic lattice packed with 108 spherical cells with water molecules distributed randomly throughout the lattice at $t = 0$. Cell radii were sampled from a normal distribution with a mean of 6.8 μm and a standard deviation of 1.2 μm. We set the simulation time step $\tau = 50\ \mu s$ and at each time step, water molecules were propagated in a 3D random walk with step size given by

$N\sqrt{\pi/2}\,\sqrt{2D\tau}$ in each direction. Here, N is sampled from a random normal distribution and D is the free diffusion coefficient of water at 12.9°C (the bore temperature of our MRI scanner) in the intracellular compartment (554.7 $\mu m^2/s$) or in the extracellular space (1664.2 $\mu m^2/s$)[60]. If a water molecule encounters a membrane, the propagation step is recalculated and the molecule either transmitted or reflected off the membrane with a probability given by $1 - 4P\sqrt{\tau/6D}$, wherein P is the membrane permeability and D is the free diffusion coefficient of water in the intracellular compartment. Diffusion paths were simulated in Python and the apparent diffusion coefficient (ADC) was calculated using Matlab as described in the Szafer model[48]: $ADC(\Delta) = -\lim_{q\to 0^+} \frac{ln<e^{-q\frac{\sum x^2}{2}}>}{q\Delta}$ where $\sum x^2$ represents the sum square displacement of a water molecule from its starting position and q is given by $(\gamma\delta g)^2$ where γ is the gyromagnetic ratio, g is the gradient strength and δ is the duration of the pulsed diffusion gradient. We note that b-value is calculated as: $b = q.(\Delta - \delta/3)$. In the first set of simulations (ADC *vs.* permeability), we varied the cell permeability from .034 to 0.39 μm/s and calculated ADC(Δ) for each value of cell permeability. In the second set of simulations (ADC *vs.* fraction of AQP1-expressing cells) the permeability of AQP1-expressing cells and control cells were fixed at 0.14 μm/s and 0.039 μm/s respectively, in accordance with previously published values[55]. We incrementally varied the fraction of cells expressing AQP1 and for each composition, simulated 3 x 10^4 (nonunique) random arrangements of AQP1 expressing and control cells to exclude geometry or arrangement dependent bias in the results. ADC(Δ) was estimated corresponding to varying fractions of AQP1 expressing cells in the population.

Our Monte Carlo simulations of a packed cellular lattice suggested that the effects of an aquaporin-mediated increase in water diffusion would be most pronounced at $\Delta_{eff} > 100$ ms (**Figure 2.1**). To access these longer diffusion times, we used a stimulated echo DWI sequence, in which net magnetization is stored along the longitudinal axis in the interval between the diffusion gradients, and is thereby limited by T_1 relaxation, rather than the typically shorter T_2 relaxation limit of the more widely used spin echo DWI[46, 58, 61]. Pellets of AQP1-expressing cells appeared much darker in diffusion-weighted images than GFP controls (**Figure 2.2a**), corresponding to dramatic increases in their apparent diffusion coefficients. We found that the relative increase in ADC is more pronounced at $\Delta_{eff} = 398$ ms compared to $\Delta_{eff} = 18$ ms (**Figure 2.2b**), consistent with AQP1 expression facilitating the exchange of water across the cell membrane.

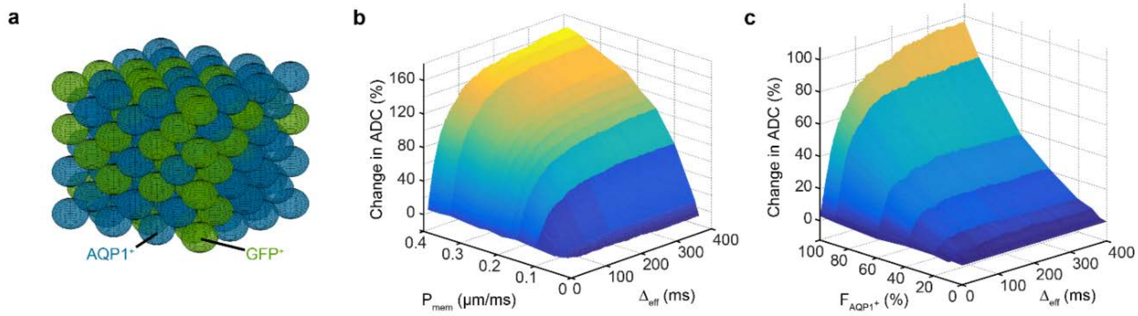

Figure 2.1 Monte Carlo simulations of water diffusion in AQP1$^+$ and GFP$^+$ (control) cells as a function of cell membrane permeability (P_{mem}), effective diffusion time (Δ_{eff}), and percentage of AQP1-labeled cells (F_{AQP1+}). We modeled cellular tissue as a face-centered cubic lattice packed with 108 spherical cells and with water molecules distributed randomly throughout the lattice at $t = 0$. **a** Mixed populations of AQP1$^+$ and GFP$^+$ cells were modeled by randomly distributing AQP1$^+$ and GFP$^+$ cells in the lattice to simulate 3 x 10^4 (nonunique) random arrangements of heterogeneous cell populations corresponding to varying fractions of AQP1$^+$ cells. **b** ADC increases with increasing cell permeability, with the percent change in the ADC (measured relative to control cells with a basal permeability of 0.035 μm/s[55]) being most pronounced at longer diffusion times, consistent with the role of AQP1 in enhancing water diffusion across the cell membrane. **c** ADC increases in a nonlinear fashion with increase in the fraction of AQP1-labeled cells in a mixed population comprising AQP1$^+$ and GFP$^+$ cells. AQP1$^+$ cells are assigned a permeability coefficient of 0.14 μm/s while GFP-

expressing control cells are assigned a basal permeability 0.035 µm/s in accordance with literature values[55].

2.2.2 Dynamic range of AQP1

Next, we sought to establish whether AQP1 can be used to report on varying degrees of gene expression, particularly at low levels of expression. Our Monte Carlo simulations suggested that ADC values are sensitive to a broad range of cell membrane permeabilities (**Figure 2.1b**), providing AQP1 with significant dynamic range. To realize this experimentally, we expressed AQP1 in a dose-dependent fashion by supplementing CHO cells with varying concentrations of doxycycline and measured corresponding values of ADC (**Figure 2.2, a-b**). AQP1 expression was also quantified via western blotting (**Figure 2.2c**). Significant changes in ADC and DWI contrast (53% and 29% respectively) were observed with very low levels of doxycycline induction (0.01 µg/mL), which corresponded to membrane AQP1 expression below the chemiluminescence detection limit of our western blot. At the lowest blotting-detectable level of AQP1 expression, corresponding to an AQP1 concentration of 1.06 ± 0.19 µM (induced with 0.1 µg/mL doxycycline, N = 2), cells showed a 164 ± 5% increase in ADC relative to controls. Since substantial DWI contrast is also observed at 10-fold lower induction levels, we expect that the actual detection limit for AQP1 expression is significantly below 1 µM. This large dynamic range will facilitate the use of AQP1 as a reporter gene in a variety of biomedical applications.

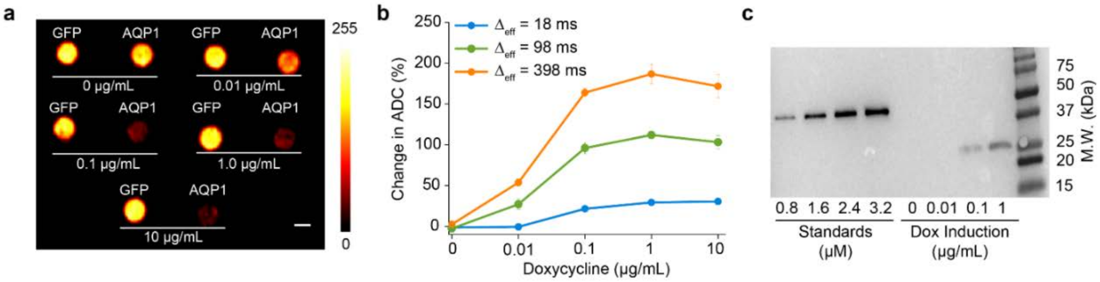

Figure 2.2 AQP1 reports gene expression over a large dynamic range. a Diffusion weighted images (acquired at Δ_{eff} = 398 ms, b = 2089 s/mm^2) of CHO cells expressing AQP1 or GFP (control) and treated with varying doses of doxycycline to induce transgene expression. Scale bar indicates 3 mm. **b** Percent change in ADC of water in AQP1-expressing CHO cells (relative to control cells expressing GFP) as a function of doxycycline concentration, measured at different diffusion times. Error bars represent SEM for 4 biological replicates. **c** Representative western blot used to quantify AQP1 expression in CHO cells using FLAG-tagged bacterial alkaline phosphatase at the indicated concentrations as a calibration standard. AQP1 levels were estimated using membrane fractions isolated from AQP1 expressing CHO cells respectively induced using 0, 0.01, 0.1, and 1 µg/mL doxycycline for 48 hours. AQP1 levels corresponding to 0.01 µg/mL doxycycline are below the blotting-detectable limit.

2.2.3 Contrast from AQP1 within a mixed population

The ability to specifically detect small numbers of genetically labeled cells in a population of unlabeled cells would enable the use of genetically encoded reporters in applications such as *in vivo* tracking of cell based therapeutics[18, 62, 63]. Having shown that AQP1 can appreciably increase water diffusion even at low levels of expression (**Figure 2.2**), we tested whether apparent water diffusion could be significantly increased if AQP1 expression was restricted to a small subset of cells in a mixed population. In general, the relationship between expressing fraction and ADC is expected to be nonlinear, since in small-fraction scenarios, cells expressing AQP1 would be surrounded mostly by cells without enhanced water permeability, and the impact of AQP1 expression would therefore be diminished (**Figure 2.3a**). However, our Monte Carlo simulations predicted that even in this scenario, expressing fractions as small as 10% could be sufficient to increase the overall ADC in heterogeneous cell populations, particularly at long Δ_{eff} times (**Figures 2.3b, 2.1c**). To verify this experimentally, we measured ADC in mixed populations comprising AQP1 expressing CHO cells and GFP expressing control cells in varying proportions. Strikingly, diffusion measurements revealed a significant increase in ADC in cell populations comprising 10% AQP1 expressing cells (21.44 ± 5.21% relative to GFP expressing cells, measured at Δ_{eff} = 398 ms, $P = 0.04$, $n = 4$, **Figure 2.3c-d**). Furthermore, under optimal imaging conditions we were able to observe 12.87% and 19.58% decreases in diffusion weighted image intensity for 5% and 10% AQP1 cell populations, respectively, relative to homogeneous GFP controls (**Figure 2.3c, inset**). This data suggests that, contrary to initial intuition, diffusional reporter genes such as AQP1 are suitable for imaging gene expression in heterogeneous or infiltrating cell populations.

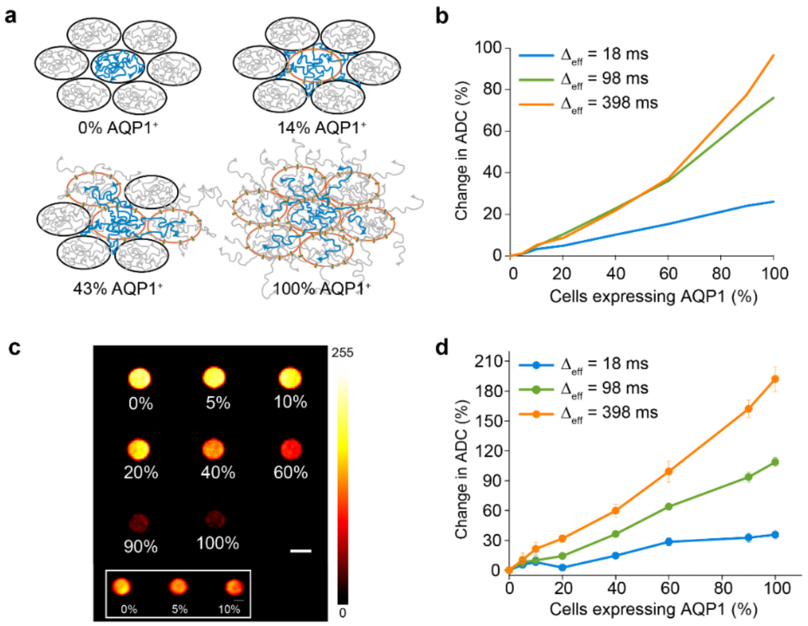

Figure 2.3 AQP1 expression is observable in mixed cell populations. a Illustration of the effect of an increasing fraction of AQP1-labeled cells in a tissue on the overall diffusivity of water. **b** Monte Carlo simulations of percent increase in ADC as a function of the fraction of cells expressing AQP1 in a mixed population. **c** Diffusion weighted MRI (acquired at Δ_{eff} = 198 ms, b = 2334 s/mm^2) of cells comprising AQP1-labeled cells mixed with GFP-labeled control cells in varying proportions. (Inset) Mixed populations consisting of 0, 5, and 10% AQP1 expressing cells independently imaged using optimal parameters (Δ_{eff} = 398 ms, b = 8000 s/mm^2) to maximize contrast for the low AQP1 fraction scenario. In order to reduce image noise and improve visual clarity, the image was smoothed using a low pass Gaussian filter, implemented in ImageJ. Scale bar represents 3 mm. **d** Experimental percent change in ADC in mixed AQP1/GFP cell pellets as a function of the fraction of AQP1 expressing cells. Error bars represent SEM for 4 biological replicates.

2.3 Transverse relaxation from ultraparamagnetic cells

Adapted from: P. Ramesh, S.-J. Hwang, **H. C. Davis**, et al. (2018). “Ultraparamagnetic cells formed through intracellular oxidation and chelation of paramagnetic iron.” *Angew. Chem. Int. Ed.* , ***57***, 12385.

Inspired by magnetotactic bacteria, chemical and synthetic biologists have attempted to impart ferromagnetism or superparamagnetism onto non-magnetic microbial and eukaryotic cell types to enable their localization and isolation from complex samples using magnetic fields and visualization with magnetic resonance imaging (MRI)[1–4]. Such capabilities would facilitate, for example, the study of commensal and pathogenic microbes inside mammalian hosts and the development of magnetically engineered microbial diagnostic and therapeutic agents[5,6]. However, because of the stringent pH, iron concentrations and redox potentials required for the synthesis of magnetosomal magnetite and other forms of superparamagnetic or ferromagnetic iron oxides, attempts to engineer the formation of these minerals in natively non-magnetic species such as *E. coli* have had limited success[7–11].

Here, we introduce an alternative paradigm for producing magnetic cells that is focused on maximizing cellular paramagnetism rather than forming superparamagnetic or ferromagnetic deposits. This approach arises from the recognition that many applications of magnetic cells, including MRI and cellular separation, involve multi-Tesla magnetic fields, in which sufficiently paramagnetic cells would be expected to act as microscale magnets, capable of producing MRI contrast and experiencing magnetic gradient forces for localization and separation (**Fig. 2.4a**)[12,13]. With such "ultraparamagnetism" as the stated goal, ferritin – the main iron storage protein in most cells and the focal point of previous efforts in magnetic cell engineering – represents a relatively poor iron host because most of the electron spins in its ferrihydrite core are cancelled by antiferromagnetic partners, such that its net paramagnetic moment equates to only ~5% of the available spin at 37 ºC [14,15].

We hypothesized that better use of intracellular iron could be made by cells expressing a protein construct specifically designed to nucleate and chelate iron in a paramagnetic configuration. In this work, we engineer such a construct, characterize it physically and biochemically, and show that *E. coli* expressing it have 8-fold stronger paramagnetism than ferritin-overexpressing controls. This allows these cells to be localized via magnetic field gradients, visualized with MRI, and isolated from complex biological samples.

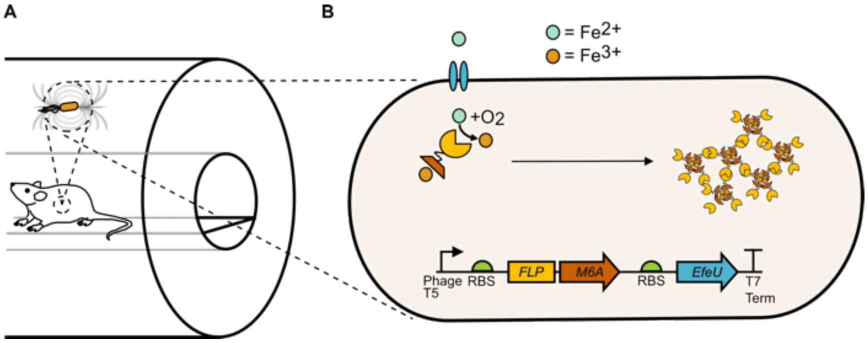

Figure 2.4 Ultraparamagnetic gene circuit. a Paramagnetic cells produce magnetic fields and experience force when placed inside a strong magnetic field, such as in an MRI scanner. **b** UPMAG gene circuit, comprising a ferroxidase (FLP) fused to a magnetite nucleating peptide (M6A), and a ferrous iron transporter (EfeU). The circuit is driven using an IPTG-inducible T5 phage promoter. The ferrous iron transporter increases the intracellular iron content available to FLPM6A. FLPM6A then forms macromolecular assemblies with oxidized iron.

2.3.1 Design of the genetic construct

To produce and store intracellular iron in a paramagnetic state, we created a fusion protein combining the decameric ferroxidase FLP from *Rhodospirillum Rubrum* with the iron-binding peptide M6A derived from the last 20 C-terminal residues of the Mms6 protein from *Magnetospirillum magneticum* (**Fig. 2.4 b**)[16,17]. Iron can be imported into *E.coli* as Fe^{2+}, but must be oxidized to avoid the production of toxic radicals via the Haber-Weiss reaction[18]. We specifically chose FLP for this purpose because it can effectively oxidize ferrous iron, but does not on its own mineralize the iron into potentially poorly magnetic iron oxides[16]. This stands in contrast to ferritin, which both oxidizes iron and stores it as an antiferromagnetic mineral. The second component, M6A, was previously shown to promote and stabilize the nucleation of magnetic iron species *in vitro*[17,19]. We hypothesized that, after

FLP oxidizes iron to Fe^{3+}, M6A would bind any available ferrous iron as well as oxidized ferric iron and promote the nucleation of small iron oxide minerals[20], stabilized by multiple M6A binding interactions (**Fig. 2.4 b**). We predicted that this iron would remain in a loosely ordered, strongly paramagnetic state. As control constructs, we generated *E. coli* overexpressing bacterioferritin (BFR) or fluorescent proteins (FP: mRuby2 or eGFP). BFR was chosen as our standard for comparison based on its previous use as a genetically encoded contrast agent for MRI [21]. All vectors also included the iron transporter EfeU from *E. coli* Nissle 1917 to facilitate the uptake of ferrous iron from the growth medium. These constructs were expressed in a model strain of *E. coli* (BL21 DE3) with no additional alterations to endogenous iron-handling genes. The complete genetic circuit consisting of FLPM6A and EfeU is hereafter referred to as UPMAG, for UltraParaMagnetic Genes.

2.3.2 Experimental Results

To assess whether the cellular paramagnetism conferred by UPMAG could be used for noninvasive cellular imaging in addition to magnetic actuation, we imaged cells expressing this construct with MRI. When imaged in agarose phantoms at 7 Tesla, UPMAG cells produced T_2 contrast relative to both background and controls at densities as low as 1×10^{10}, colony forming units (cfu) per ml, corresponding to a cellular volume fraction of 3.6 % (**Fig. 2.5a**)[25]. In contrast, cells expressing FP required at least 3-fold higher concentrations to be comparably visualized relative to background. Overexpression of BFR led to only a modest increase in T_2 contrast relative to FP, as expected based on the fact that *E.coli* cultured in iron-rich media also upregulate the expression of endogenous ferritins such as ftnA, ftnB, and BFR[26–28].

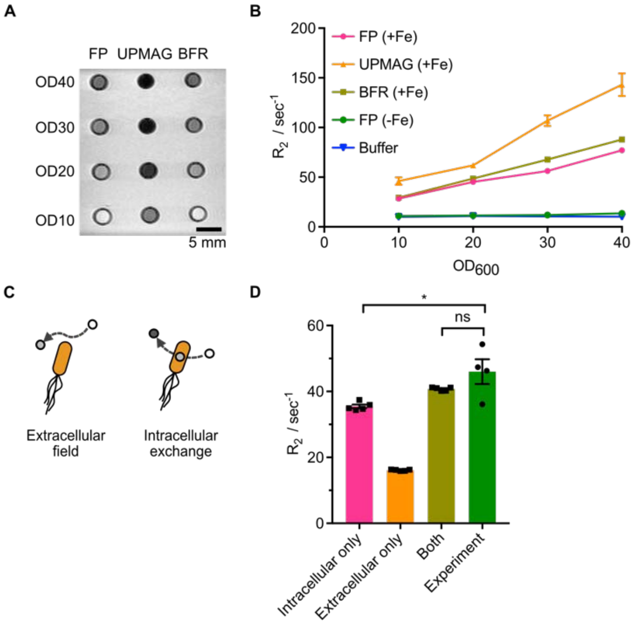

Figure 2.5 UPMAG cells produce enhanced MRI contrast. a A T_2 weighted image of *E.coli* in an agarose phantom, acquired at 7 Tesla using a spin echo sequence with $T_R = 2500$ ms and $T_E = 11$ ms. **b** R_2 vs. OD_{600} for *E.coli* expressing either UPMAG or controls in a Bruker 500 MHz NMR spectrometer with a spin echo sequence and $T_E = 0.5$ ms. **(c)** Schematic of two potential mechanisms of T_2 contrast, one in which water relaxes due to extracellular outer-sphere dipole relaxation, and a second in which water relaxes via diffusional exchange into the intracellular compartment. **d** Monte Carlo simulation results for cells at $OD_{600} = 10$, in comparison with experimental data.

Quantitative NMR measurements at 11.7 Tesla showed that solutions of *E. coli* expressing UPMAG had 70% faster relaxation rates compared to controls at cell optical density OD10 (**Fig. 2.5b**), with a cellular T_2 relaxivity of approximately $3.4\ \frac{\mathrm{sec}^{-1}}{\mathrm{OD}_{600}}$, or equivalently a per-iron relaxivity of $20.7\ \mathrm{mM}^{-1}\mathrm{sec}^{-1}$, as determined by linear fit. Monte Carlo simulations of water diffusion and spin precession in media containing ultraparamagnetic bacteria further revealed that most of the observed T_2 relaxation enhancement can be explained by diffusional water exchange between the bulk and the $\Delta\chi$-shifted cell interior (**Fig. 2.5, c-d, Fig. 2.6a**)

2.3.3 Monte Carlo Simulations

Nuclear spin relaxation was simulated for by randomly distributing spherical *E. coli* cells with $\chi_V = +4.68\ \mathrm{ppm}$ inside a $1000\ \mu\mathrm{m}^3$ cubic simulation volume using periodic boundary conditions. Cell radius was set to $0.65\ \mu\mathrm{m}$ to match previously reported equivalent cell volumes of *E. coli* [10]. The number of cells in the simulation volume was set to match the OD of our experimental data using the Agilent estimate of $\mathrm{N_{cells}} = \mathrm{OD}_{600} \cdot \mathrm{V}_{E.coli} \cdot 8 \times 10^{11}$, where V is the simulation volume in cubic meters. The magnetic moment of each *E. coli* cell was calculated as $\mathrm{m} = \chi_\mathrm{V} \cdot \mathrm{V} \cdot \mathrm{H}$ where χ is the bulk magnetic susceptibility, V is the volume of the cell, and H is the bias field in the NMR spectrometer (11.7 Tesla). The magnetic field B in the extracellular space was explicitly calculated for each water molecule based on the sum contribution from each *E. coli* cell. 4032 water molecules were randomly assigned initial 3D spatial coordinates ($\mathbf{r} = [x, y, z]$) in the simulation volume with phase $\phi(\mathrm{t}_0) = 0$ and allowed to diffuse according to previously established cellular diffusion models[8,9]. The phase in the rotating reference frame evolves according to $\delta\phi(\mathrm{t}) = -\gamma \cdot \mathbf{B}(\mathbf{r}) \cdot \delta\mathrm{t}$ for water in the extracellular space, where γ is the proton gyromagnetic ratio and **B** is the total magnetic field in the rotating reference frame as experienced by the water molecules. For water in the intracellular space, phase evolves according to $\delta\phi(\mathrm{t}) = \Delta\omega \cdot \delta\mathrm{t}$, where $\Delta\omega$ is the shift in the Larmor frequency due to the difference in intracellular bulk magnetic susceptibility relative to external media. Re-focusing pulses were simulated by setting $\phi(\mathrm{t}) = -\phi(\mathrm{t} - \delta\mathrm{t})$. Cell membranes were modeled as semi-permeable boundaries with a permeability of $2\ \frac{\mu\mathrm{m}}{\mathrm{ms}}$, in accordance with previously measured values for *E.coli* cells[11]. Intracellular and extracellular water diffusivity were set to 1 and $2\ \frac{\mu\mathrm{m}^2}{\mathrm{ms}}$ respectively, in accordance with previous studies of cellular diffusion and established values for water diffusivity at the temperature of our spectrometer bore $(20\ ^{\circ}\mathrm{C})$. Bulk spin magnetization in the sample was calculated as $\mathrm{M(t)} = \sum_{\mathrm{i}} \cos\,[\phi_{\mathrm{i}}(\mathrm{t})]$, where i is the index of simulated water molecules and the magnetic moment of a single molecule is normalized to 1. T_2 values were extracted from each simulated sample with a mono-exponential fit to the first 10 echoes. Background relaxation from buffer was accounted for by multiplying all simulated exponential decays with a mono exponential decay whose rate constant was equal to the experimentally measured relaxation rate of pure buffer.

We simulated three different diffusion models to determine the dominant relaxation mechanism for UPMAG expressing *E.coli*. In the combined model, both intracellular and extracellular contributions to relaxation were allowed as described above. In the “intracellular only” case, membrane permeability was as described above, but the $\delta\phi$ for extracellular water was set to zero. In this way, we were able to isolate the intracellular relaxation that arises solely from water molecules transiting through a compartment with different magnetic susceptibility. In the “extracellular only” case, water molecules were initialized only in the extracellular space, and the cell membranes were modeled as impermeable to water. In this way, we were able to isolate the effect of the outer-sphere dipolar relaxation due to the net magnetic moment of the *E.coli* cells. We found that intracellular relaxation was dominant and explained the preponderance of the relaxation. Our simulation that combined both relaxation effects accurately predicted the relaxation rate within experimental uncertainty over a wide concentration range. (**Fig 2.6**) All simulations were written in CUDA and performed on two NVIDIA K40 GPUs.

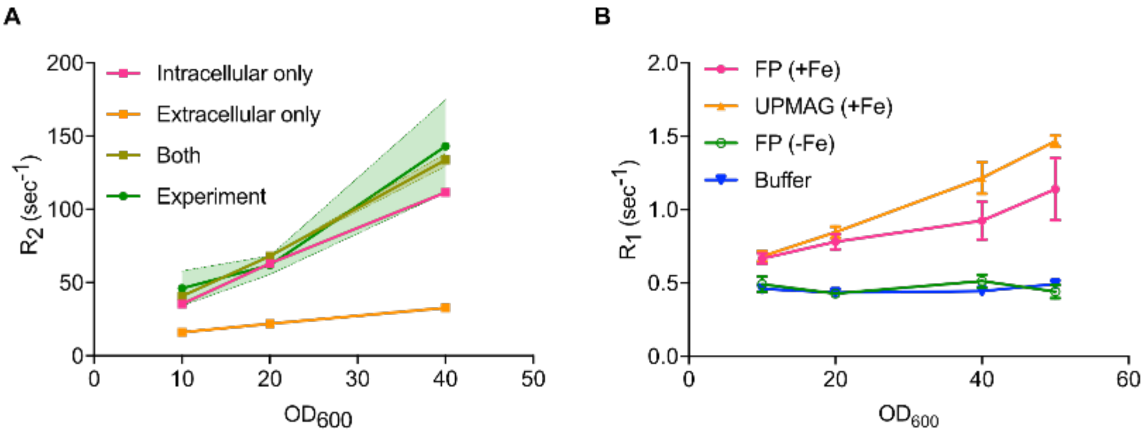

Figure 2.6 Simulated and experimental relaxation rates for multiple concentrations a Simulated transverse relaxation rates (R_2) for UPMAG expressing *E. coli* for different cell densities. Exchange of water between compartments with a difference of + 4.68 ppm in bulk susceptibility accounts for the bulk of the observed transverse relaxation rates. **b** Spin-lattice relaxation rates (R_1) for *E.coli* expressing either FP or UPMAG grown under various conditions.

Bibliography

1. Mukherjee, A., Wu, D., Davis, H.C. & Shapiro, M.G. Non-invasive imaging using reporter genes altering cellular water permeability. *Nature Communications* **7**, 13891 (2016).
2. Ramesh, P. et al. Ultraparamagnetic Cells Formed through Intracellular Oxidation and Chelation of Paramagnetic Iron. *Angewandte Chemie International Edition* **57**, 12385-12389 (2018).
3. Rao, J., Dragulescu-Andrasi, A. & Yao, H. Fluorescence imaging in vivo: recent advances. *Current opinion in biotechnology* **18**, 17-25 (2007).
4. Contag, C.H. & Bachmann, M.H. Advances in in vivo bioluminescence imaging of gene expression. *Annual review of biomedical engineering* **4**, 235-260 (2002).
5. Chudakov, D.M., Matz, M.V., Lukyanov, S. & Lukyanov, K.A. Fluorescent proteins and their applications in imaging living cells and tissues. *Physiological reviews* **90**, 1103-1163 (2010).
6. Weissleder, R. A clearer vision for in vivo imaging. *Nature biotechnology* **19**, 316-316 (2001).
7. Ntziachristos, V., Ripoll, J., Wang, L.V. & Weissleder, R. Looking and listening to light: the evolution of whole-body photonic imaging. *Nat Biotech* **23**, 313-320 (2005).
8. Bar-Shir, A. et al. Human protamine-1 as an MRI reporter gene based on chemical exchange. *ACS chemical biology* **9**, 134-138 (2013).
9. Louie, A.Y. et al. In vivo visualization of gene expression using magnetic resonance imaging. *Nat Biotech* **18**, 321-325 (2000).
10. Bar-Shir, A. et al. Transforming thymidine into a magnetic resonance imaging probe for monitoring gene expression. *Journal of the American Chemical Society* **135**, 1617-1624 (2013).
11. Zurkiya, O., Chan, A.W. & Hu, X. MagA is sufficient for producing magnetic nanoparticles in mammalian cells, making it an MRI reporter. *Magnetic resonance in medicine* **59**, 1225-1231 (2008).
12. Cohen, B., Dafni, H., Meir, G., Harmelin, A. & Neeman, M. Ferritin as an endogenous MRI reporter for noninvasive imaging of gene expression in C6 glioma tumors. *Neoplasia* **7**, 109-117 (2005).
13. Cohen, B. et al. MRI detection of transcriptional regulation of gene expression in transgenic mice. *Nature medicine* **13**, 498-503 (2007).
14. Patrick, P.S. et al. Dual-modality gene reporter for in vivo imaging. *Proceedings of the National Academy of Sciences of the United States of America* **111**, 415-420 (2014).
15. Patrick, P.S. et al. Development of Timd2 as a reporter gene for MRI. *Magnetic resonance in medicine* (2015).
16. Matsumoto, Y., Chen, R., Anikeeva, P. & Jasanoff, A. Engineering intracellular biomineralization and biosensing by a magnetic protein. *Nature communications* **6**, 8721 (2015).
17. Genove, G., DeMarco, U., Xu, H., Goins, W.F. & Ahrens, E.T. A new transgene reporter for in vivo magnetic resonance imaging. *Nature medicine* **11**, 450-454 (2005).
18. Iordanova, B. & Ahrens, E.T. In vivo magnetic resonance imaging of ferritin-based reporter visualizes native neuroblast migration. *NeuroImage* **59**, 1004-1012 (2012).

19. Deans, A.E. et al. Cellular MRI contrast via coexpression of transferrin receptor and ferritin. *Magnetic resonance in medicine* **56**, 51-59 (2006).
20. Bartelle, B.B., Mana, M.D., Suero-Abreu, G.A., Rodriguez, J.J. & Turnbull, D.H. Engineering an effective Mn-binding MRI reporter protein by subcellular targeting. *Magnetic resonance in medicine* **74**, 1750-1757 (2015).
21. Bartelle, B.B., Szulc, K.U., Suero-Abreu, G.A., Rodriguez, J.J. & Turnbull, D.H. Divalent metal transporter, DMT1: A novel MRI reporter protein. *Magnetic resonance in medicine* **70**, 842-850 (2013).
22. Westmeyer, G.G. & Jasanoff, A. Genetically controlled MRI contrast mechanisms and their prospects in systems neuroscience research. *Magnetic resonance imaging* **25**, 1004-1010 (2007).
23. Airan, R.D. et al. MRI biosensor for protein kinase A encoded by a single synthetic gene. *Magnetic resonance in medicine* **68**, 1919-1923 (2012).
24. Gilad, A.A. et al. Artificial reporter gene providing MRI contrast based on proton exchange. *Nature biotechnology* **25**, 217-219 (2007).
25. Gilad, A.A., Winnard, P.T., Van Zijl, P. & Bulte, J. Developing MR reporter genes: promises and pitfalls. *NMR in biomedicine* **20**, 275 (2007).
26. Gilad, A.A. et al. MRI reporter genes. *Journal of nuclear medicine : official publication, Society of Nuclear Medicine* **49**, 1905-1908 (2008).
27. Minn, I. et al. Tumor-specific expression and detection of a CEST reporter gene. *Magnetic resonance in medicine* **74**, 544-549 (2015).
28. Shapiro, M.G. et al. Genetically encoded reporters for hyperpolarized xenon magnetic resonance imaging. *Nature chemistry* **6**, 629-634 (2014).
29. Shapiro, M.G., Szablowski, J.O., Langer, R. & Jasanoff, A. Protein Nanoparticles Engineered to Sense Kinase Activity in MRI. *Journal of the American Chemical Society* **131**, 2484-2486 (2009).
30. Shapiro, M.G. et al. Directed evolution of a magnetic resonance imaging contrast agent for noninvasive imaging of dopamine. *Nature biotechnology* **28**, 264-270 (2010).
31. Matsumoto, Y. & Jasanoff, A. Metalloprotein-based MRI probes. *FEBS letters* **587**, 1021-1029 (2013).
32. van Zijl, P. & Yadav, N.N. Chemical exchange saturation transfer (CEST): what is in a name and what isn't? *Magnetic resonance in medicine* **65**, 927-948 (2011).
33. Kim, J.-W., Kim, Y., Cheong, H. & Ito, K. Manganese induced parkinsonism. *Journal of Korean medical science* **13**, 437-439 (1998).
34. Caravan, P., Ellison, J.J., McMurry, T.J. & Lauffer, R.B. Gadolinium (III) chelates as MRI contrast agents: structure, dynamics, and applications. *Chemical reviews* **99**, 2293-2352 (1999).
35. Silva, A.C., Lee, J.H., Aoki, I. & Koretsky, A.P. Manganese-enhanced magnetic resonance imaging (MEMRI): methodological and practical considerations. *NMR in biomedicine* **17**, 532-543 (2004).
36. Cacheris, W.P., Quay, S.C. & Rocklage, S.M. The relationship between thermodynamics and the toxicity of gadolinium complexes. *Magnetic resonance imaging* **8**, 467-481 (1990).
37. Wolf, G. & Baum, L. Cardiovascular toxicity and tissue proton T1 response to manganese injection in the dog and rabbit. *American journal of roentgenology* **141**, 193-197 (1983).

38. Pfeuffer, J., Flögel, U., Dreher, W. & Leibfritz, D. Restricted diffusion and exchange of intracellular water: theoretical modelling and diffusion time dependence of 1H NMR measurements on perfused glial cells. *NMR in biomedicine* **11**, 19-31 (1998).
39. Pfeuffer, J., Flögel, U. & Leibfritz, D. Monitoring of cell volume and water exchange time in perfused cells by diffusion-weighted 1H NMR spectroscopy. *NMR in biomedicine* **11**, 11-18 (1998).
40. Thelwall, P.E., Grant, S.C., Stanisz, G.J. & Blackband, S.J. Human erythrocyte ghosts: exploring the origins of multiexponential water diffusion in a model biological tissue with magnetic resonance. *Magnetic resonance in medicine* **48**, 649-657 (2002).
41. Winston, G.P. The physical and biological basis of quantitative parameters derived from diffusion MRI. *Quantitative imaging in medicine and surgery* **2**, 254-265 (2012).
42. Padhani, A.R. et al. Diffusion-Weighted Magnetic Resonance Imaging as a Cancer Biomarker: Consensus and Recommendations. *Neoplasia* **11**, 102-125 (2009).
43. Le Bihan, D. & Iima, M. Diffusion magnetic resonance imaging: what water tells us about biological tissues. *PLoS Biol* **13**, e1002203 (2015).
44. Neil, J.J. Diffusion imaging concepts for clinicians. *Journal of magnetic resonance imaging : JMRI* **27**, 1-7 (2008).
45. Norris, D.G. The effects of microscopic tissue parameters on the diffusion weighted magnetic resonance imaging experiment. *NMR in biomedicine* **14**, 77-93 (2001).
46. Li, H. et al. Time-dependent influence of cell membrane permeability on MR diffusion measurements. *Magnetic resonance in medicine* (2015).
47. van der Weerd, L., Melnikov, S.M., Vergeldt, F.J., Novikov, E.G. & Van As, H. Modelling of Self-diffusion and Relaxation Time NMR in Multicompartment Systems with Cylindrical Geometry. *Journal of Magnetic Resonance* **156**, 213-221 (2002).
48. Szafer, A., Zhong, J. & Gore, J.C. Theoretical model for water diffusion in tissues. *Magnetic resonance in medicine* **33**, 697-712 (1995).
49. Plech, A., Kotaidis, V., Grésillon, S., Dahmen, C. & von Plessen, G. Laser-induced heating and melting of gold nanoparticles studied by time-resolved x-ray scattering. *Physical Review B* **70**, 195423 (2004).
50. Rau, P.R. et al. Apparent diffusion coefficient in the aging mouse brain: a magnetic resonance imaging study. *Life sciences* **78**, 1175-1180 (2006).
51. Stanisz, G.J., Li, J.G., Wright, G.A. & Henkelman, R.M. Water dynamics in human blood via combined measurements of T2 relaxation and diffusion in the presence of gadolinium. *Magnetic resonance in medicine* **39**, 223-233 (1998).
52. Yang, B. & Verkman, A. Water and glycerol permeabilities of aquaporins 1–5 and MIP determined quantitatively by expression of epitope-tagged constructs inXenopus oocytes. *Journal of Biological Chemistry* **272**, 16140-16146 (1997).
53. Agre, P. et al. Aquaporin CHIP: the archetypal molecular water channel. *American Journal of Physiology - Renal Physiology* **265**, F463-F476 (1993).
54. Badaut, J., Fukuda, A.M., Jullienne, A. & Petry, K.G. Aquaporin and brain diseases. *Biochimica et biophysica acta* **1840**, 1554-1565 (2014).
55. Ma, T., Frigeri, A., Tsai, S.-T., Verbavatz, J. & Verkman, A. Localization and functional analysis of CHIP28k water channels in stably transfected Chinese hamster ovary cells. *Journal of Biological Chemistry* **268**, 22756-22764 (1993).

56. Badaut, J. et al. Brain water mobility decreases after astrocytic aquaporin-4 inhibition using RNA interference. *Journal of cerebral blood flow and metabolism : official journal of the International Society of Cerebral Blood Flow and Metabolism* **31**, 819-831 (2011).
57. Fukuda, A.M. et al. Posttraumatic reduction of edema with aquaporin-4 RNA interference improves acute and chronic functional recovery. *Journal of cerebral blood flow and metabolism : official journal of the International Society of Cerebral Blood Flow and Metabolism* **33**, 1621-1632 (2013).
58. Van Zijl, P. et al. Complete separation of intracellular and extracellular information in NMR spectra of perfused cells by diffusion-weighted spectroscopy. *Proceedings of the National Academy of Sciences* **88**, 3228-3232 (1991).
59. Kärger, J. Principles and applications of self-diffusion measurements by nuclear magnetic resonance. *Adv Magn Reson* **12**, 1-89 (1988).
60. Holz, M., Heil, S.R. & Sacco, A. Temperature-dependent self-diffusion coefficients of water and six selected molecular liquids for calibration in accurate 1H NMR PFG measurements. *Physical Chemistry Chemical Physics* **2**, 4740-4742 (2000).
61. Nilsson, M. et al. Noninvasive mapping of water diffusional exchange in the human brain using filter-exchange imaging. *Magnetic resonance in medicine* **69**, 1572-1580 (2013).
62. Ahrens, E.T. & Bulte, J.W. Tracking immune cells in vivo using magnetic resonance imaging. *Nature reviews. Immunology* **13**, 755-763 (2013).
63. Srivastava, A.K. et al. Advances in using MRI probes and sensors for in vivo cell tracking as applied to regenerative medicine. *Disease models & mechanisms* **8**, 323-336 (2015).

Chapter 3

MAPPING THE MICROSCALE ORIGINS OF MRI CONTRAST WITH SUBCELLULAR DIAMOND MAGNETOMETRY

Davis, H.C.† , Ramesh, P.† et al. (2018). "Mapping the microscale origins of magnetic resonance image contrast with subcellular diamond magnetometry". *Nature Communications* 9, 131. doi:10.1038/s41467-017-02471-7

3.1 Introduction

Magnetic resonance imaging (MRI) is a widely used biomedical imaging modality, with millions of scans performed each year for medical diagnosis, human neuroscience research and studies in animal models. The contrast seen in MRI images is strongly influenced by microscale magnetic field gradients in cells and tissues, produced by endogenous substances such as blood, cellular iron deposits (1, 2), or molecular imaging agents such as iron oxide nanoparticles (IONs) (3-6). The precise dependence of voxel-scale (~ 0.5 mm) MRI contrast on the microscale magnetic field has been a topic of intense theory and simulation due to its importance for disease diagnosis and contrast agent design (2, 7-10). These studies predict, for example, that the spatial frequency of the local magnetic field can significantly impact the T_2 relaxation rate of a tissue, and that optimizing contrast agent size can maximize T_2 contrast for a given set of material and imaging parameters. However, despite its significance for biological imaging, the relationship between microscopic magnetic field patterns in tissue and T_2 relaxation has not been studied experimentally due to a lack of effective methods to map magnetic fields at the microscale under biologically relevant conditions.

Here, we establish a new method to study the connection between subcellular magnetic fields and MRI contrast using nitrogen vacancy (NV) magnetometry, a recently developed technique that enables the imaging of magnetic fields with optical resolution using the electronic properties of fluorescent NV quantum defects in diamond (11). The electronic structure of an NV center forms a ground-state triplet, with the $m_s = \pm 1$ states separated from the $m_s = 0$ state by 2.87 GHz, making ground-state spin transitions addressable by standard electron spin resonance (ESR) techniques. The Zeeman energy difference between the +1 and -1 states leads to the splitting of the 2.87 GHz resonance into two distinct energy levels, whose separation from each other increases linearly with magnetic field strength. Upon green laser excitation (532 nm), the $m_s = \pm 1$ states are more likely to undergo non-radiative relaxation than the zero-spin state, so that microwave-induced transitions from $m_s = 0$ to $m_s = \pm 1$ cause a drop in NV fluorescence. Thus, the local magnetic field of an NV center can be extracted from the optically reported ground-state spin transition frequency. Diamonds densely doped with NV centers make it possible to optically image this resonant transition frequency over a wide field of view, thus providing an Abbe-limited image of the magnetic field at the diamond surface (12).

NV magnetometry has recently been used in proof-of-concept biological applications such as imaging the magnetic fields produced by magnetotactic bacteria (13), detecting magnetically labeled cancer cells (14), visualizing paramagnetic ions bound to cells(15), and measuring magnetic fields produced by neuronal action potentials (16). However, to date this technology has not been used to map subcellular magnetic fields in living mammalian cells or to connect these maps to *in vivo* diagnostic imaging modalities such as MRI. Doing so requires adapting NV magnetometry for high-sensitivity imaging of sparse magnetic fields in cells and tissues, developing methods to convert 2-D NV data into the 3-D distribution of magnetic field sources and simulating the behavior of nuclear spins in the resulting magnetic fields. In addition, monitoring the evolution of magnetic fields in live cells requires operating under non-damaging optical and thermal conditions with reduced available signal. In this work, we address these challenges to enable the mapping of sub-cellular magnetic fields in an *in vitro* model of macrophage iron oxide endocytosis and histological samples from a mouse model of liver iron overload, connecting both to MRI contrast.

3.2 Results

3.2.1 Mapping sub-cellular magnetic fields

Our home-built NV magneto-microscope (**Fig. 3.1a**) was optimized for both high-resolution magnetic field imaging of fixed samples and dynamic imaging of living cells. By virtue of a relatively thick NV layer in our diamond (~4 µm), we were able to significantly reduce the applied laser power compared to shallower surface-implanted NV diamond microscopes, while maintaining a strong NV fluorescent signal for rapid imaging. We used a total internal reflection geometry to minimize phototoxicity (13, 16) and bonded a silicon carbide wafer to the diamond base to improve thermal dissipation (16). For cell imaging experiments, we applied a moderate bias field (~10 mT) to magnetize cell-internalized superparamagnetic IONs. While a larger bias field would increase the magnetization of the sample, it would also produce stronger off-axis magnetic fields for each NV axis, which significantly reduces the sensitivity of NV magnetometry(17).

As a first test of our method, we imaged the magnetic fields resulting from the endocytosis of superparamagnetic IONs by murine RAW 264.7 macrophages. Magnetic labeling and *in vivo* imaging of macrophages is under development for a variety of diagnostic and therapeutic applications (4, 18-20), which could benefit from an improved understanding of the resulting MRI contrast. In particular, although labeling is typically done with dispersed particles of sizes ranging from a few nanometers to several microns(21-23), their internalization and subsequent compaction by the cell (**Fig. 3.1, b-c**) could produce radically different magnetic field profiles (8-10), which cannot be directly observed by conventional electron microscopy or iron staining techniques. We performed vector magnetometry on fixed macrophages after incubating them for one hour with 200 nm, multi-core IONs and allowing one additional hour for internalization. After measuring the magnetic field along each of the four NV orientations (**Fig. 3.1d**), we projected the field maps along Cartesian axes convenient for magnetic dipole localization via orthogonalization and tensor rotation (**Fig. 3.1e**).

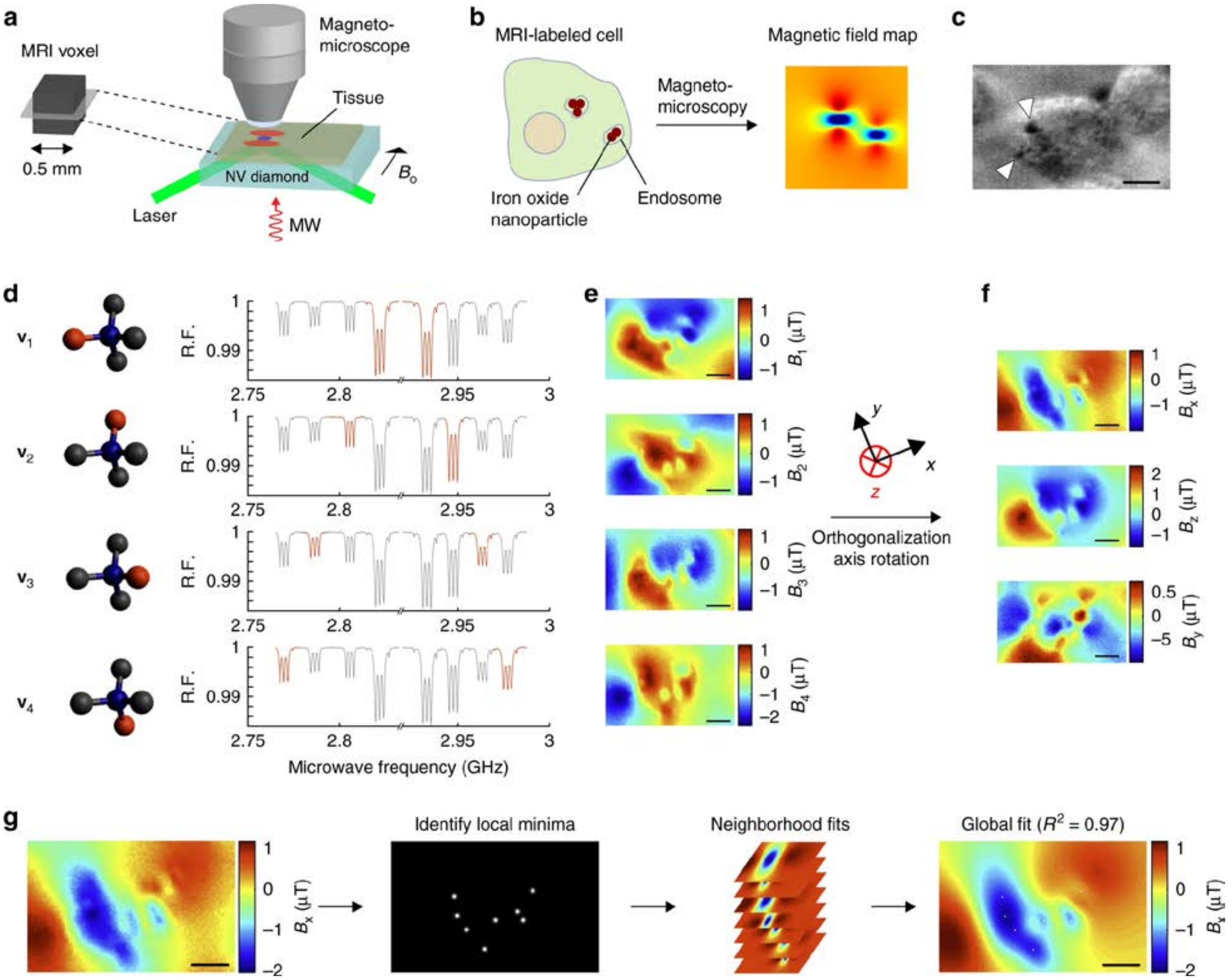

Figure 3.1 Subcellular mapping of magnetic fields in cells labeled for MRI. a Schematic of subvoxel magnetic field mapping using a NV magneto-microscope. **b** Illustration of a cell labeled with IONs and its expected magnetic field pattern. **c** Bright-field image of RAW 264.7 macrophage labeled with 200- nm IONs. White arrows point to internalized IONs. A bright-field imaging artifact also appears as black in the upper right corner of the cell. **d** Cartoon representation of each NV orientation and the corresponding representative spectra from fixed-cell experiments. The blue ball represents nitrogen and the red ball represents the adjacent lattice vacancy. Highlighted peaks in each relative fluorescence (RF) spectrum show the transition corresponding to each of the four orientations. **e** Magnetic field images of the field projections along each of the four NV axes of macrophages 2 h after initial exposure to 279 ng ml^{-1} 200- nm IONs. **f** Images in **e** converted via Gram–Schmidt orthogonalization and tensor rotation to field maps along three Cartesian coordinates with the *z* axis defined perpendicular to the diamond surface and the *x* axis defined as the projection of the applied bias field onto the diamond surface plane. The *y* axis is defined to complete the orthogonal basis set. **g** Representative example of the procedure for dipole localization in cellular specimens. This procedure comprises three steps: first the local minima in the field map are identified and ranked; next, in decreasing order of magnitude, the neighborhood of each local minimum is fit to a point dipole equation and the resulting field is subtracted from the field map to reduce the fit-deleterious effect of overlapping dipole fields; and finally, the results of

these fits are used as guess parameters for a global fit over the full field of view. The fit shown has a degree-of-freedom-adjusted R^2 of 0.97. Scale bars are 5 μm

3.2.2 Connecting microscale fields to MRI contrast

To connect microscale magnetic field measurements to MRI contrast, we first converted our 2-D images to 3-D maps of magnetic field sources in the sample, then simulated the behavior of aqueous nuclear spins in the corresponding 3-D field. To convert 2-D vector maps imaged at the diamond surface into a 3-D model of magnetic fields in cells above the diamond, we developed an algorithm for iterative localization of magnetic dipoles (**Fig. 3.1f**, **Supplementary Fig. 3.S1**). First, the in-plane coordinates of putative dipole field sources (*e.g.,* clusters of magnetic particles) were identified from local minima in the x-component of the vector field, chosen parallel to the projection of the bias field onto the diamond surface. Then, the off-diamond height (z) and magnetic moment of each cluster were determined by fitting the local dipole field profile. After fitting the dipole at the strongest local minimum, the resulting magnetic field pattern was subtracted, and the next strongest local minimum fitted, with this process repeated until all local minima were exhausted. A global fit was then performed using the results from the local fits as starting parameters. The degree-of-freedom-adjusted R^2 for all the global fits made to 6 representative particle-containing cells was greater than 0.90. Magnetic localization of nanoparticle clusters was confirmed in a separate set of cells using fluorescently labeled nanoparticles (**Supplementary Fig. 3.S8**). In addition, independent measurements of intracellular iron concentration using inductively coupled plasma mass spectroscopy, 1.09 ± 0.10 pg Fe per cell, corroborated the estimated iron content inferred from NV measurements, which was 1.126 pg Fe per cell. The final dipole values were scaled from the 10 mT bias field of the NV instrument to the 7 T field of our MRI scanner using the bulk magnetization curve of the IONs (**Supplementary Fig. 3.S2**).

To translate sub-cellular magnetic field maps into predictions about MRI contrast, we performed Monte Carlo simulations of nuclear spin T_2 decoherence in lattices of representative cells. These cells contained magnetic dipole distributions and magnitudes derived from NV magnetometry of a representative cellular library (**Fig. 3.2a**, **Supplementary Fig. 3.S3**). The resulting lattice thereby contains information about the spatial frequencies of the magnetic field present in the pellet tissue, a critical parameter for T_2 contrast. Importantly, since this information can be obtained from NV measurements performed on a representative sampling of cells or tissues, this obviates the need for NV evaluation of the exact individual sample imaged with MRI, enhancing the versatility of this approach.

Our simulation predicted a bulk MRI T_2 relaxation time of 24.3 ms for a 1:1 mixture of supplemented and unsupplemented cells (**Fig. 3.2b**). Mixing was done to obtain a sufficiently long T_2 for accurate measurement with our MRI system. When compared to an experimental MRI measurement of T_2 in macrophages prepared as in the NV experiment and pelleted in a 1:1 mixture with unsupplemented cells, the Monte Carlo prediction was accurate to within 2.8% (**Fig. 3.2, c-d**). Importantly, the T_2 relaxation time of the cell pellets could not have been predicted solely from the concentration of IONs in the sample, as previous simulations have suggested a major influence of packing geometry on contrast agent relaxivity (8-10). To establish that this relationship also holds for our model system, we performed MRI measurements and Monte Carlo simulations with IONs distributed in the extracellular space (**Fig. 3.2e**). Per iron mass, we found that this diffuse extracellular arrangement produces approximately 6.63-fold faster T_2 relaxation than do endocytosed particles (**Fig. 3.2f**), underlining the importance of the microscale magnetic field patterns mapped with our method. Simulations of additional particle distributions, shown in **Supplementary Fig. 3.S7**, examine the relative influence of particle clustering and confinement inside cells and endosomes.

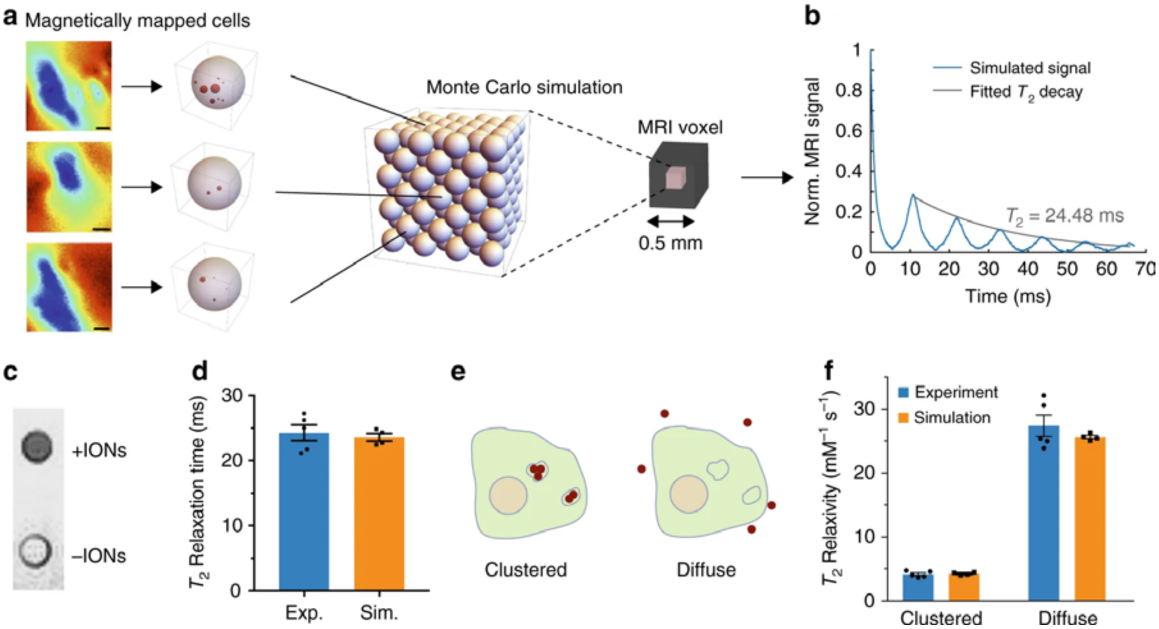

Figure 3.2 Predicted and experimental MRI behavior in cells. a Schematic of Monte Carlo modeling of spin relaxation using NV-mapped magnetic fields. A library of 11 cells mapped with vector magnetometry (three representative cells shown) in a 1:1 mix with unlabeled cells, was used to randomly fill a 108-cell FCC lattice with periodic boundary conditions and run a Monte Carlo simulation of spin-echo MRI to predict T_2 relaxation behavior. **b** Representative simulated MRI signal. **c** T_2-weighted MRI image of cell pellets containing a 1:1 mixture of supplemented and unsupplemented cells (+ IONs and –IONs, respectively) or 100% unlabeled cells (bottom). **d** Simulated and experimentally measured T_2 relaxation times for the 1:1 mixture. **e** Illustration of the same quantity of magnetic particles endocytosed or distributed in the extracellular space. **f** Simulated and experimentally measured relaxivity for endocytosed and extracellular distributions of IONs. Measurements and simulations have $N = 5$ replicates. All error bars represent ± SEM

3.2.3 Mapping magnetic fields in histological specimens

To extend this technique to diagnostic imaging, we performed NV magnetometry on liver specimens from a mouse model of hepatic iron overload. The spatial distribution of iron deposits in the liver and other tissues has been a topic of interest in clinical literature as an indicator of disease state, including efforts to discern it noninvasively using MRI (2). Iron overload was generated through intravenous administration of 900 nm IONs to C57bl/6 mice (**Fig. 3.3a**) to produce efficient iron loading of the liver detectable by MRI. Livers were harvested 18 hours after injection and imaged with 7 T MRI, showing enhanced macroscale T_2 relaxation compared to controls (**Fig. 3.3b**). To investigate the microscale nature of this contrast enhancement, we cryosectioned the livers of saline- and iron-injected mice and imaged the magnetic field profiles of these tissue sections on our NV magneto-microscope. We measured the projection of the magnetic field along a single NV orientation, probing the m_s=0 to m_s=+1 and m_s=0 to m_s=–1 transitions. The magnetic particle clusters were relatively sparse, resulting in a punctate distribution of magnetic dipoles within the liver tissue of the iron-overloaded mouse (**Fig. 3.3c**, **Supplementary Fig. 3.S4**). We confirmed that these magnetic fields resulted from IONs using fluorescent imaging, for which purpose the IONs were labeled with a fluorescent dye. These results suggest that NV magnetometry could be used to map sub-voxel magnetic field patterns within histological specimens, increasing the diagnostic power of MRI by correlating magnetic field distributions to disease state.

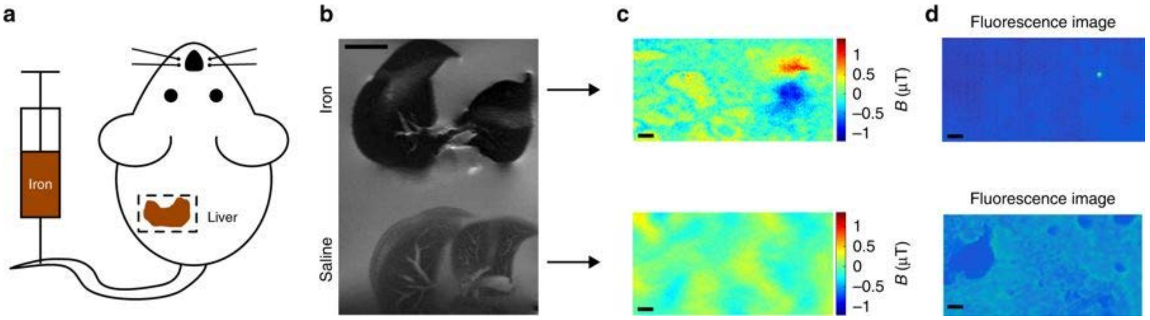

Figure 3.3 Magnetometry of histological samples. a Diagram of mouse model of iron overload, prepared by injecting 10 mg kg^{-1} of 900 nm iron oxide nanoparticles into the tail vein. **b** 7T T_2-weighted MR image of fixed, excised mouse livers from mice injected with IONs or saline. **c** NV magnetic field maps of 10 μm liver sections obtained from the mice in **b**. **d** Fluorescence images of the tissue samples in **c**. Fluorescence images were taken with autogain to reduce the necessary exposure time, resulting in the visibility of the autofluorescence of the tissue in the saline control. Magnetometry scans were taken with a fixed gain. This experiment was repeated a total of three times, with data from two additional experiments shown in Supplementary Fig. 3.S6. Scale bars in **b** and **c**–**d** are 5 mm and 10 μm, respectively

3.2.4 Magnetic imaging of endocytosis

Finally, we tested whether NV magnetometry could be used to follow the magnetic consequences of the dynamic redistribution of magnetic material in living mammalian cells. Macrophages endocytosing IONs go through several stages of internalization, gradually reconfiguring diffuse particles into compacted lysosomal clusters (**Fig. 3.4a**). This process could be relevant to interpreting MRI data from labeled macrophages and to the development of clustering-based magnetic nanoparticle contrast agents (24, 25). To image living cells, we adjusted our NV methodology to minimize optical and thermal energy deposition. We sub-sampled the NV spectrum to probe only the m_s=0 to m_s=+1 transition of one NV orientation and limited laser illumination to 5 minutes per image. This allowed us to generate time-lapse images of magnetic fields coalescing inside macrophages after ION internalization (**Fig. 3.4, b-c**, **Supplementary Figs. S5-S6**), at the expense of precise 3-D source localization, which requires vector magnetometry using multiple NV orientations. Cell viability (assessed via a Trypan Blue exclusion assay) was ~90%. To our knowledge, this represents the first magnetic field imaging of a dynamic process in living mammalian cells, and could aid the development of dynamic contrast agents for MRI.

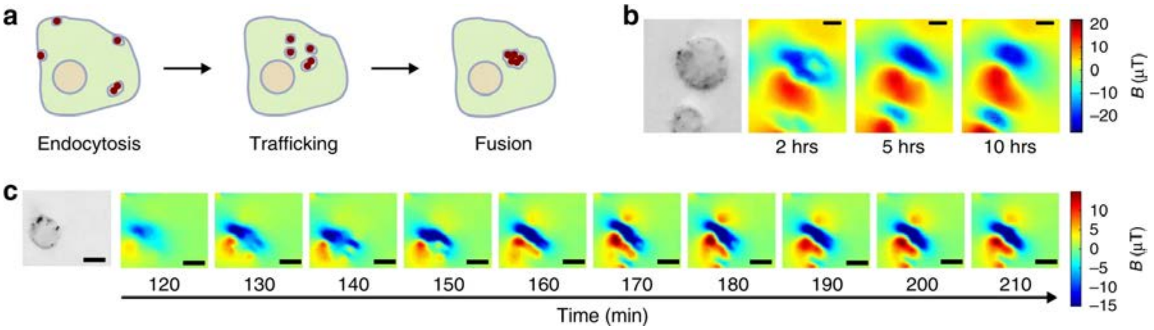

Figure 3.4 Dynamic magnetic microscopy in live mammalian cells. a Cartoon showing the typical progression of endocytotic uptake of IONs. **b** Bright field and series of time-lapse magnetic field images of RAW macrophages over 10 h. Three additional replicates are shown in Supplementary Fig. 3.S7. **c** Bright field and series of time-lapse magnetic field images of a RAW macrophage with 10 min between magnetic field images. Two additional replicates of this experiment are shown in Supplementary Fig. 3.7. Scale bars are 5 μm

3.3 Discussion

In summary, this work establishes the capability of subcellular NV diamond magnetometry to map microscale magnetic field patterns in mammalian cells and tissues and introduces computational methods to connect these patterns to MRI contrast. The ability to make this connection experimentally will facilitate the interpretation of noninvasive images through microscopic analysis of matching histological specimens and aid the development of magnetic contrast agents for molecular imaging and cellular tracking. Alternative methods for magnetic measurement, such as scanning SQUID microscopy(26, 27) and magnetic force microscopy(28, 29), are more difficult to apply to tissue-scale biological specimens due to the need to raster scan samples, the spatial offsets required for thermal insulation of SQUID magnetometers from biological materials, and the need to penetrate samples with probe tips for force microscopy. Meanwhile, methods such as electron microscopy or iron staining, which can also reveal the *in vitro* locations of putative magnetic materials based on their density or atomic composition, contain no information about the magnetic properties of such materials and their resulting fields, limiting the utility of these methods to examining the distribution of known magnetic field sources.

Although the present study also used known particles to enable direct experimental validation of our methods, NV magnetometry can in principle be used to measure magnetic field profiles arising from unknown sources, such as biomineralized iron oxide. To enable such measurements, NV imaging could be performed with a variable, electromagnet-driven bias field to first map the locations of magnetic field sources at low field (where vector magnetometry is possible), then apply a ramping field along a single NV axis to assess the M *vs*. H behavior of each field source. Such *in situ* saturation curves would provide the information needed to model MRI relaxation in samples with unknown saturation behavior. Additional improvements in this technique may be needed to reconstruct the location and magnetization of more diffuse magnetic materials that are less easily detected as point dipoles.

The sensitivity of our current instrument, established by computing the variance between 3 sequential magnetic measurements of the identical sample, was 17 nT at 1 µm in-plane resolution. This sensitivity corresponds to the field produced by a 92 nm particle situated 10 µm above the diamond surface (assuming the same volumetric magnetization as the IONs used in this study), or a 10 nm particle located immediately on top of the diamond. This sensitivity was more than sufficient to detect the 200 nm IONs used in our proof-of-concept experiments. While these particles are within the size range used in MRI contrast agents (21-23), future work should focus on improving the sensitivity of NV magnetometry and demonstrating detection of smaller sources. Sensitivity could be improved by employing diamonds with thinner NV layers, which would allow detection of significantly smaller magnetic sources near the diamond surface and would reduce the point spread function of NV-imaged magnetic fields, increasing the precision of source localization. Combined with improved methods for positioning tissue sections flatter on the diamond surface, this would allow the mapping of fields produced by smaller, endogenous magnetic inclusions and ultrasmall superparamagnetic nanoparticles.

The study of microscale sources of T_2 contrast could be complemented by methods to map the concentrations of T_1 contrast agents using alternating current (AC) NV magnetometry(15). In particular, adapting this technique to measure the 3-D distribution of T_1 agents inside of the cell using nanodiamonds(30, 31) could enable Monte Carlo modeling of T_1 relaxation in contrast-labeled cells and tissues. In addition to mapping the distribution of contrast agents and resultant magnetic fields, recent advances in NV magnetometry could allow for *in situ* imaging of water-bound proton relaxation, enabling a direct measurement of the effect of contrast agents on the relaxation of surrounding water molecules(32).

Besides contributing to the study of MRI contrast, the methods presented for mapping magnetic field sources in 3-D from planar optical data will enable biological imaging applications directly using NV diamonds and magnetic labels. Because the optical readout in this technique is confined to the diamond surface, this method can be used to study opaque tissues inaccessible to conventional microscopy. To this end, our demonstration that time-resolved wide-field NV magnetic imaging can be performed on living cells increases the utility of this technique for monitoring dynamic biological processes.

3.4 Materials and Methods

3.4.1 Nitrogen Vacancy Magneto-Microscope

The NV magneto-microscope was constructed from a modified upright Olympus microscope and a 532 nm laser source. The diamond used in this work is an electronic grade (N < 5ppb) single crystal substrate with nominal rectangular dimensions of 4.5 mm x 4.5 mm x 500 μm, grown using chemical vapor deposition (CVD) by Element Six. The top-surface NV sensing layer is measured to be 3.87 μm thick, consists of 99.999% isotopically pure ^{12}C with 21.4 ppm ^{14}N ($3.77*10^{17}$ cm^{-3}) incorporated into the layer during growth. Layer thickness and nitrogen concentration were determined by secondary ion mass spectroscopy. The diamond was irradiated with a 4.5 MeV electron source with an irradiation dose of 9 x 10^{18} cm^{-2}. The samples were subsequently annealed at 400 ºC for 2 hrs, 800 ºC for 16 hrs and 1200 ºC for 2 hrs. This diamond was affixed to a silicon carbide wafer (for enhanced heat dissipation), which was in turn affixed to a pair of triangular prisms to facilitate a total internal reflection excitation path. The prisms, silicon carbide wafer and diamond were fused using Norland Optical Adhesive (NOA 71). The diamond assembly was removable to allow live cell culture on the diamond surface in a cell culture incubator. Light was collected from the top of the diamond through a water-immersion objective. Images were acquired on a Basler acA2040-180kmNIR - CMV4000 CCD camera with 2048x2040 5.5 µm pixels (we used 256x1020 pixels to increase frame rate). For high-resolution vector magnetometry and tissue imaging, NV fluorescence was excited using a 100 mW Coherent OBIS LS 532 nm optically pumped semiconductor laser. For live cell imaging, we used an attenuated 2 W 532 nm laser from Changchun New Industries Optoelectronics. When necessary, focal drift was adjusted for using a piezo-driven stage (Thorlabs). Microwave radiation was applied through a single turn copper loop immediately surrounding the diamond. The microwave signal was generated by a Stanford Research Systems Inc. SG384 signal generator and amplified by a ZHL-16W-43-S+ amplifier from MiniCircuits. Experimental timing was controlled by a National Instruments USB 6363 X Series DAQ. A bias magnetic field was generated by two NeFeB grade N52 magnets (1”x2”x.5”, K&J Magnetics) positioned on opposite sides of the NV diamond. The NV setup was controlled by custom software written in LabView.

3.4.2 Cell Culture

RAW 264.7 cells (ATCC) were cultured at 37º C and 5% CO_2 in DMEM (Corning Cellgro) and passaged at or before 70% confluence. For particle labeling, media was aspirated and replaced with phenol red-free DMEM supplemented with 279 ng/ml IONs (200 nm Super Mag Amine Beads Ocean Nanotech, MHA). After one hour, the ION solution was aspirated and cells were washed twice with PBS to remove unbound particles. For fixed-cell magnetometry, the cells were trypsinized quenched with DMEM and deposited on the diamond surface at 40-70% confluency. After a 1 hour incubation on the diamond under ambient conditions, the cells were fixed with 4 % paraformaldehyde-zinc fixative (Electron Microscopy Services) and washed twice with PBS.

For live cell imaging, the cells were cultured as above until trypsinization and spotting on the diamond. Their media was supplemented with 0.1 mM ascorbic acid to mitigate phototoxicity (33). For extended imaging (Supplementary Fig. 3.S3a), the cells were maintained on the diamond in DMEM supplemented with 10 mM HEPES to stabilize pH at 7.4 under ambient atmosphere.

3.4.3 Vector Magnetometry

The bias magnetic field was aligned close to in-plane with the diamond surface while having sufficient out-of-plane field strength to resolve the resonance of each NV axis, and the full NV optically detected magnetic resonance (ODMR) spectrum was probed. The out-of-plane component was necessary because a purely in-plane bias field did not provide each NV axis with a unique parallel B-field, causing absorption lines to overlap. The microwave resonance for each pixel in the image was set as the center of the middle hyperfine peak of the transition. Spectra were swept at 0.5 Hz with 2000 images acquired per spectrum (0.9 ms exposure time). Images were acquired with an Olympus 60x water immersion objective (NA 1.0). Magnetometry spectra were acquired for 2 hours each. For a sub-set of measurements, this time was extended to 6 hours to improve SNR.

Projection field maps for each NV orientation were generated from the corresponding peaks in the NV ODMR spectrum, and the background magnetic gradient from the bias magnets (32 μT/mm in a representative scan) was subtracted out by fitting the background to a 2D quadratic function and subtracting the fit from the signal. Projection field maps were combined to form 3 orthogonal field maps with B_z oriented normal to the diamond sensing surface. B_x is defined as the projection of the applied field onto the diamond plane and B_y is defined along the vector that completes the orthogonal set. Pixels were binned 2x2 in postprocessing to boost SNR. (This does not cause a significant reduction in resolution as the binned pixels in the object plane are 92 nm on a side, which oversamples the Abbe limit of ~340 nm.)

3.4.4 Live Cell Magnetometry

For live cells, the bias magnetic field was aligned such that it was possible to resolve at least one NV resonance, and the magnetic field projection along a single NV orientation was probed using the $m_s = 0 \rightarrow m_s = +1$ transition. The microwave resonance for each pixel in the image was set as the center of the middle hyperfine peak of the transition. While probing only one NV transition allowed us to reduce the light dose to the sample while maintaining good SNR, it also limited our information to a projection of the field along one axis. This limitation precludes the source fitting performed on the fixed samples. Spectra were swept ~10 MHz at 1 Hz with 200 images acquired per spectrum (4 ms exposure time). In order to limit phototoxicity, each image was averaged for only 5 minutes and the laser was shuttered for five minutes in between images, resulting in a 50% duty cycle. Regions of interest were selected to include all relevant fields for a given cell. Optical power density was ~40 W/cm^2. Images were acquired with a Zeiss 40x near infrared water immersion objective (NA 0.8). Cell viability was assessed by performing a Trypan Blue exclusion assay after NV measurements.

3.4.5 Intracellular Iron Quantification

We performed inductively coupled plasma mass spectrometry (ICP-MS) to independently confirm the intracellular iron concentration estimated by NV magnetometry. RAW 264.7 cells were cultured and labeled with IONs as described above. After trypsinizing, the cells were counted using a disposable hemocytometer (InCYTO C-Chip). The cells were then pelleted at 400 g for 5 min, and the supernatant was aspirated. The cell pellet was first boiled in 2 mL of 70% nitric acid (ICP grade, Sigma) for 24 hrs to completely oxidize and dissolve any intracellular iron. The dried residue was then resuspended in 2% nitric acid and diluted 10-fold with deionized water for analysis using an Agilent ICP-MS quadrupole spectrometer. Unsupplemented cells contained 0.21+/- 0.04 pg Fe per cell. A procedural blank was included throughout the process to account for background iron contamination (~ 34 ppb), which was subtracted from measured samples.

3.4.6 Field Fitting and Dipole Localization

In-plane dipole coordinates were identified as local minima in the B_x field map. Before localization, the field map was spatially low-passed (2D Gaussian filter with σ = 0.5 pixels) to eliminate noise-generated local minima in the background. A pixel was identified as a local minimum if and only if its B_x field value was smaller than all of its immediate neighbors (including diagonals) in the spatially low-passed image.

Starting with the strongest local minimum, the measured magnetic field in a 10x10 pixel (~1.8x1.8 µm) square surrounding this minimum was fitted to a point dipole equation and averaged through the full NV layer depth (assuming uniform NV density), with the magnetic moment, height off of the diamond, and dipole orientation as free parameters.

$$B_x(i,j) = \frac{\int_{-z}^{-(z+h)} B_{xo}(i',j',b,M,\theta,\phi) \cdot db}{-h}$$

where

$$B_{xo}(i,j) = \frac{\mu_0}{4\pi} \cdot \left(\frac{3\,x\,(\boldsymbol{M} \cdot \boldsymbol{r})}{r^5} - \frac{\boldsymbol{M} \cdot \hat{x}}{r^3}\right)$$

Here i'=(i-i_0) and j'=(j-j_0) where (i_0,j_0) are the in-plane coordinates of the magnetic dipole, θ and ϕ correspond to the two rotational degrees of freedom available to a point dipole, M is the magnetic moment, z is the height of the dipole over the diamond, **r** is the displacement vector, $\hat{x}$ is the unit vector along the projection of the dipole axis onto the diamond surface plane, $x = i' \cos(\theta) - j' \sin(\theta)$, b is a dummy variable for integration through the NV layer, and h is the NV layer thickness. All parameters are free to fit other than the in-plane dipole coordinates, which are fixed by the local minimum of the B_x field map. While the z offset between the dipole and the diamond and the magnetic moment of the dipole both affect the strength of the detected field, they have distinguishable effects on the resultant field pattern. This is clear from the distinct dependence of the dipole function on **M** and r, as shown in the Supplementary Information.

After the strongest minimum has been fitted, the fitted field from the fit dipole (within the full field of view) was subtracted from the magnetic field image, to facilitate the fitting of weaker dipoles. The 10x10 pixel neighborhood of the second strongest dipole was then fitted in the subtracted image. The fitted field was subtracted, and the fitting continued until the list of local minima had been exhausted.

A global fit was then performed using the results from the neighborhood fits as starting parameters. The global fit function is the sum of N dipoles (where N is the number of local minima) with the in-plane dipole coordinates fixed at the local minima.

$$B_{x_{tot}}(i,j) = \sum_{q} B_{x_q}(i,j)$$

Here q is an index that runs from one to N and indicates the dipole field source. The precision of this technique is limited by the key assumption that the local minima are not significantly shifted in the x-y plane by neighboring dipoles. The degree of freedom-adjusted R^2 for each of the four global fits in the cell library was greater than 0.9. (For 3 of the 6 labeled cells, with image acquisition time increased from 2 to 6 hours, the R^2 was greater than 0.95). While this approach was able to produce a sufficiently precise magnetic field reconstruction to predict MRI relaxation, other methods are also available for analytic dipole localization and magnetic field reconstruction(34).

3.4.7 Monte Carlo Simulations & Cell Library

Nuclear spin relaxation was simulated by assigning 11 representative cells from vector magnetometry to random positions in a repeating face-centered cubic (FCC) lattice containing a total of 108 spherical cells with periodic boundary conditions. The intracellular volume fraction of this packing geometry is 74%. While spherical cells in a periodic lattice represent a geometric simplification compared to real tissues, this and similar simplifications have been used previously to model diffusion in cell pellets and tissues(35-37). Cell size was set to match previously measured values for RAW 264.7 cells(38). Water molecules were randomly assigned initial x, y, and z coordinates in the lattice and allowed to diffuse while their phase in the rotating frame evolved from $\phi(0) = 0$ by $\delta\phi(t) = -\gamma B(x, y, z)\delta t$, where $B(x, y, z)$ is the local nanoparticle-induced field. This phase step does not account for inner-sphere effects from water coordinating to the nanoparticle surface. Re-focusing pulses were simulated at 5.5 ms Carr-Purcell time (11 ms echo time) by setting $\phi(t) = -\phi(t - \delta t)$. Adjusting the Carr-Purcell time has been demonstrated to significantly affect the efficacy of the refocusing pulses in T_2 sequences. We used an 11 ms echo time to match the echo time of our cell pellet MR measurements. The magnetic field was mapped within this 3D-volume using a finite mesh whose mesh size was inversely proportional to the local field gradient. If a water molecule moved within a distance equivalent to six nanoparticle cluster radii of a cluster, the field contribution from that cluster was calculated explicitly. Background RAW cell relaxation was accounted for by post-multiplying the simulated signal with an exponential decay with time constant set to the measured relaxation rate of an unlabeled RAW cell pellet. Cell membranes were modeled as semi-permeable boundaries with a permeability of .01 $\frac{\mu m}{ms}$ in accordance with previously measured values for murine macrophage-like cells, adjusted to the temperature in our magnet bore (12.9 ºC)(39). Intracellular and extracellular water diffusivity were set, respectively, to 0.5547 and 1.6642 $\frac{\mu m^2}{ms}$ in accordance with previous studies of cellular diffusion(35, 36, 40) and established values for water diffusivity at 12.9 ºC(41), the temperature of our scanner bore. Bulk spin magnetization in the sample was calculated as $M(t) = \sum_i \cos\,[\phi_i(t)]$, where i is the index of simulated water molecules and the magnetic moment of a single molecule is normalized to 1.

Nanoparticle clusters were modeled as spheres packed so as to occupy three times the volume of their constituent nanoparticles, within the range of measured literature values and grain packing theory (42) (43) (44). To account for the increase in nanoparticle magnetizations at 7T compared to our NV bias field, we scaled dipole magnetization using a SQUID-measured curve (**Supplementary Fig. 3.S2a**). Magnetic dipole coupling effects between particles were neglected, as is valid for our average cluster size and geometry. (See Supplementary Information for further discussion.) Data presented in the manuscript represents the output of N=10 simulations, each containing 20 random arrangements of cells and 2000 water molecules. The number of trials was chosen such that the SEM for our simulations was smaller than the SEM of our corresponding experiments.

To assess the impact of an alternative nanoparticle distribution (Fig. 3.2, e-f), we simulated the same 200 nm nanoparticles, unclustered and distributed randomly in the extracellular space. The presented data comprises N=10 simulations, each containing 20 random arrangements of particles and 2000 water molecules.

3.4.8 MR Imaging and Relaxometry

Imaging and relaxometry were performed on a Bruker 7T MRI scanner. A 72 mm diameter volume coil was used to both transmit and receive RF signals. To measure the T_2 relaxation rate of RAW cells after nanoparticle labeling, the cells were labeled identically to their preparation for NV magnetometry, then trypsonized, resuspended in 10 mL DMEM and pelleted for 5 min at 350 g. DMEM was aspirated and cells were resuspended in 150 µL PBS. The cells were mixed with an equal number of unsupplemented cells during resuspension in PBS to extend the T_2 time of the final pellet, improving the fidelity of the T_2 fit. After transferring the cells to a 300 µL centrifuge tube, the cells were pelleted for 5 min at 350 g. These tubes were embedded in a phantom comprising 1% agarose dissolved in PBS and imaged using a multi-echo spin echo (CPMG) sequence (TR = 4000 ms, TE = 11 ms, 2 averages, 20 echoes, 273x273x1000 µm voxel size). T_2 relaxation was obtained from a monoexponential fit of the first 6 echoes. As an input into Monte Carlo simulations we measured the “background” relaxation of 4 pellets of unsupplemented RAW cells using the same parameters as above, except that since the T_2 was significantly longer we fitted the first 20 echoes.

For the scenario in which nanoparticles are unclustered in the extracellular space, unsupplemented RAW cells were pelleted and re-suspended in PBS supplemented with 100 µg/ml IONs. This concentration was selected to ensure a measurable T_2 and allow both *in silico* and *in cellulo* comparisons between the per-iron relaxation rates of extracellular and internalized particle scenarios. The validity of a per-iron comparison was confirmed by previous studies of the linearity of relaxivity for this size of iron oxide nanoparticles when unclustered (45). To limit endocytosis, cells were moved to the cold MRI bore and imaged immediately after supplementation and pelleting. Imaging parameters were as described above.

3.4.9 Mouse Model of Iron Overload

Animal experiments were conducted under a protocol applowed by the Institutional Animal Care and Use Committee of the California Institute of Technology. Female C57bl/6 mice were injected in the tail vein with 10 mg/kg of dragon green labeled 900 nm ION (Bangs) or saline. A total of three mice were used in this study. No randomization or blinding were needed given the design of the study. 16 hours after injection, the mice were perfused with 2 mL of 10% formalin, and their livers were harvested for MRI or NV magnetometry. MRI was performed on livers embedded in 1 % agarose using the 7T scanner described above, using a spin-echo pulse sequence with TR = 2500, TE = 11 ms, 4 averages, and a 273x273x1000 µm voxel size. For NV magnetometry, the liver was frozen in OCT embedding media and sectioned into 10 µm slices. Sections were mounted in on glass coverslips. We inverted the glass cover slip and pressed the tissue sample against the NV diamond. Silicon vacuum grease was applied at the edge of the cover slip (away from the diamond) to hold the sample against the diamond. After this preparation was complete, PBS was added to the dish to wet the sample. We performed fluorescent imaging to locate magnetic sources in the tissue. As the sources were sparsely distributed, the camera was set to an auto-gain function to allow for short exposure time and rapid scanning. The camera was set back to fixed gain before NV imaging commenced. To compensate for magnetic field sources being further from the diamond due to tissue thickness and/or folds in the sections, NV imaging was performed with a strong (25 mT) bias field applied along a single NV axis. This strong bias field served to increase the magnetization of the magnetic inclusions in the liver. As it was applied along an NV axis, this bias field did not significantly reduce the contrast of the relevant ODMR spectral lines. However, such a strong bias field precludes the use of vector magnetometry. Future improvements to histological sample preparation should increase the sample flatness and bring the magnetic material closer to the diamond surface, allowing for a lower bias field and, as a result, vector magnetometry and source localization. Images were acquired with a Zeiss 40x near infrared water immersion objective (NA 0.8).

3.4.10 Software and Image Processing

All fits and plots were generated in MATLAB. Monte Carlo Simulations were performed in C++ on a Linux High Performance Computing Cluster.

3.4.11 Statistical Analysis

Sample sizes were chosen on the basis of preliminary experiments to have sufficient replicates for statistical comparison. Data are plotted, and values are given in the text, as mean ± S.E.M. Statistical comparisons assumed similar variance.

3.5 Supplementary Notes

Verification that a Live Cell Process was required for nanoparticle trafficking

To ensure that the nanoparticle motion observed in the live cell experiments was due to a live cellular process, we also analyzed particle motion in fixed cells. Figure S5d shows that there was no observable change in the nanoparticle fields over the relevant time-course in fixed cells (~10 hours).

SQUID Magnetometry and Saturation Field Scaling

Strong off-axis fields shift the eigenbasis of the NV spin Hamiltonian from along the NV axis to along the applied field. In this condition, m_s is no longer an eigenstate of the spin Hamiltonian, leading to mixing of the m_s=0 and m_s=+/-1 states. This effect significantly reduces the sensitivity of NV vector magnetometry at bias fields above 10 mT (17). Therefore, all our vector magnetometry experiments were conducted with a 10 mT bias field. To translate these measurements to the 7 T field strength of MRI in Monte Carlo simulations, we scaled the measured magnetic moments from the 10 mT bias field to 7 T using the results of SQUID magnetometry performed on a dried sample containing $\sim 3 * 10^9$ IONs (**Supplementary Fig. 3.S2a**). This scaling works well for large pseudo-spherical clusters, but does not fully account for the difference in inter-particle effects between small clusters of nanoparticles and the dried SQUID sample in a non-saturated field. As has been previously demonstrated, bulk mass magnetization of continuum nanoparticle assemblies M_{Bulk} is reduced from the mass magnetization of a single nanoparticle or a small nanoparticle cluster (M) due to magnetic dipole coupling (46) such that:

$$M_{Bulk} = (1 - \alpha)M \tag{S1}$$

To assess the potential impact of dipole-dipole interactions on the accuracy of our dipole scaling, we estimated it using a Monte Carlo model of magnetic coupling in nanoparticle clusters (**Supplementary Fig. 3.S2b**). Since we used multi-core particles, we assumed that each nanoparticle has many domains and is in thermal equilibrium, allowing us to neglect the complex time-dependence of Neel relaxation for single domains. We spline-interpolated the SQUID magnetization curve in MATLAB, and solved the following many-body problem employing a similar method to one used previously to simulate magnetic dipole coupling (47). Our governing equations are as follows:

$$\boldsymbol{m_i} = S\left[H_{ef,i}\right] = S[\boldsymbol{H_0} + \textstyle\sum_{j \neq i} \boldsymbol{H_j}] \tag{S2}$$

$$\boldsymbol{H_j} = \frac{1}{4\pi}\left(\frac{3\boldsymbol{r_{ij}}(\boldsymbol{m_j} \cdot \boldsymbol{r_{ij}})}{r_{ij}^5} - \frac{\boldsymbol{m_j}}{r_{ij}^3}\right) \tag{S3}$$

Here m_i is the magnetic moment of the ith nanoparticle in the cluster, S[$H_{ef,i}$] is the splined approximation of the SQUID M vs H curve for the effective field at the location of the ith nanoparticle, $H_0 = 7958\frac{A}{m} = 100\ Oe$ is the initial bias field applied to all nanoparticles in the lattice, and $\boldsymbol{r_{ij}}$ separating the ith and the jth nanoparticle. The effect on the mass magnetization of clusters due to dipole coupling is calculated as follows:

1) Nanoparticles are randomly dispersed into a pseudo-spherical arrangement with packing fraction $\eta = .33$. This value is equal to the packing fraction from our Monte Carlo simulation and is within the range of measured values in literature (42) (43).
2) The magnetic moment of each nanoparticle is calculated based on of the bias field H_0.
3) The field at each nanoparticle is calculated as the superposition of the dipole fields from the other nanoparticles in the cluster.
4) In order to enforce a smooth process, the magnetic moment magnitude and orientation of each nanoparticle are adjusted to a weighted average of their value in the previous step and the value calculated from (S2).
5) Steps 3 and 4 are repeated until the effective applied field and the magnetic moment of each nanoparticle are aligned such that $\max_{i\epsilon[1,N]}\{\frac{\|\boldsymbol{m_i}\times\boldsymbol{H_{ef,i}}\|}{\|\boldsymbol{m_i}\|}\} < 10^{-12}$ and the fractional change of each nanoparticle's magnetic moment is less than 10^{-15}.
6) The dipole-coupling induced magnetization's deviation from the bulk measurement is quantified as:

$$\alpha(N) = \frac{(m_{mc}(N) - m_{Bulk}(N))}{m_{mc}(N)} \qquad \text{(S4)}$$

Here $m_{mc}(N)$ is the simulated magnetic moment of a cluster with N particles and $m_{Bulk}(N)$ is the predicted magnetic moment for that cluster applying the bulk mass-magnetization. We assume that a 100 np cluster behaves as bulk.

The results of this simulation are shown in **Supplementary Figure 3.S2c**. The expected difference relative to the bulk measurement is largest for small clusters, where the dipole interaction is not in the continuum limit. However, in all cases it is below 25%, and for the mean cluster size of ~28 nanoparticles measured with our NV magnetometer it is 7.5%. The curve flattens above N=80, validating our treatment of N=100 as a bulk material. Overall, this represents a modest under-estimation of the mass magnetization, meaning that NV measurements would slightly over-estimate the mass of particles in a given cluster at 10 mT, which in turn would cause an over-estimation of the magnetic moment of a given cluster at saturation (7 T). This in turn could help to account for our simulation's ~3% over-estimation of the relaxivity of our "clustered" samples. Future work mapping magnetic fields of nanoparticles could use the presented simulations to better estimate the relaxivity from pseudo-spherical and anisotropic particle clusters.

Packing and Distribution Effects on T2 Relaxivity

In Figure 2 of the main text we evaluated the ability of NV measurement-based Monte Carlo modeling to predict the effect of nanoparticle clustering patterns in cells on T_2 relaxivity compared to unclustered particles distributed in the extracellular space. While these two cases enabled experimental validation of our method, we performed additional *in silico* trials of hypothetical particle geometries to better understand the parameters driving the measured difference in relaxation (Supplementary Fig. 3.S7).

One hypothetical condition (Supplementary Fig. 3.S7a) addresses the significance of extracellular confinement for unclustered nanoparticles by randomly placing unclustered nanoparticles throughout the whole lattice, including intracellular space. Dispersing the particles throughout the entire lattice slightly increases their relaxivity compared to extracellular confinement, from 25.6 +/- .3 $mM^{-1}s^{-1}$ to 27.8+/- .8 $mM^{-1}s^{-1}$. However, this effect is small compared to that caused by endocytosis and clustering (Supplementary Fig. 3.S7d).

Two additional hypothetical conditions utilized clusters drawn from the NV-measured cell library described in the main text. One condition (Supplementary Fig. 3.S7c) examined clustered nanoparticles placed in the extracellular, rather than intracellular, space. Clusters obtained from the NV measurement library were randomly distributed throughout the extracellular space of the cell lattice. This increased T_2 relaxivity from 4.1 ± 0.20 $mM^{-1}s^{-1}$ to 6.7+/-.3 $mM^{-1}s^{-1}$ compared to the cell-confined intracellular clusters analyzed in the main text. This 63% increase can be understood as arising from a more homogeneous distribution of particles in the lattice, compared to confinement within a subset of cells. This result supports the significance of using NV magnetometry to visualize the sub-tissue and sub-cellular distribution of magnetic fields.

The final condition analyzed the effect of confining intracellular clusters in a lipid compartment (Supplementary Fig. 3.S7e). We simulated the effect of such a compartment by creating an impermeable 5 nm diffusion barrier surrounding the nanoparticle clusters. This decreased the relaxivity from 4.1 ± 0.20 $mM^{-1}s^{-1}$ to 3.8 ±0.16 $mM^{-1}s^{-1}$, within statistical error, indicating that the majority of the contrast from these large nanoparticle clusters does not come from water molecules in close proximity to the cluster surface.

Fluorescent Colocalization

To assess the accuracy of NV-based localization of magnetic particles in cells in the x-y plane, we performed vector magnetometry and fluorescent imaging on the same cellular specimens. To enable fluorescent visualization, the same nanoparticles used in the main text were labeled at their amino groups with Alexa 488 NHS (ThermoFisher Scientific). Before labeling, nanoparticles were diluted to 1 mg/ml in 0.1M sodium bicarbonate at pH=8.2. Alexa 488 dye was dissolved in DMSO at 10 mg/ml and added in 10 times molar excess to the nanoparticle surface amino groups. Fluorescent images were taken before the NV magnetometry commenced to avoid photobleaching due to NV illumination. We then performed a 2 hour vector magnetometry scan and localized the magnetic field sources using the algorithm depicted in Fig. 3.1f. Alexa 488 fluorescent signal was Wiener filtered to remove background speckle and then Gaussian blurred. Local maxima of the Gaussian blurred image were designated the centroids of the fluorescent signal. The average discordance between NV and fluorescent localization was 790 +/-105 nm. In one case we were unable to establish a fluorescent centroid corresponding to a dipole that was visible on the NV magnetometry scan. Fitting of this magnetic source predicted a magnetic moment corresponding to a single nanoparticle, which may explain its weak fluorescent signal.

Uniqueness of Fit for Dipole Magnetization and Height off the Diamond

Here, we seek to demonstrate that for a given (z,M) value pair, there does not exist another (z’,M’) value pair such that $\mathrm{B_x}(\mathrm{x}, \mathrm{y}, \mathrm{z}, \mathbf{M}) = \mathrm{B_x}(\mathrm{x}, \mathrm{y}, \mathrm{z'}, \mathbf{M'})$for all values of x and y. This can be proven by contradiction. The coordinate system is set such that the point dipole is at the origin and the measurement plane is below the point dipole and is parallel to the xy plane.

Assume there exists $(z, \boldsymbol{M})\ and\ (z', \boldsymbol{M'})\ such\ that\ \ B_x(x, y, z, \boldsymbol{M}) = B_x(x, y, z', \boldsymbol{M'})\ \forall\ (x, y)$

Let $(x, y) = (0, y_1)$ with $y_1 > 0$. From the equation for $B_x$provided in the main text,

$$\frac{\boldsymbol{M}\cdot\hat{x}}{r^3} = \frac{\boldsymbol{M\prime}\cdot\hat{x}}{r\prime^3} \tag{S5}$$

Where $r_1 = \sqrt{{y_1}^2 + z^2}\ and\ r_1' = \sqrt{{y_1}^2 + z'^2}$. Simplifying

$$\frac{M_x'}{M_x} = \frac{r_1'^3}{r_1^3} \tag{S6}$$

Now take $(x, y) = (0, y_2)$ with $y_2 > 0$. By similar logic:

$$\frac{M_x'}{M_x} = \frac{r_2'^3}{r_2^3} \tag{S7}$$

Where $r_2 = \sqrt{y_2^2 + z^2}\ and\ r_2' = \sqrt{y_2^2 + z'^2}$. Substituting from equation S6

$$\frac{r_2'^3}{r_2^3} = \frac{r_1'^3}{r_1^3} \tag{S8}$$

Plugging in the definitions and simplifying gives

$$\frac{y_1^2+z'^2}{y_1^2+z^2} = \frac{y_2^2+z'^2}{y_2^2+z^2} \tag{S9}$$

Cross-Multiplying and Simplifying gives

$$z^2(y_1^2 - y_2^2) = z'^2(y_1^2 - y_2^2) \tag{S10}$$

As the measurement plane is always below the magnetic source in our system, this implies either $z = z'or\ y_1 = y_2$, both of which violate assumptions in the proof. Thus, sampling any two points with y>0 along x=0 on the measurement plane uniquely specifies both **M** and z. (It is trivial to demonstrate that this also holds for any two points with y<0. The degeneracy from $y_1 = -y_2$ makes sense given the symmetric shape of the dipolar field.)

Due to SNR constraints and the need to localize the (x,y) position of the dipole source, we fit to many more than two points per dipole source.

3.6 Supplementary Figures

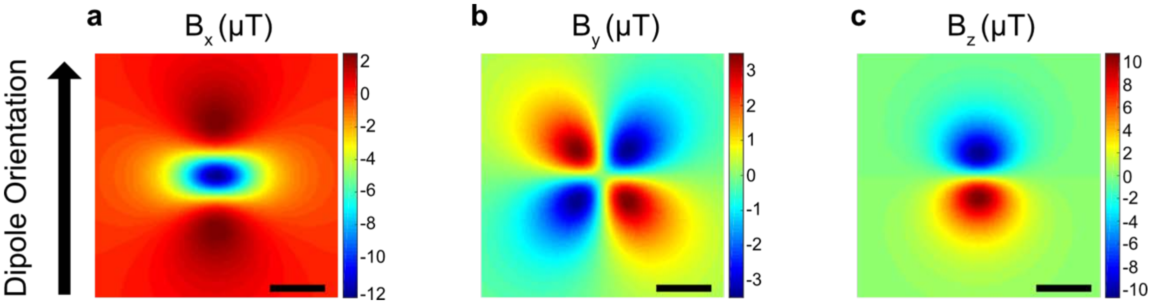

Supplementary Figure 3.S1 - Simulated dipole fields. Simulated B_x (**a**), B_y (**b**), and B_z (**c**) field projections for a point dipole oriented towards the top of the image with a magnetic moment of $10^{-15} A \cdot m^2$. The x and y coordinates of the dipole are fixed at the center of the image and the dipole is spaced two μm above the plane of projection. As in the main text, x is defined along the dipole axis, z is defined out of the page, and y is defined to complete the normal basis. Scale bars are 2.5 μm.

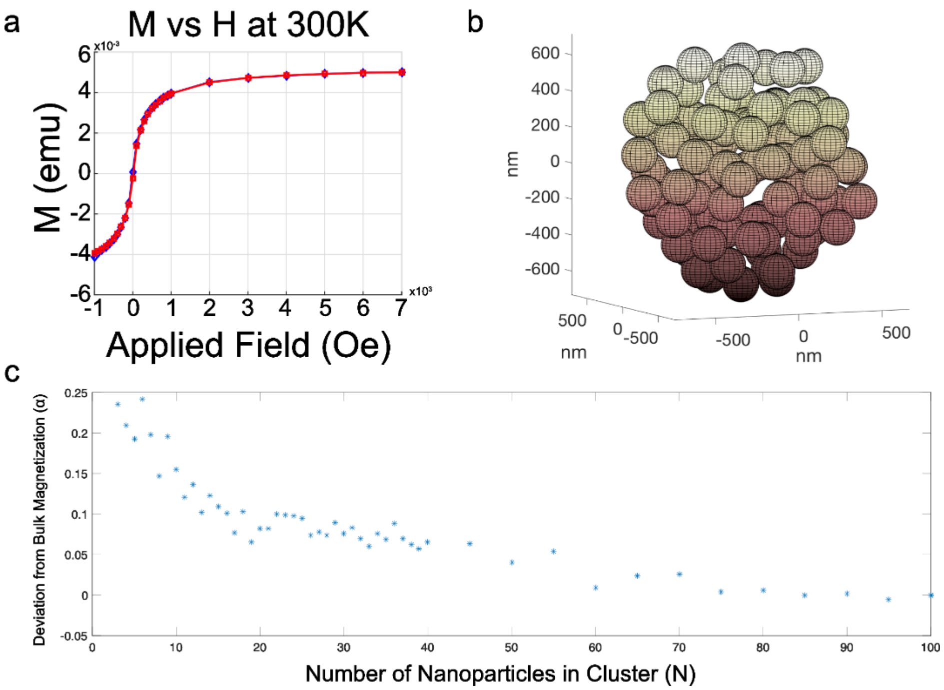

Supplementary Figure 3.S2 – SQUID magnetometry and saturation of IONs (a) SQUID magnetometry of a 100 µg stock of our IONs at 300K. **(b)** A representative pseudo-spherical cluster (N=100 nanoparticles) used in our Monte Carlo magnetization simulations. **(c)** Approximate error α of our bulk approximation for clusters containing varying numbers of nanoparticles. Each point represents the mean value from 60 random particle arrangements.

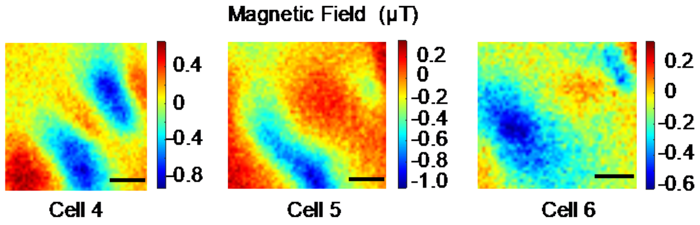

Supplementary Figure 3.S3 - Additional cells for Monte Carlo library. Vector magnetometry results from three additional cells. These cells were measured as described in Figure 1 with the exception that the imaging time was cut to 2 hours. Scale bars are 2.5 µm.

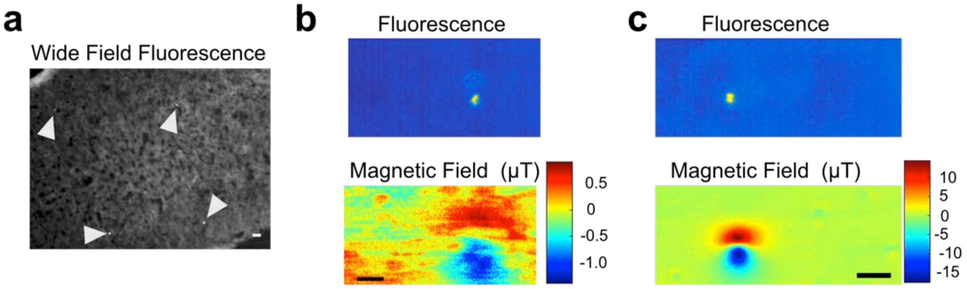

Supplementary Figure 3.S4 - Additional tissue sections. (**a**) Fluorescent image of a wide field of view of a representative liver tissue section from an iron-injected mouse. Punctate fluorescent spots from the fluorescently labeled 900 nm ION are sparsely visible in the fluorescent image. (**b-c**) Field profile of two additional clusters measured using our NV microscope, measured as in Figure 2. Scale bars are 20 μm.

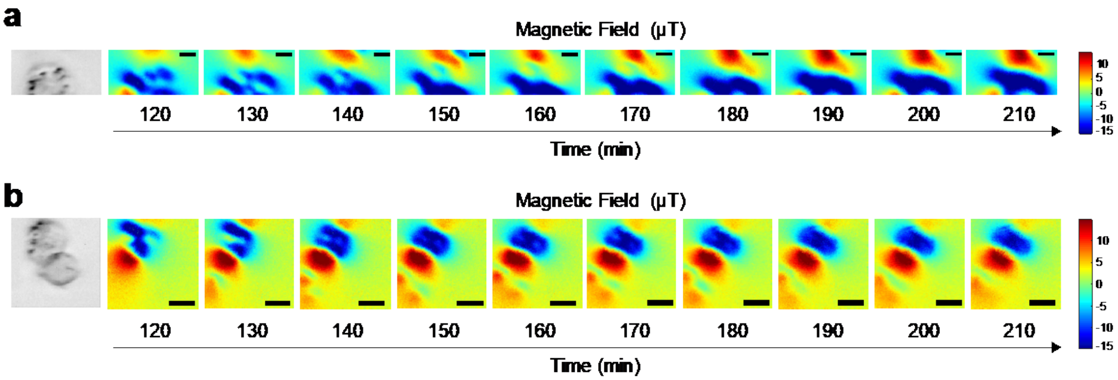

Supplementary Figure 3.S5 – Additional live cells. (**a-b**) Two additional live cell replicates matching Figure 3b. Cells were confirmed alive with trypan blue after NV imaging. Scale bars are 5 μm.

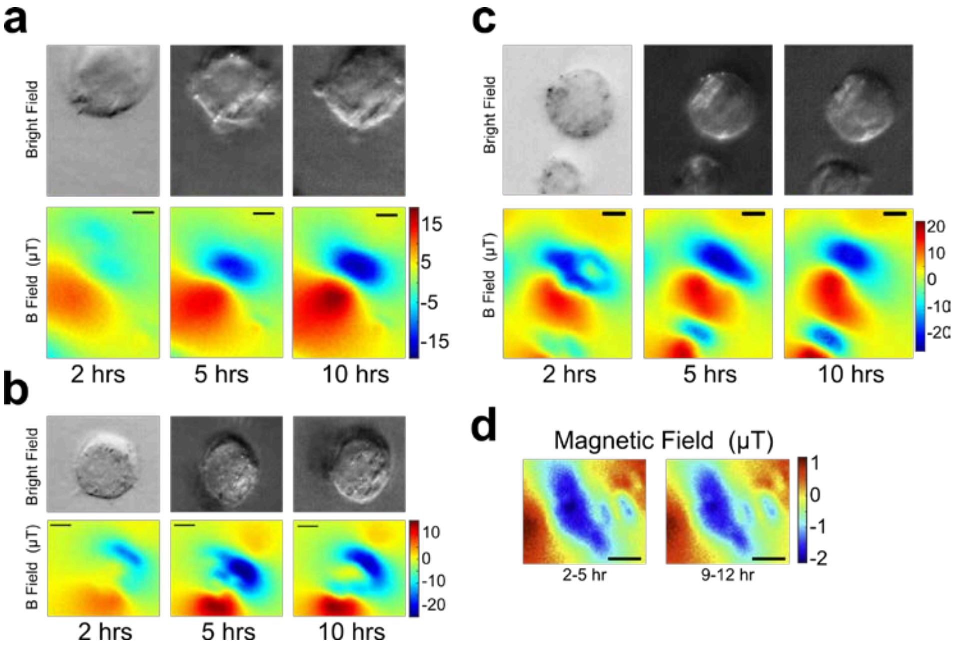

Supplementary Figure 3.S6 - Live cell imaging with extended time course. (**a-c**) Bright field and magnetic images of ION endocytosis in RAW cells acquired 2, 5, and 10 hours after initial nanoparticle exposure to 279 ng/ml 200 nm IONs. Trypan blue assay revealed an ~70% viability for these imaging studies. All displayed cells were still alive after imaging. Bright field illumination was provided by a hand-positioned LED source that was repositioned between images. (**d**) Magnetic field map from fixed cell acquired 7 hours apart to show the absence of dynamic changes in the magnetic field. Scale bars are 5 μm.

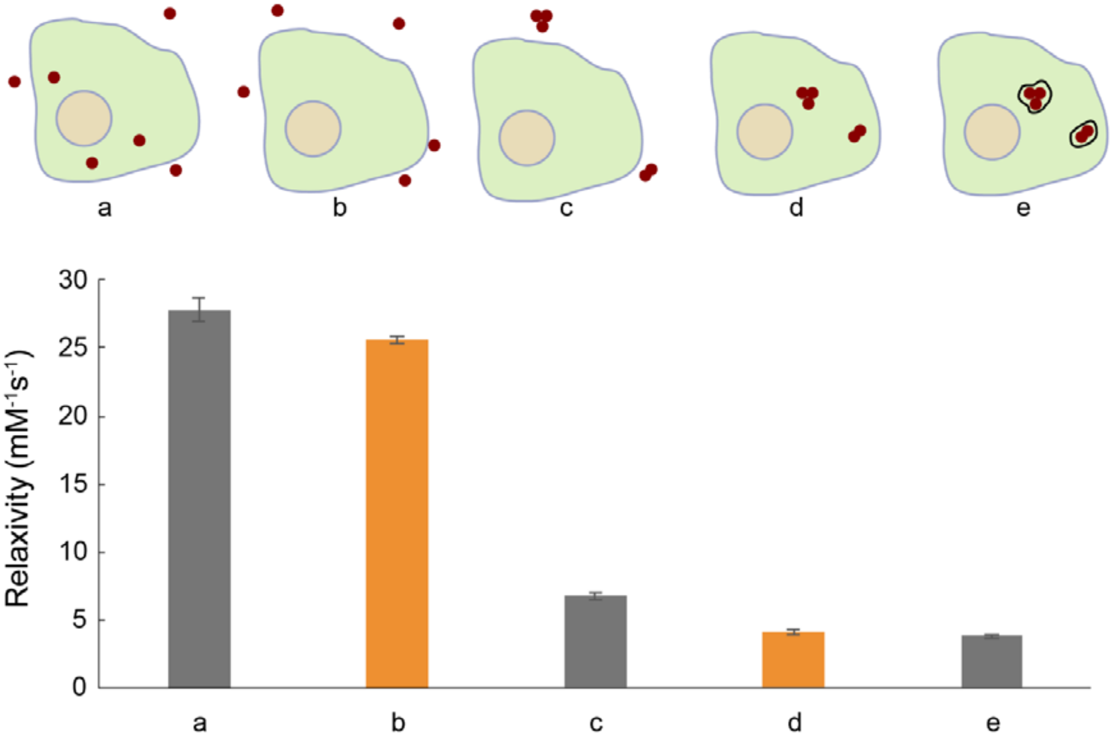

Supplementary Figure 3.S7 – Supplementary *in silico* models of T_2 relaxation. In order to further assess the predicted effect of spatial frequency and cellular confinement on nanoparticle relaxivity, we simulated several additional particle distribution scenarios using the same Monte Carlo algorithm described in the main text. The scenarios are illustrated on top, with corresponding T_2 relaxivities below. Orange bars correspond to data in the main text. **(a)** Diffuse (unclustered) nanoparticles were randomly placed throughout the lattice. As this geometry minimized clustering, it maximized relaxivity for our IONs. **(b)** Unclustered particles randomly placed in the extracellular space in the lattice. This is the same as the diffuse condition that was experimentally verified in Fig. 3.2 of the main text. As the particles are still unclustered, the partial refocusing effect is small, maintaining the high nanoparticle relaxivity **(c)** Clusters from NV-established cell library randomly dispersed throughout the extracellular space of the lattice. The clustering of the particles significantly reduces their relaxivity relative to the unclustered condition, but the large distances between the clusters significantly increase relaxivity compared to clusters spatially confined in "host" cells, as shown in (d). **(d)** Cells from the NV library were randomly placed in the lattice, and clustered nanoparticles were confined inside of their host cells. This is the same condition as the "clustered" case that was experimentally verified in Fig. 3.2 of the main text. **(e)** In order to determine the effect of confinement in an intracellular compartment, we added an impermeable 5 nm diffusion barrier around the clusters and randomly placed them inside their host cells as in condition (d). There was a statistically insignificant decrease in the nanoparticle relaxivity, supporting the hypothesis that the majority of the relaxivity of these particles comes from is outer-sphere effects on aqueous protons.

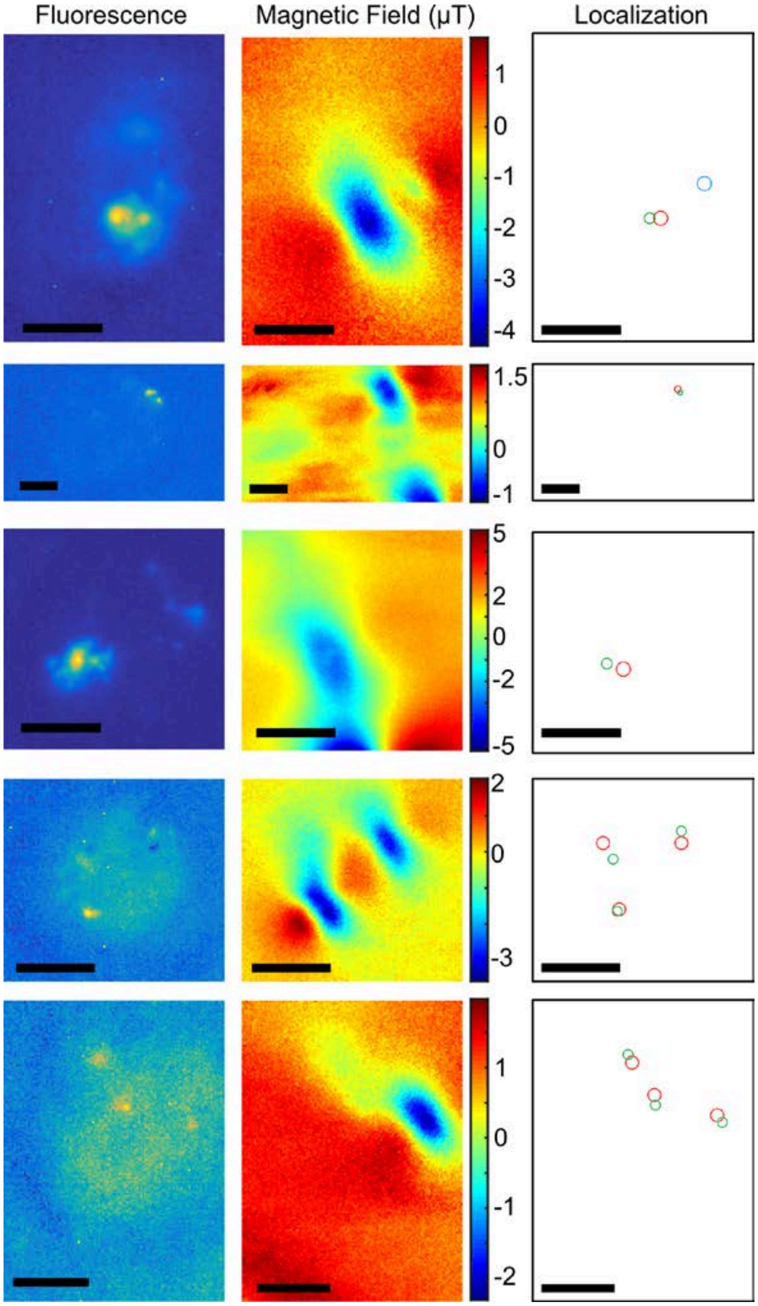

Supplementary Figure 3.S8 – Magnetic–fluorescent colocalization. Fluorescence and magnetic images of fixed cells after the uptake of 200 nm IONs labeled with Alexa 488 fluorescent dye. NV localization (red circles) show strong fidelity to centroids of fluorescent images (green circles) with a mean offset of <800nm. Circle diameters are fixed to the diffraction limit for the NV and Alexa 488 dye fluorescence respectively. The sole mismatch occurred in the top cell, where a second dipole was visible in the NV image and localization, but there was no corresponding centroid in the Alexa 488 fluorescent image. NV localization of this dipole is marked with blue. Fitting of this dipole revealed that it possessed the magnetic moment of ~1 nanoparticle, perhaps explaining the weak fluorescent signal. Scale bars are 5 μm.

Bibliography

1. Rouault, T. A. 2013. Iron metabolism in the CNS: implications for neurodegenerative diseases. Nat Rev Neurosci 14(8):551-564. Review.

2. Ghugre, N. R., and J. C. Wood. 2011. Relaxivity-iron calibration in hepatic iron overload: Probing underlying biophysical mechanisms using a Monte Carlo model. Magnetic resonance in medicine : official journal of the Society of Magnetic Resonance in Medicine / Society of Magnetic Resonance in Medicine 65(3):837-847.

3. Corot, C., P. Robert, J.-M. Idée, and M. Port. 2006. Recent advances in iron oxide nanocrystal technology for medical imaging. Advanced drug delivery reviews 58(14):1471-1504.

4. Weinstein, J. S., C. G. Varallyay, E. Dosa, S. Gahramanov, B. Hamilton, W. D. Rooney, L. L. Muldoon, and E. A. Neuwelt. 2010. Superparamagnetic iron oxide nanoparticles: diagnostic magnetic resonance imaging and potential therapeutic applications in neurooncology and central nervous system inflammatory pathologies, a review. Journal of Cerebral Blood Flow & Metabolism 30(1):15-35.

5. Kircher, M. F., S. S. Gambhir, and J. Grimm. 2011. Noninvasive cell-tracking methods. Nature reviews Clinical oncology 8(11):677-688.

6. Shapiro, E. M., K. Sharer, S. Skrtic, and A. P. Koretsky. 2006. In vivo detection of single cells by MRI. Magnetic Resonance in Medicine 55(2):242-249.

7. Vuong, Q. L., P. Gillis, and Y. Gossuin. 2011. Monte Carlo simulation and theory of proton NMR transverse relaxation induced by aggregation of magnetic particles used as MRI contrast agents. Journal of Magnetic Resonance 212(1):139-148.

8. Bowen, C. V., X. Zhang, G. Saab, P. J. Gareau, and B. K. Rutt. 2002. Application of the static dephasing regime theory to superparamagnetic iron-oxide loaded cells. Magnetic Resonance in Medicine 48(1):52-61.

9. Gossuin, Y., P. Gillis, A. Hocq, Q. L. Vuong, and A. Roch. 2009. Magnetic resonance relaxation properties of superparamagnetic particles. Wiley Interdisciplinary Reviews: Nanomedicine and Nanobiotechnology 1(3):299-310.

10. Matsumoto, Y., and A. Jasanoff. 2008. T₂ relaxation induced by clusters of superparamagnetic nanoparticles: Monte Carlo simulations. Magnetic Resonance Imaging 26(7):994-998.

11. Balasubramanian, G., I. Y. Chan, R. Kolesov, M. Al-Hmoud, J. Tisler, C. Shin, C. Kim, A. Wojcik, P. R. Hemmer, A. Krueger, T. Hanke, A. Leitenstorfer, R. Bratschitsch, F. Jelezko, and J. Wrachtrup. 2008. Nanoscale imaging magnetometry with diamond spins under ambient conditions. Nature 455(7213):648-651. 10.1038/nature07278.

12. Schirhagl R, C. K., Loretz M, Degen CL. . 2014. Nitrogen-Vacancy Centers in Diamond: Nanoscale Sensors for Physics and Biology. Annual Review of Physical Chemistry 65(1):83-105.

13. Le Sage, D., K. Arai, D. R. Glenn, S. J. DeVience, L. M. Pham, L. Rahn-Lee, M. D. Lukin, A. Yacoby, A. Komeili, and R. L. Walsworth. 2013. Optical magnetic imaging of living cells. Nature 496(7446):486-489.

14. Glenn, D. R., K. Lee, H. Park, R. Weissleder, A. Yacoby, M. D. Lukin, H. Lee, R. L. Walsworth, and C. B. Connolly. 2015. Single-cell magnetic imaging using a quantum diamond microscope. Nat Meth 12(8):736-738. Brief Communication.

15. Steinert, S., F. Ziem, L. T. Hall, A. Zappe, M. Schweikert, N. Götz, A. Aird, G. Balasubramanian, L. Hollenberg, and J. Wrachtrup. 2013. Magnetic spin imaging under ambient conditions with sub-cellular resolution. 4:1607. Article.

16. J. F. Barry, M. J. T., J. M. Schloss, D. R. Glenn, Y. Song, M. D. Lukin, H. Park, R. L. Walsworth. 2016. Optical magnetic detection of single neuron action potentials using quantum defects in diamond. arXiv:1602.01056.

17. Tetienne, J. P., L. Rondin, P. Spinicelli, M. Chipaux, T. Debuisschert, J. F. Roch, and V. Jacques. 2012. Magnetic-field-dependent photodynamics of single NV defects in diamond: an application to qualitative all-optical magnetic imaging. New Journal of Physics 14(10):103033.

18. Daldrup-Link, H. E., D. Golovko, B. Ruffell, D. G. DeNardo, R. Castaneda, C. Ansari, J. Rao, G. A. Tikhomirov, M. F. Wendland, and C. Corot. 2011. MRI of tumor-associated macrophages with clinically applicable iron oxide nanoparticles. Clinical Cancer Research 17(17):5695-5704.

19. Zanganeh, S., G. Hutter, R. Spitler, O. Lenkov, M. Mahmoudi, A. Shaw, J. S. Pajarinen, H. Nejadnik, S. Goodman, M. Moseley, L. M. Coussens, and H. E. Daldrup-Link. 2016. Iron oxide nanoparticles inhibit tumour growth by inducing pro-inflammatory macrophage polarization in tumour tissues. Nat Nano advance online publication. Article.

20. Corot, C., K. G. Petry, R. Trivedi, A. Saleh, C. Jonkmanns, J.-F. Le Bas, E. Blezer, M. Rausch, B. Brochet, and P. Foster-Gareau. 2004. Macrophage imaging in central nervous system and in carotid atherosclerotic plaque using ultrasmall superparamagnetic iron oxide in magnetic resonance imaging. Investigative radiology 39(10):619-625.

21. Tarulli, E., J. D. Chaudhuri, V. Gretka, A. Hoyles, C. M. Morshead, and G. J. Stanisz. 2013. Effectiveness of micron-sized superparamagnetic iron oxide particles as markers for detection of migration of bone marrow-derived mesenchymal stromal cells in a stroke model. Journal of Magnetic Resonance Imaging 37:1409-1418.

22. Shapiro, E. M., S. Skrtic, K. Sharer, J. M. Hill, C. E. Dunbar, and A. P. Koretsky. 2004. MRI detection of single particles for cellular imaging. Proceedings of the National Academy of Sciences of the United States of America 101:10901-10906.

23. McAteer, M. A., N. R. Sibson, C. von zur Muhlen, J. E. Schneider, A. S. Lowe, N. Warrick, K. M. Channon, D. C. Anthony, and R. P. Choudhury. 2007. In vivo magnetic resonance imaging of acute brain inflammation using microparticles of iron oxide. Nature Medicine 13:1253-1258.

24. Perez, J. M., L. Josephson, T. O'Loughlin, D. Hogemann, and R. Weissleder. 2002. Magnetic relaxation switches capable of sensing molecular interactions. Nat Biotech 20(8):816-820. 10.1038/nbt720.

25. Atanasijevic, T., M. Shusteff, P. Fam, and A. Jasanoff. 2006. Calcium-sensitive MRI contrast agents based on superparamagnetic iron oxide nanoparticles and calmodulin. Proceedings of the National Academy of Sciences of the United States of America 103(40):14707-14712.

26. Kirtley, J. R., and J. P. Wikswo Jr. 1999. Scanning SQUID microscopy. Annual Review of Materials Science 29(1):117-148.

27. Finkler, A., Y. Segev, Y. Myasoedov, M. L. Rappaport, L. Ne’eman, D. Vasyukov, E. Zeldov, M. E. Huber, J. Martin, and A. Yacoby. 2010. Self-aligned nanoscale SQUID on a tip. Nano letters 10(3):1046-1049.

28. Hartmann, U. 1999. Magnetic force microscopy. Annual review of materials science 29(1):53-87.

29. Sidles, J. A., J. L. Garbini, K. Bruland, D. Rugar, O. Züger, S. Hoen, and C. Yannoni. 1995. Magnetic resonance force microscopy. Reviews of Modern Physics 67(1):249.

30. Maclaurin, D., L. T. Hall, A. M. Martin, and L. C. L. Hollenberg. 2013. Nanoscale magnetometry through quantum control of nitrogen–vacancy centres in rotationally diffusing nanodiamonds. New Journal of Physics 15:013041.

31. Kucsko, G., P. C. Maurer, N. Y. Yao, M. Kubo, H. J. Noh, P. K. Lo, H. Park, and M. D. Lukin. 2013. Nanometre-scale thermometry in a living cell. Nature 500(7460):54-58. Letter.

32. RugarD, H. J. Mamin, M. H. Sherwood, KimM, C. T. Rettner, OhnoK, and D. D. Awschalom. 2015. Proton magnetic resonance imaging using a nitrogen–vacancy spin sensor. Nat Nano 10(2):120-124. Letter.

33. Wäldchen S, L. J., Klein T, van de Linde S, Sauer M. . 2015. Light-induced cell damage in live-cell super-resolution microscopy. Scientific Reports(5).

34. Mosher, J. C., P. S. Lewis, and R. M. Leahy. 1992. Multiple dipole modeling and localization from spatio-temporal MEG data. IEEE Transactions on Biomedical Engineering 39(6):541-557.

35. Mukherjee, A., D. Wu, H. C. Davis, and M. G. Shapiro. 2016. Non-invasive imaging using reporter genes altering cellular water permeability. Nature Communications 7:13891. Article.

36. Szafer, A., J. Zhong, and J. C. Gore. 1995. Theoretical Model for Water Diffusion in Tissues. Magnetic Resonance in Medicine 33(5):697-712.

37. Imae, T., H. Shinohara, M. Sekino, S. Ueno, H. Ohsaki, K. Mima, and K. Ohtomo. 2009. Estimation of Cell Membrane Permeability and Intracellular Diffusion Coefficient of Human Gray Matter. Magnetic Resonance in Medical Sciences 8(1):1-7.

38. Hevia, D., A. Rodriguez-Garcia, M. Alonso-Gervós, I. Quirós-González, H. M. Cimadevilla, C. Gómez-Cordovés, R. M. Sainz, and J. C. Mayo. 2011. Cell volume and geometric parameters determination in living cells using confocal microscopy and 3D reconstruction.

39. Loike, J. D., L. Cao, K. Kuang, J. C. Vera, S. C. Silverstein, and J. Fischbarg. 1993. Role of facilitative glucose transporters in diffusional water permeability through J774 cells. The Journal of General Physiology 102(5):897-906.

40. Pfeuffer, J., U. Flögel, W. Dreher, and D. Leibfritz. 1998. Restricted diffusion and exchange of intracellular water: theoretical modelling and diffusion time dependence of 1H NMR measurements on perfused glial cells. NMR in Biomedicine 11(1):19-31.

41. Holz, M., S. R. Heil, and A. Sacco. 2000. Temperature-dependent self-diffusion coefficients of water and six selected molecular liquids for calibration in accurate 1H NMR PFG measurements. Physical Chemistry Chemical Physics 2(20):4740-4742. 10.1039/B005319H.

42. Wilhelm, C., A. Cebers, J. C. Bacri, and F. Gazeau. 2003. Deformation of intracellular endosomes under a magnetic field. Eur Biophys J 32(7):655-660.

43. Aubertin, K., S. Bonneau, A. K. Silva, J. C. Bacri, F. Gallet, and C. Wilhelm. 2013. Impact of photosensitizers activation on intracellular trafficking and viscosity. PLoS One 8(12):e84850.

44. Huang, W., Liang, Y. 2012. Serial Symmetrical Relocation Algorithm for the Equal Sphere Packing Problem. arXiv:1202.4149.

45. Thorek, D. L. J., and A. Tsourkas. 2008. Size, Charge and Concentration Dependent Uptake of Iron Oxide Particles by Non-Phagocytic Cells. Biomaterials 29(26):3583-3590.

46. Sanchez, F. H. e. a. 2015. Dipolar interaction and demagnetizing effects in magnetic nanoparticle dispersions: introducing the Mean Field Interacting Superparamagnet Model (MFISP Model). arXiv:1507.05192.

47. Varón, M., M. Beleggia, T. Kasama, R. J. Harrison, R. E. Dunin-Borkowski, V. F. Puntes, and C. Frandsen. 2013. Dipolar Magnetism in Ordered and Disordered Low-Dimensional Nanoparticle Assemblies. Scientific Reports 3:1234. Article

Chapter 4

NANOSCALE FLUORESCENT THERMOMETRY OF MAGNETIC NANOPARTICLES AND FERRITIN IN AN ALTERNATING MAGNETIC FIELD

Davis, H.C., Kang, S., Lee, J., Shin, T.,Putterman, H.,Cheon, J.W.,Shapiro,M.G, (2019). "Nanoscale fluorescent thermometry of magnetic nanoparticles and ferritin in an alternating magnetic field" *In preparation.*

4.1 Introduction

Radiofrequency heating of superparamagnetic iron oxide nanoparticles (SPIONs) is an established technique for the ablative treatment of diseases such as cancer and an emerging tool in basic biological research. In a typical application of this method, radiofrequency alternating magnetic fields (RF-AMF) are used to remotely heat a bolus of injected SPIONs in a tissue, raising the local temperature to a critical level to kill diseased cells or increase their sensitivity to chemotherapy or radiotherapy [1]. As single-domain magnets, SPIONs can generate heat in response to RF-AMF stimulation via dissipative losses associated with rigid body rotation (Brownian relaxation) or internal magnetic realignment (Neel relaxation) [2-5]. Significant theoretical [6, 7] and computational [8, 9] work has been done to model the interplay of these relaxation mechanisms and their contribution to the heat generated by the particle. In an effort to use magnetic fields to control, rather than kill, specific cells, recent work has combined nanoparticle-based radiofrequency hyperthermia in the well-tolerated temperature range of 37–42 ºC with the targeted expression of temperature-sensitive biomolecules such as the temperature-gated ion channel TRPV1 [10]. This "magnetogenetic" approach enables

RF-AMF to turn on calcium currents in cells, leading to activation of insulin secretion or neural circuit activity [11, 12].

A key requirement for effective magnetogenetic manipulation is for the heat generated by SPIONs to be localized to the target cells and not appreciably affect surrounding tissue. However, the extent of this thermal confinement is matter of considerable debate. It is widely accepted that a small bolus of particles generates a millimeter-scale heat diffusion zone during RF-AMF, affecting cells within this region and not outside it. In addition, several studies have suggested that heat is preferentially confined to the nanoscale vicinity of individual magnetic nanoparticles during RF-AMF stimulation, resulting in a large steady-state temperature gradient at the surface of the nanoparticle [10, 13-15]. Such nanoscale confinement would enable the actuation of thermal bioswitches attached to a SPION without significantly heating the rest of the cell. Further extending this concept, it has been proposed that genetically encoded magnetic nanoparticles such as ferritin, which produce insignificant bulk heating in response to RF-AMF due to their small magnetic coercivity, could nevertheless activate temperature-sensitive ion channels to which they are tethered due to the heat-concentrating effect of thermal confinement [11, 16].

While millimeter-scale heat diffusion profiles are uncontroversial, the concept of nanoscale heat confinement near the surface of nanoparticles in aqueous suspension represents a significant departure from well-established heat transport theory [17]. In a classical analysis, the steady-state temperature profile emanating from a spherical source can be predicted by Fourier's heat diffusion law [18]:

$$\Delta T(r) = \frac{Q}{4\pi c r}$$

Here Q is the heating power of the source, c is the thermal conductivity of the medium (0.64 W $m^{-1}K^{-1}$ for water), r is the distance from the center of the source, and ΔT is the predicted temperature above an infinitely far location in the bath. This continuum analysis is consistent with experimental and computational studies of heat transport from laser-heated gold nanoparticles in fluid, whose ability to generate over 100 nW of heat per particle results in a measurable temperature difference between the nanoscale vicinity of the particle surface and the bulk fluid bath [18-21]. However, when applied to SPIONS, which typically generate less than 30 fW of heat per particle under RF-AMF [22], Fourier's law predicts a negligible temperature difference between the vicinity of a single particle and the bulk fluid (373 nK for Q=30 fW and r=10 nm in water). Thus, although the concerted action of many SPIONS in a ferrofluid effectively heats the bulk fluid, Fourier theory does not predict a measurable temperature gradient emanating from the surface of individual particles. When this analysis is extended to account for a finite thermal interface resistance at the particle surface, it also predicts a temperature discontinuity between the solid particle and the fluid, which is measurable for laser-heater gold nanoparticles [23]. However, this effect would again have an exceedingly small magnitude for a 30 fW source, assuming an interface resistance in the range of previously characterized nanoparticles [20, 23].

Contradicting these predictions of Fourier's law, several studies using optical thermometry at the surface of magnetic nanoparticles in RF-AMF have reported local heating of several K relative to the bulk [10, 13-15]. This literature is cited in magnetogenetics studies as a way to motivate and explain the biological results observed [11, 16]. However, given the direct conflict between these results and classical theory, and the controversial reception of several recent works on magnetogenetics [17], a careful re-examination of the possibility of non-classical heat confinement at the surface of SPIONs and ferritin, and the potential artifacts confounding previous studies, is greatly needed.

To address this need, we designed an experimental approach allowing us to measure the temperature at the surface of magnetic nanomaterials and in surrounding fluid during RF-AMF application using a simultaneous all-optical readout with 0.1 ºC sensitivity (**Fig. 4.1a**). Measurements of three different types of SPIONs representing a range of sizes, core compositions and surface chemistries revealed no measurable difference in temperature between the particle surface and the bulk solution during RF-AMF heating, while ferritin failed to show any heat generation. These results suggest that nanomagnetic hyperthermia follows classical heat transfer theory. Additional experiments recapitulating previous measurement approaches revealed potential sources of artifacts that could be misinterpreted as non-classical thermal confinement.

4.2 Materials and Methods

4.2.1 Probe Conjugation and Sample Preparation for Commercial particles

In order to precisely measure the temperature of the surface of our magnetite nanoparticle samples (Ocean Nanotech SHA-10 and SHA-20), we conjugated NHS-Dylight 550 (Thermo Scientific) to the amine groups on magnetite nanoparticle surface in PBS buffer (Corning) with a particle concentration of 1 mg/ml and a 10 fold excess of Dylight 550 to amine groups on the particle surface. The reaction was allowed to proceed under mechanical agitation at room temperature for 10 hours. Next, the sample was dialyzed overnight against a 4000-fold volume excess of 10 mM Tris HCL (pH 8) in order to hydrolyze any unreacted NHS groups and separate the unbound dye from the nanoparticle solution. The sample was then dialyzed overnight against a 4000-fold volume excess of PBS and concentrated to the desired final solution using 10 kDa centrifugal filters (Amicon). Our fluid temperature probe, DY-521XL (Dyomics), was mixed into the ferrofluid solution at a sufficient concentration to balance the fluorescent intensities of the two dyes. Horse spleen ferritin went through the identical preparation, with the exception that the dye-excess was 100 dye molecules per ferritin. Magnetite nanoparticle and ferritin iron concentrations were quantified using a total iron quantification kit (Pointe Scientific I7505) after digesting samples at 75°C in nitric acid for 4 hours. Ferritin protein concentration was quantified using a BCA protein assay (ThermoFisher 23225).

4.2.2 Core-Shell Nanoparticle Synthesis and Characterization

Core cobalt ferrite nanoparticles were synthesized by the thermal decomposition method. Cobalt(II) chloride (3.25 mmol), iron(III) acetylacetonate (5.00 mmol), oleylamine (91.2 mmol), oleic acid (31.6 mmol), and octyl ether (49.9 mmol) were mixed into a three-neck round-bottom flask under an Ar atmosphere. The reaction mixture was heated up to 300 ^{o}C. After 1 hour, the resulting cobalt ferrite nanoparticles were isolated by centrifugation and washed with hexane and ethanol.

Core-shell nanoparticles composed of a cobalt ferrite core and a manganese ferrite shell were then synthesized by the seed-mediated growth method. Cobalt ferrite nanoparticles (0.34 mmol), manganese(II) chloride (3.25 mmol), iron(III) acetylacetonate (5.00 mmol), oleylamine (60.8 mmol), oleic acid (15.8 mmol), and trioctylamine (34.3 mmol) were added to a three-neck round bottom flask under an Ar atmosphere. The reaction mixture was heated to 350 ^{o}C and maintained for 1 hour. The core-shell nanoparticle was obtained by centrifugation and washing processes. (See **Supplementary Fig. 4.S5** for particle characterization.)

As-synthesized core-shell nanoparticles were coated with a silica shell and conjugated with Dylight 550 using a previously reported method with minor modifications [24]. Amine functionalized core-shell nanoparticles were conjugated with NHS-Dylight 550 in DMSO with a particle concentration of 1 mg/ml and Dylight 550 concentration of 0.1 mg/ml. The reaction was allowed to proceed in microtube mixer (Eppendorf) at 1,500 r.p.m. for 8 hours at room temperature. The products were purified on a MACS MS column (Milttenyi Biotec.) and eluted with DMSO. The sample was then reacted with 1 mg of succinic anhydride per 1 mg/ml of particle solution for an additional 8 hours at room temperature in vigorous shaking. The products were purified again on a MACS MS column and eluted with pure water. To make sure that there is no remaining free Dylight 550, the products were purified using dye removal columns (ThermoFisher 22858) three times. In each step, concentration of the core-shell nanoparticle was measured using a UV-visible absorption spectrophotometer (extinction coefficient: 15.2 ml/mg·$\text{cm}_{(\text{Fe+Co+Mn})}$ at 400 nm).

4.2.3 Fluorometry

We used a custom-built fiberoptic fluorometer to probe the fluorescent intensity of our optical thermometers. Excitatory light was provided by an OBIS 532-LS laser modulated with an 80 kHz sinusoidal signal. The laser light traveled through the outer ring of an optical fiber bundle whose end was housed in a custom PEEK fiber ferrule (Ocean Optics) which was mechanically coupled to our plastic sample holder. Fluorescence from both dyes was collected via the central core in the fiber bundle. The collected fluorescence was coupled to air via a 10 mm .22 NA Fiber Optic Collimator (Edmund Optics 88-180) and notch filtered to eliminate the signal from the 532 nm laser. The result light was split using a long-pass dichroic mirror. The reflected leg was short-pass filtered at 600 nm, and the transmitted leg was long-pass filtered at 650 nm. All filters and mirrors were from Thorlabs. The signal from each dye was focused onto a silicon photodiode (Thorlabs DET36A). Photodiode signals were amplified by lock-in amplifiers locked to the laser modulation frequency with 300 ms integration time. Resulting signals were digitized in a Molecular Devices Axon Digidata 1550 and processed using Matlab.

4.2.4 Electromagnet Construction and Characterization

We designed three distinct electromagnets for our study corresponding to three frequency ranges: 400-648 kHz, 1-5 MHz, and 30-40 MHz. Our 400-648 kHz electromagnet produced a strong magnetic field in a 10 mm gap in a water-cooled Ferroxcube 3F3 toroid wound with litz wire. The toroid was placed in series with a high voltage mica capacitor (1-5 nF depending on desired resonance) forming a series RLC circuit. In order to impedance match this circuit with a 50 ohm standard, we constructed a toroidal transformer out of a Ferroxcube 3F3 toroid and placed a variable ballast resistor (40-47 ohms) on the 50 ohm side of the transformer. AC signals were generated by a Stanford Research Systems SG380 signal generator and amplified by an Electronics and Innovation 1020L RF amplifier. Our 1-5 MHz system used the same signal generator and amplifier to drive a toroidal electromagnet with better high-frequency performance, but a lower saturation magnetization (Fair-Rite Ferrite

52) which was balanced by a single vacuum variable capacitor. Our 30-40 MHz electromagnet used 3 vacuum variable capacitors to tune and impedance match an air-cored solenoid to a 50 ohm high frequency amplifier (MiniCircuits ZHL-3A-S+). The air-cored solenoid had a gap in the windings to insert our sample holder. All field strengths were measured using a custom-built magnetic search loop attached to a 100 MHz digital oscilloscope. Stimulus timing was controlled with Labview.

4.2.5 Sample Calibration Chamber

Our custom-built temperature-controlled cuvette holder was composed of a copper block with a gap machined in the front to hold an optical glass cuvette (Fireflysci Type 507) and a fan-cooled thermoelectric plate on the back. The temperature of the fluid was monitored using an immersed fiberoptic phosphor temperature probe (Osensa PRB-G20). Using a PID control system, the copper block temperature was stepped three times between a randomly permuted list of 5 temperatures. A five-minute settling time was allowed in between temperature changes. The fluorescence of both dyes was evaluated for thirty seconds after the settling time using the system described in the fluorometry section above.

4.3 Results

Our temperature measurements made use of two spectrally separable, strongly thermochromic organic dyes to independently measure the temperature on the nanoparticle surface and in the surrounding bath (**Fig. 4.1a**). The surface probe, Dylight 550 NHS, was conjugated to the surface of nanoparticles via amine cross-linking, while the fluid probe, DY-521XL, was dissolved freely in the solution. The two dyes were excited at the same time by a modulated 532 nm laser via the outer ring of an optical fiber bundle, and the resulting fluorescent signal was collected via a separate core of the same fiber bundle. The emitted light was split using a series of dichroic filters and mirrors to isolate the signal from the two fluorescent dyes, which was transduced to voltage by silicon photodiodes connected to analog lock-in amplifiers (**Fig. 4.1b**). The dyes were readily spectrally separated due to the large Stokes shift of DY-521XL, with channel crosstalk below 6% (**Fig. 4.1c and Supplementary Fig. 4.S1**). Extra care was taken to minimize free Dylight 550 in the solution and ascertain that the vast majority of the fluorescence measured for this dye was coming from the nanoparticle surface (**Supplementary Table S1**).

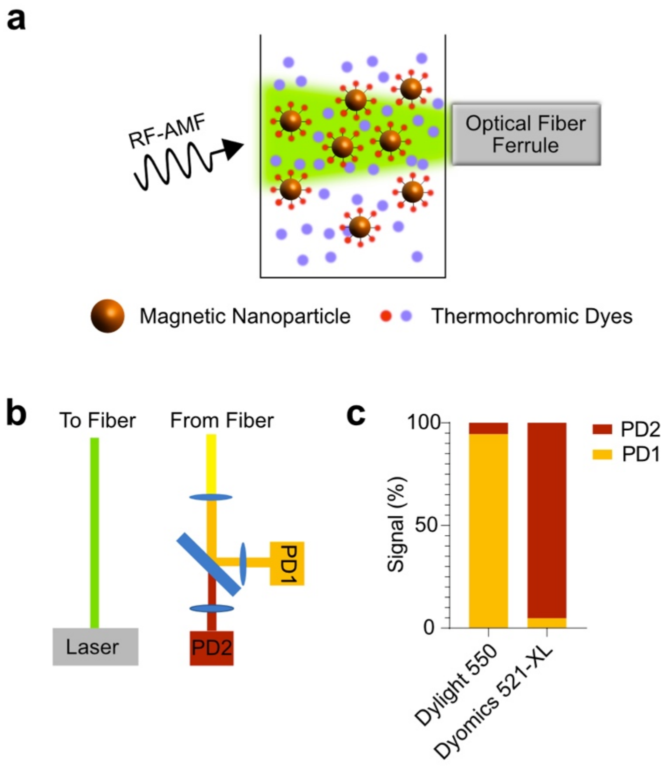

Figure 4.1 Nanoscale thermometry during magnetic nanoparticle hyperthermia. a Diagram of experimental setup, involving the simultaneous optical measurement of the temperature of the nanoparticle surface and surrounding fluid during radiofrequency alternating magnetic field (RF-AMF) application using thermochromic dyes as nanoscale temperature probes. **b** Diagram of optical path, in which both dyes are excited using a modulated 532 nm laser, and the emitted fluorescent signal is spectrally separated to independently evaluate the fluorescence of each dye on a silicon

photodiode. The photodiode voltage is demodulated and amplified using an analog lock-in amplifier. **c** Independently measuring the fluorescence of unmixed Dylight 550-labeled nanoparticles and DY-521XL shows that our system can discriminate between these dyes with less than 6% crosstalk. (See **Supplementary Fig. 4.S1** for the spectra of Dylight 550-labeled nanoparticles and DY-521XL.)

Before applying RF-AMF, we calibrated the thermochromic response of each individual dye-labeled ferrofluid sample by measuring the fluorescence intensity of both dyes while varying the temperature using a custom-built temperature-controlled cuvette holder (**Fig. 4.2a**). The sample was cycled three times between a randomly permuted list of five temperatures. Bulk fluid temperature was monitored during this calibration procedure using a 450-µm diameter phosphor thermal probe. Both fluorophores showed a strong linear decrease in fluorescence over the experimental temperature range (**Fig. 4.2, b-c**).

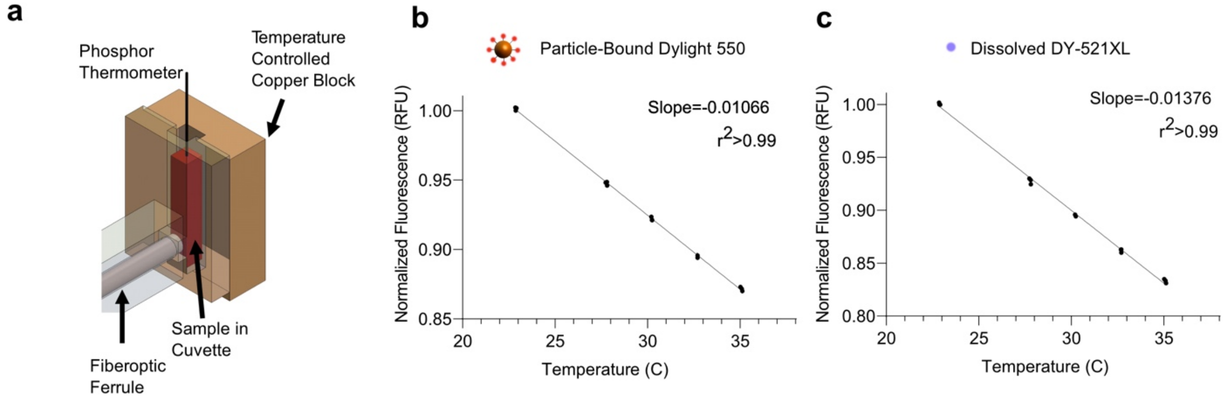

Figure 4.2 Thermochromic calibration of particle-bound and free dye. a Diagram of calibration setup. For each individual ferrofluid sample, a calibration was obtained by monitoring the change in fluorescence intensity of each dye in response to temperature cycling in a custom temperature-controlled cuvette holder. **b** Representative calibration curves from a ferrofluid containing Dylight 550-labeled 10 nm iron oxide nanoparticles and free DY-521XL solution. Fluorescence at five temperatures were measured three times in a randomly permuted sweep. Points represent the average of each measurement. Error bars represent ± SEM, and are not shown if smaller than the plotted symbols.

Our study of synthetic nanoparticle RF-AMF heating used three distinct magnetic nanoparticle compositions (**Fig. 4.3a**). First, we examined commercially available 10-nm magnetite nanoparticles, which are similar to a variety of small superparamagnetic iron oxide ferrofluids commonly used for magnetic resonance imaging and similar in core size to ferritin. Second, we measured the responses of commercial 20-nm iron oxide nanoparticles, a core size commonly used in radiofrequency hyperthermia owing to its significant specific loss power [22, 25]. According to the manufacturer, both of these particle types are coated with a 4 nm-thick organic shell comprising a monolayer of oleic acid and a monolayer of amphiphilic polymer. Third, we examined the heating behavior of a ferrofluid containing custom-synthesized 15-nm core-shell nanoparticles (**Supplementary Fig. 4.S5**), which have exceptional coercivity and heating ability. These nanoparticles were coated with a 3 nm-thick silica layer. All particles had surface amine groups enabling dye conjugation.

After calibration, we measured the fluorescence of particle-bound and free dye in response to strong RF-AMF produced by a water-cooled gapped ferrite toroid wound with litz wire (**Fig. 4.3b**). This allowed us to apply fields of up to 27 kA/m at frequencies of 420 to 648 kHz, within the range of common parameters in literature. Samples in shortened 5-mm silica tubes were placed inside a sample housing jacketed by constant airflow to minimize heat transfer from the toroid. We applied RF-AMF stimulation for 20 one-minute cycles with 9 minutes of rest between cycles to allow the toroid to cool. Samples were tested at different concentrations to ensure sufficient heating of small magnetite particles, while minimizing particle clustering for larger and more magnetic particles. We performed three trials for each sample with separate nanoparticle batches, and representative results for each particle type are shown in **Fig. 4.3, c-e** (additional trials shown in **Supplementary Fig. 4.S2**). All three nanoparticle compositions generated significant heat due to RF-AMF. However, in each case, we observed no measurable difference between the temperature of the bulk fluid and the temperature of the nanoparticle surface throughout the experimental time course. This was true for all three particle types despite their different core sizes, shell materials and thickness and concentration in the fluid. These results suggest that heat transfer from SPIONs follows classical theory.

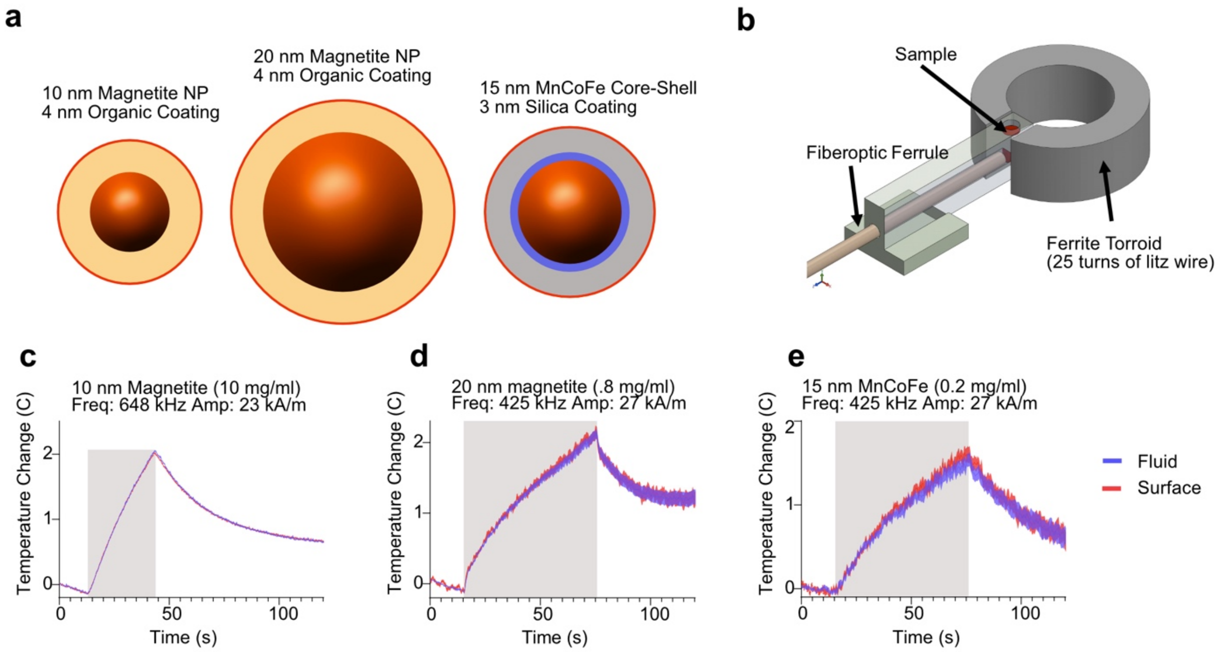

Figure 4.3 Nanoscale thermometry of synthetic nanoparticles a Diagram of the structure of three nanoparticle types tested with RF-AMF heating. **b** Diagram of hyperthermia apparatus, which generates a concentrated magnetic field in a gapped toroid wound with litz wire, acting as the inductor in a series-resonant RLC circuit. The fluorescence is measured with a fiberoptic fluorometer with lock-in amplification. **c-e** Surface and fluid temperatures measured for each nanoparticle type during RF-AMF application. Mean and SEM temperature for particle surface (red) and surrounding fluid (blue) are plotted for each sample, with frequency and field parameters specified above the plot. RF-AMF application period is denoted by grey shading. Each trace denotes the mean ± S.E.M. of 20 runs of RF-AMF stimulation. Cooling seen before RF-AMF stimulus results from cooling of the toroid between stimuli. (See **Supplementary Fig. 4.S3**.)

Having examined the possibility of nanoscale heat confinement at the surface of synthetic magnetic nanoparticles, we used the same nanoscale thermometry technique to investigate the heating ability of the metalloprotein ferritin. Ferritin comprises a 2 nm-thick protein shell enclosing an 8 nm antiferromagnetic ferrihydrite core (**Fig. 4.4a**) [26]. A disordered surface layer of the core gives rise to uncompensated magnetic spins, resulting in a small magnetic moment. Since these uncompensated spins are only weakly coupled, the Neel relaxation rate of the ferritin core is in the GHz range [27, 28], suggesting that this protein is not expected to experience dynamic hysteresis under RF-AMF at kHz and MHz frequencies. This has been confirmed by previous thermometry of bulk ferritin ferrofluids [29]. Nevertheless, multiple studies have proposed ferritin heating under RF-AMF as a mechanism of thermal actuation in engineered cellular signaling pathways [11, 16] by invoking the possibility of surface thermal confinement, unmeasurable by bulk techniques. To investigate the possibility of heat confinement on the ferritin surface under RF-AMF stimulation, we conjugated Dylight 550-NHS to the surface amines of horse spleen ferritin, a widely studied model ferritin containing an average of 2600 iron atoms per core. We mixed the resulting ferrofluid with DY-521XL and calibrated the thermochromic response of both dyes as we did for synthetic nanoparticles. We then applied RF-AMF at three different frequencies spanning 425 kHz to 35.6 MHz, covering the field parameters used in previous reports of magnetogenetic control [10, 11, 16]. At no frequency were we able to measure heating of the ferritin-containing solution, nor did we observe heat buildup on the protein surface (**Fig. 4.4, b-d**). Small background heating from the 425 kHz toroid, measured using a blank sample containing only DY 521-XL in PBS, was subtracted from the low-frequency study to try to detect any small heating contribution from the ferritin (**Supplementary Fig. 4.S4**). These results confirm that ferritin does not produce significant heating, either at the bulk scale, or at the nanoscale, under RF-AMF up to tens of MHz in frequency.

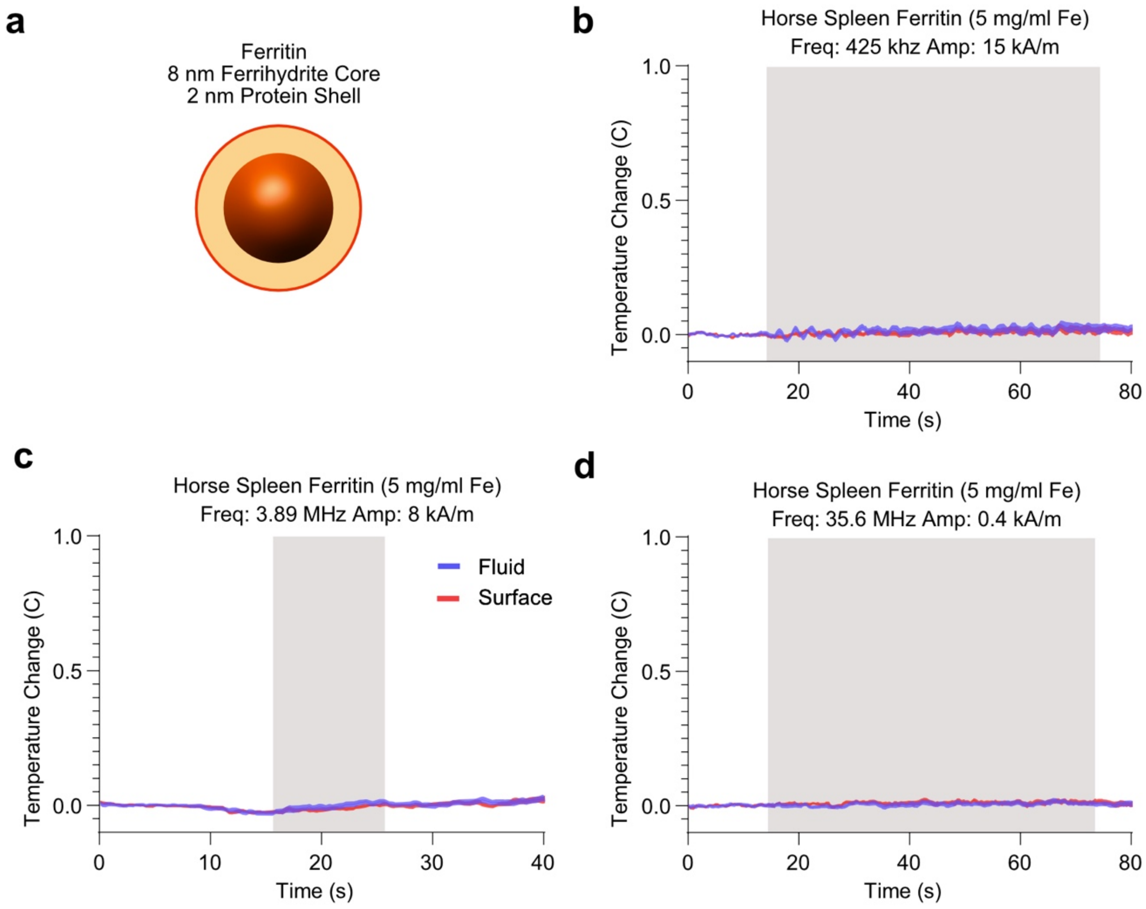

Figure 4.4 Ferritin shows no measurable heating in response to RF-AMF stimulation. a Diagram of the structure of ferritin, comprising a 2 nm-thick protein shell encapsulating a 6-8 nm ferrihydrite core. **b-d** Surface (red) and fluid (blue) temperature monitored for ferritin during RF-AMF application for three frequency regimes, as labeled in the figure. Each trace denotes the mean ± S.E.M. of 20 runs of RF-AMF stimulation. The RF-AMF application period is denoted by grey shading. A small (<.2 degrees C) temperature variation from the 440 kHz toroid was measured using a PBS blank and subtracted from **b** (see **Supplementary Fig. 4.S4**).

While our data with synthetic magnetic nanoparticles and ferritin strongly suggest that heat transfer from magnetic nanoparticles under RF-AMF is consistent with classical heat transfer theory, several previous studies using optical thermometry have suggested otherwise [10, 13, 15, 30]. To uncover possible sources of this discrepancy, we examined two potential sources of artifacts. First, several previous studies measured particle surface temperature with a thermochromic dye while measuring the bulk temperature with a physical thermometer placed in the solution [13, 15, 30]. We reasoned that the combined effects of the finite thermal mass of such a thermometer, even for a small phosphor or semiconductor-based thermal probe, and the thermal connection between the thermometer and the air outside the solution would cause its temperature response to underestimate the heating of the surrounding fluid during RF-AMF application, resulting in an apparent thermal gradient between the background fluid and the nanoparticle surface. To test this hypothesis, we immersed a 450-μm diameter thermal probe in a ferrofluid containing 10 mg/ml of the 10-nm Dylight 550-labeled magnetite nanoparticles and free DY521-XL dye (**Fig. 4.5a**). While the temperature response of the two dyes to RF-AMF matched within measurement error, the solid thermal probe temperature appeared to be lower (**Fig. 4.5b**). This artifact demonstrates the need for equivalency between the methods measuring the nanoparticle surface temperature and the surrounding fluid temperature.

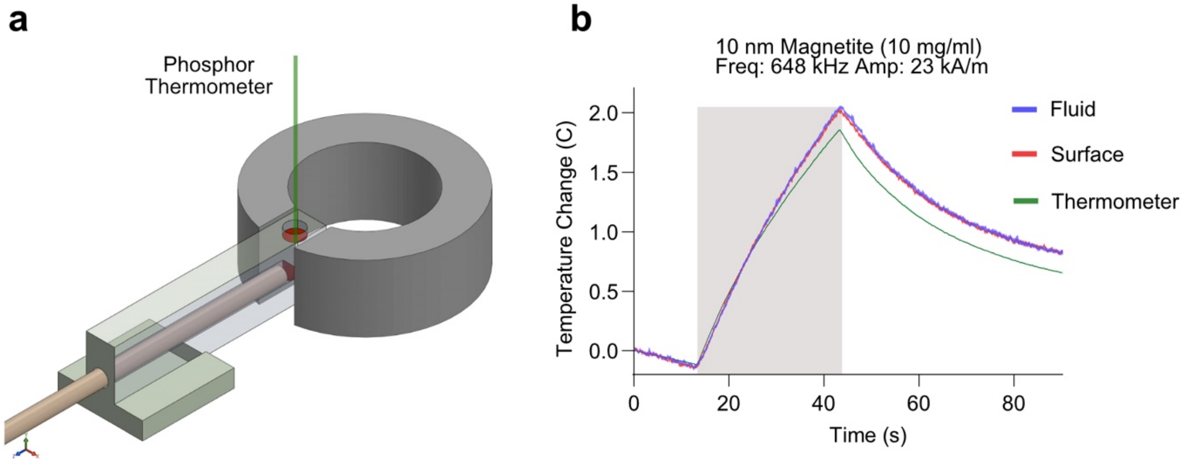

Figure 4.5 Artifactual measurement of enhanced surface heating due to the use of a solid thermal probe. **a** Diagram of experimental setup for measuring ferrofluid heating under RF-AMF that includes a solid thermal probe measurement of fluid temperature in addition to measurements of the particle surface and fluid using thermochromic dyes. **b** Temperature measured by our solid

thermal probe(green) and thermochromic measurements of temperature at the particle surface (red) and in the fluid (blue). Each trace denotes the mean ± S.E.M. of 20 runs of RF-AMF stimulation.

A second phenomenon reported in the literature involves a rapid, almost instantaneous, increase in the apparent particle surface temperature, followed by more gradual heating of the both the particle and the fluid [13, 30, 31]. We hypothesized that this observation could be caused by particle clustering due to inter-particle attraction under an applied field, especially in solutions of strongly magnetic particles. Particle clustering increases the scattering of both excitatory illumination and emitted light, which would manifest as a dip in the fluorescence of thermochromic probes (**Fig. 4.6a-c**). Since the probes' fluorescent output also decreases in response to increasing temperature, this dip in fluorescence could be misinterpreted as a jump in the temperature experienced by the dyes. To examine this effect, we reasoned that a DC field would cause clustering similar to the AC field applied during RF-AMF, without any particle heating. We ran a DC current through our gapped toroid inductor to produce a DC field comparable to the peak field of our 440 kHz AC signal. In a suspension of 20-nm magnetite particles at a concentration of 1 mg/ml, the measured fluorescence dropped immediately after the DC field is applied and recovered after the field was turned off (**Fig. 4.6d**). This effect would be even more pronounced at higher ferrofluid concentrations, where field-induced clustering would be more evident (**Supplementary Fig. 4.S6**). Such a concentration dependence would be particularly concerning as previous studies have used concentrations as high as 30 mg/ml [30]. In our experiments, the fluorescence of both dyes is affected similarly because our optical measurement is orthogonal to the magnetic field direction, such that the expected linear chain assembly of the magnetic particles [32, 33] does not preferentially shield the particle-bound dye from the light path (**Fig. 4.6e**). While both dyes in our system were affected similarly, previous studies comparing the response of a surface dye to an immersed thermometer would again arrive at the erroneous conclusion that there is a thermal gradient between the nanoparticle surface and the surrounding fluid.

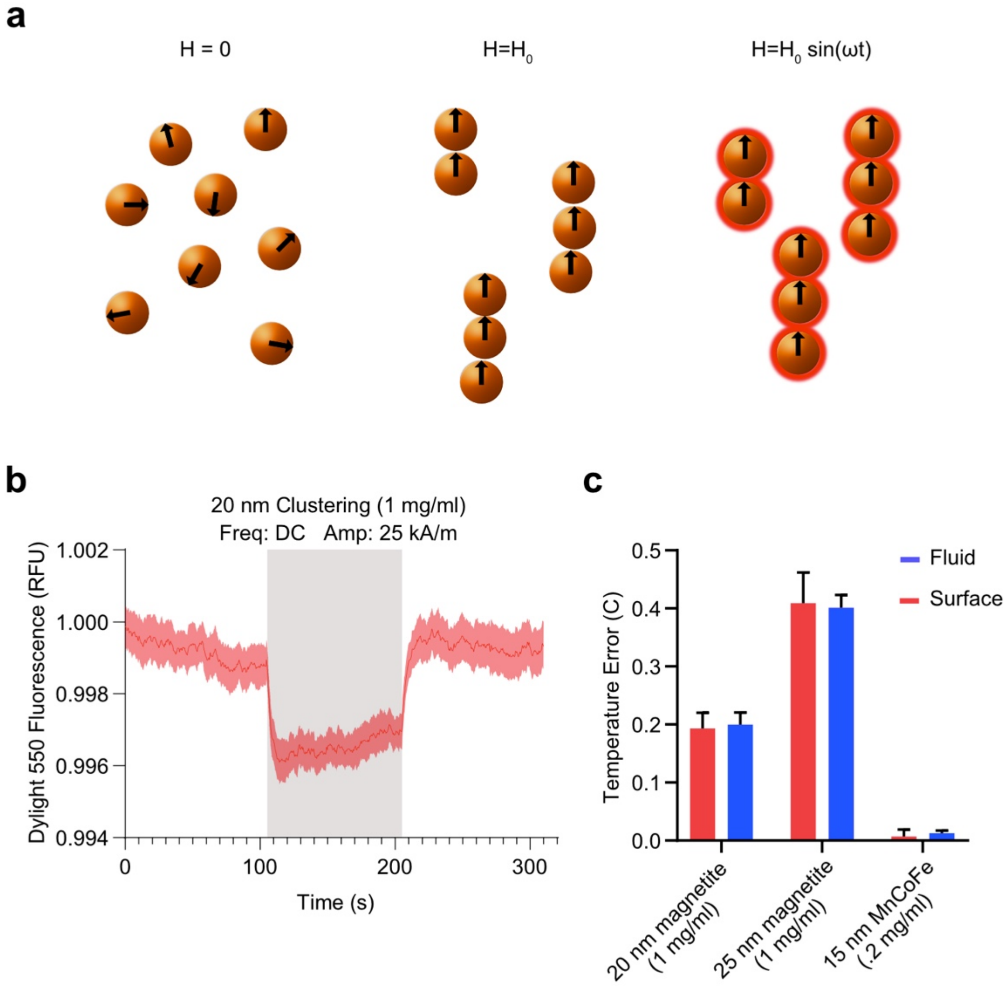

Figure 4.6 Artifact in optical thermometry due to nanoparticle clustering under applied field. a Diagram of superparamagnetic nanoparticle clustering without an applied magnetic field (left), with an applied DC field (middle) and with an applied AC field (right). Under both applied field conditions, the particles are expected to cluster into chains (see **Supplementary Fig. 4.S6**), with heating occurring under the AC field. Clustering is expected to increase with the particle concentration and with the strength of the applied field, H_0. In our optical setup, particle clustering is expected to diminish the measured fluorescence of both particle-bound and dissolved dyes. **b** Fluorescence of Dylight 550 bound to the surface of 20 nm nanoparticles during the application of a 25 kA/m DC field (stimulus period indicated with grey shading). Trace denotes the mean ± S.E.M. of 10 runs of

RF-AMF stimulation. **c** Apparent temperature jump due to the decreased fluorescence of the thermochromic dyes at the particle surface (red) and I the fluid (blue). Bars denote mean ± S.E.M. of 10 runs of RF-AMF stimulation.

Taken together, our results show that for several commonly used compositions of synthetic magnetic nanoparticles there is no significant difference between the surface temperature of the nanoparticle and the temperature of the surrounding fluid during RF-AMF stimulation. These findings are consistent with classical heat transfer theory and experiments conducted with other nanomaterials [34, 35], while contradicting several previous experimental results with SPIONs and demonstrating two potential sources of artifacts in optical temperature measurement. Several questions regarding the nanoscale phenomena involved in magnetic nanoparticles' response to RF-AMF remain unanswered. For example, our results do not directly address the temperature of the interior of the solid nanoparticle, as in some previous studies [14], though a much higher interfacial thermal resistance than measured for other nanoparticles [20, 23, 36] would be needed to produce a measurable difference in the interior temperature relative to surrounding fluid. In addition, given that the temporal resolution of our technique is substantially below the stimulus frequency, we would be unable to detect oscillating or transient thermal gradients, as might arise due to magnetocaloric effects. We consider such a phenomenon unlikely, since the thermal relaxation time of water is much faster than the stimulus frequency. Additionally, our study does not directly contradict, nor provides an explanation for, the preferential cleavage of thermolabile covalent bonds seen at the surface of magnetic nanoparticles under RF-AMF stimulation, as documented in several well-controlled studies [22, 37]. It is possible that such cleaveage is due to non-classical or non-thermal effects. Nevertheless, we believe our thermochromic dye readout corresponds closely to the scenario of nanoparticles or ferritin attached to temperature-sensitive ion channels. Thus, our experiments' inability to support the heat confinement mechanisms proposed to underlie the activtion of several magntogenetic constructs suggests that a re-examination of the mechanisms put forward in these reports may be warranted. Meanwhile, millimeter-scale heating of tissues by concentrated synthetic SPIONs remains a viable approach to magnetogenetic actuation consistent with Fourier's law [12, 15].

4.4 Supplementary Note: Monte Carlo Simulations

Monte Carlo simulation of the clustering of blocked magnetic nanoparticles. To demonstrate the effects of an applied magnetic field on the clustering of magnetic nanoparticles in a ferrofluid, we created a Monte Carlo simulation that allows blocked magnetic particles (no Neel relaxation) to rotationally and translationally diffuse and interact through magnetic dipole interactions under an applied bias field of 25 kA/m (31.35 mT). The simulation is carried out with finite time steps of $\delta t = 1ns$. Particles are modeled as hard spheres for rotational and translational diffusion by randomly displacing the particles in all three dimensions at each time step by

$$\delta x = N \cdot \frac{\pi}{2} \cdot \sqrt{2D_{trans}\delta t}$$

and rotating them in the two rotational degrees of freedom by

$$\delta\theta = N \cdot \tfrac{\pi}{2} \cdot \sqrt{2D_{rot}\delta t}.$$

Here $D_{trans} = \frac{k_b T}{6\pi\eta \cdot r_{np}}$ is the translational diffusion coefficient for a nanoparticle of radius r_{np}, $D_{rot} = \frac{k_b T}{6\pi\eta \cdot r_{np}^3}$ is the rotational diffusion coefficient, δt is the time step for the simulation which is set to 1 ns, and N is a random number chosen from the standard normal distribution. Magnetic force and torque on the j^th^ particle were calculated at each time step using the nanoparticle positions and orientations calculated in the previous time step as

$$\boldsymbol{F_j} = \sum_{i \neq j} \frac{3\mu_0}{4 * pi * r_{ij}^5} [(\boldsymbol{m_i} \cdot \boldsymbol{r_{ij}})\boldsymbol{m_j} + (\boldsymbol{m_j} \cdot \boldsymbol{r_{ij}})\boldsymbol{m_i} + (\boldsymbol{m_i} \cdot \boldsymbol{m_j})\boldsymbol{r_{ij}} - \frac{5(\boldsymbol{m_i} \cdot \boldsymbol{r_{ij}})(\boldsymbol{m_j} \cdot \boldsymbol{r_{ij}})}{r_{ij}^2} \boldsymbol{r_{ij}}]$$

and

$$\boldsymbol{\tau_j} = \boldsymbol{m_j} \times (\boldsymbol{B_{Bias}} + \textstyle\sum_{i \neq j} \boldsymbol{B_{ij}}).$$

Here $\boldsymbol{m}$ is the magnetic moment vector of the nanoparticle, $\boldsymbol{r_{ij}}$ is the displacement vector between the ith and jth particles, and $\boldsymbol{B_{ij}}$ is the magnetic field contribution from the ith particle at the position of the jth particle. Our simulation neglects inertial effects, so the magnetically driven displacement for each time step is calculated for the jth particle as

$$\delta \boldsymbol{x_j} = \frac{\boldsymbol{F_j} \cdot \delta t}{6\pi\eta r_{np}}.$$

The magnitude of the magnetically driven rotation of $\boldsymbol{m_j}$ about the axis of $\boldsymbol{\tau_j}$ is

$$\delta\theta = \frac{\tau_j \cdot \delta t}{8\pi\eta r_{np}^3}$$

Simulations were run on 100 nanoparticles with periodic boundary conditions, 1 ns time steps, and a total of 3 ms simulated time. Simulations were written in MATLAB.

4.5 Supplementary Figures

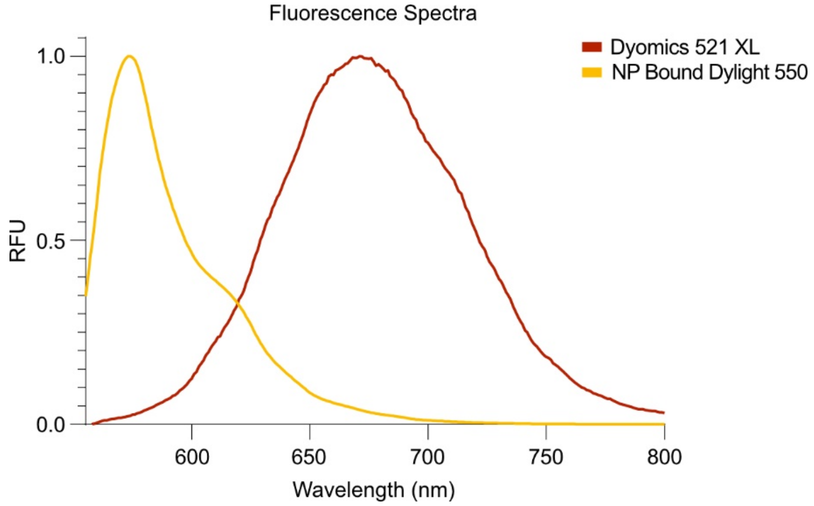

Supplementary Figure 4.S1 Fluorescence Spectra of Dylight 550 conjugated nanoparticles and DY-521XL. Spectra were measured in a Molecular Devices spectrophotometer. Excitation was set at 532 nm.

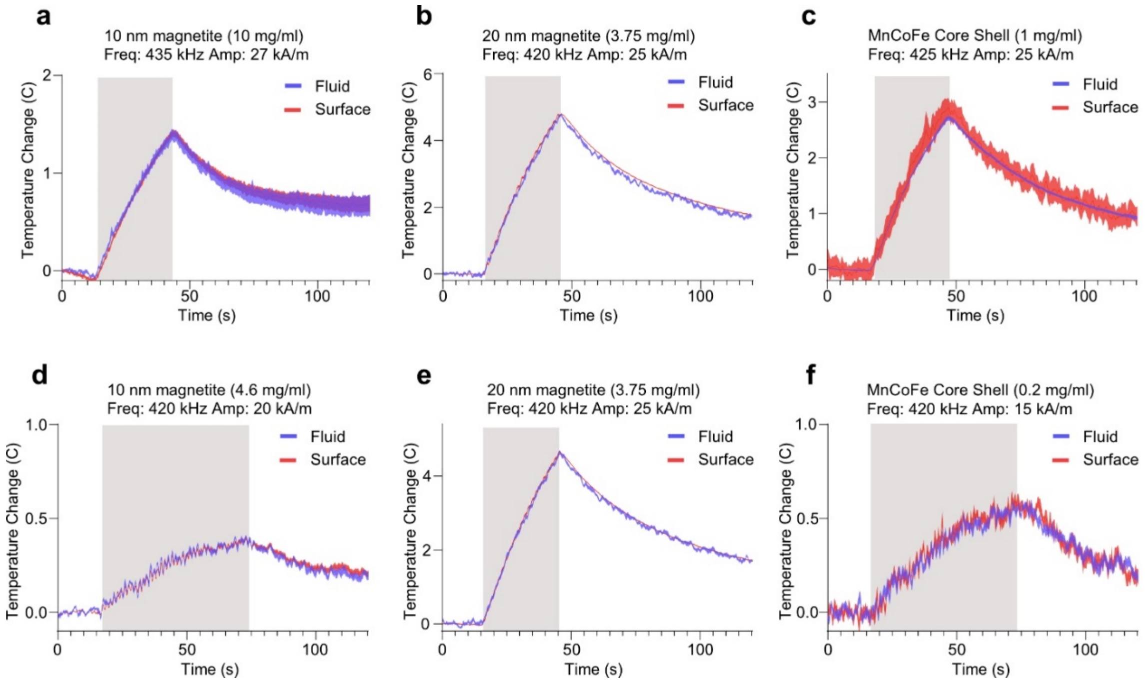

Supplementary Figure 4.S2 Additional hyperthermia trials with separate batches of magnetic particles. Surface and fluid temperatures measured for each nanoparticle type during RF-AMF application. Mean and SEM temperature for particle surface (red) and surrounding fluid (blue) are plotted for each sample, with frequency and field parameters specified above the plot. RF-AMF application period is denoted by grey shading. Each trace denotes the mean ± S.E.M. of 20 runs of RF-AMF stimulation.

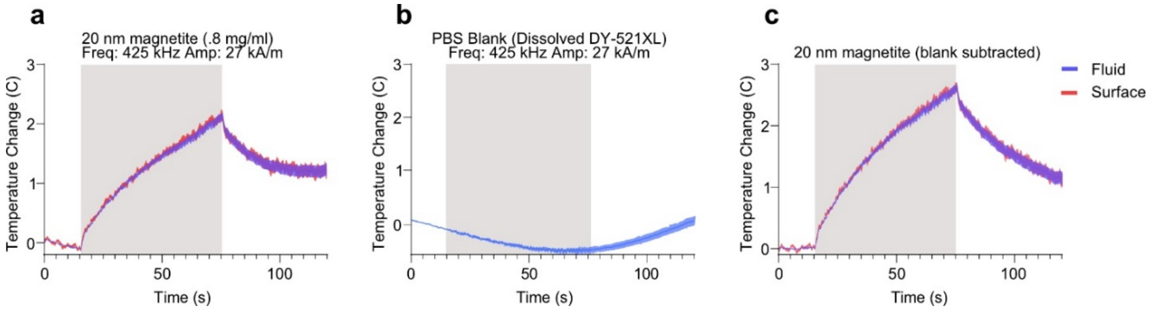

Supplementary Figure 4.S3 Artifact from background temperature variation due to the toroid. As stated in **Fig. 3** in the main text, our 400-700 kHz toroid did not completely cool in between stimuli, resulting in a slow apparent cooling at the beginning of the averaged plot. We hypothesized that the ferrofluid would easily reach thermal equilibrium with its surroundings over the nine minutes between stimuli, and as such, the slow cooling behavior of the toroid should be identical irrespective of the presence of nanoparticles in the sample. **a** Thermometry of 20 nm magnetite nanoparticle ferrofluid during RF-AMF application from **Fig. 4.3d. b** Thermometry of DY-521XL in PBS during RF-AMF application matching the field parameters in **a** establishes the background thermal variation of the sample due to the toroid. **c** Subtracting this background variation from the thermometry measurement of the ferrofluid under RF-AMF stimulus eliminates the slow cooling at the beginning of the trace. Mean and SEM temperature for particle surface (red) and surrounding fluid (blue) are plotted for each sample, with frequency and field parameters specified above the plot. RF-AMF application period is denoted by grey shading. Each trace denotes the mean ± S.E.M. of 20 runs of RF-AMF stimulation.

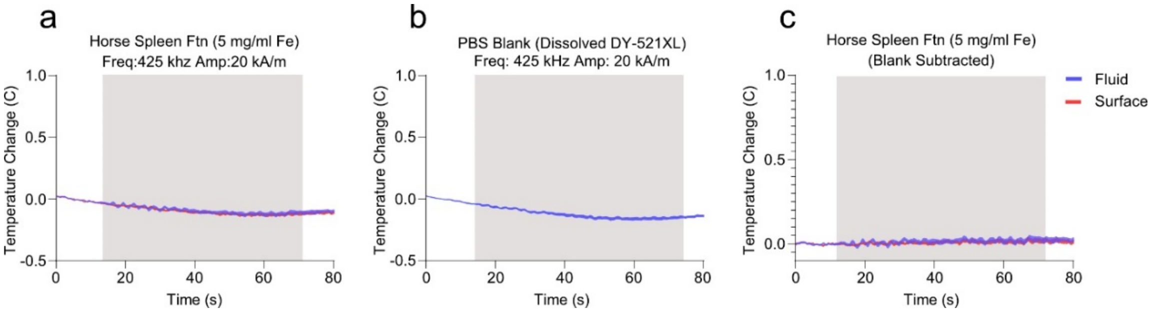

Supplementary Figure 4.S4 Background temperature variation in low frequency ferritin experiment. a Surface and fluid temperature of ferritin solution during RF-AMF application. Incomplete cooling of the toroid between stimuli leads to a slow cooling through RF-AMF stimulation in the ferritin ferrofluid. **b** Thermometry of DY-521XL in PBS during RF-AMF application matching the field parameters in **a** establishes the background thermal variation of the sample due to the toroid. **c** Subtracting background thermal variation from thermometry of ferritin under RF-AMF stimulation reveals no measurable heating from ferritin on the protein surface or in the surrounding fluid. Mean and SEM temperature for particle surface (red) and surrounding fluid (blue) are plotted for each sample, with frequency and field parameters specified above the plot. RF-AMF application period is denoted by grey shading. Each trace denotes the mean ± S.E.M. of 20 runs of RF-AMF stimulation.

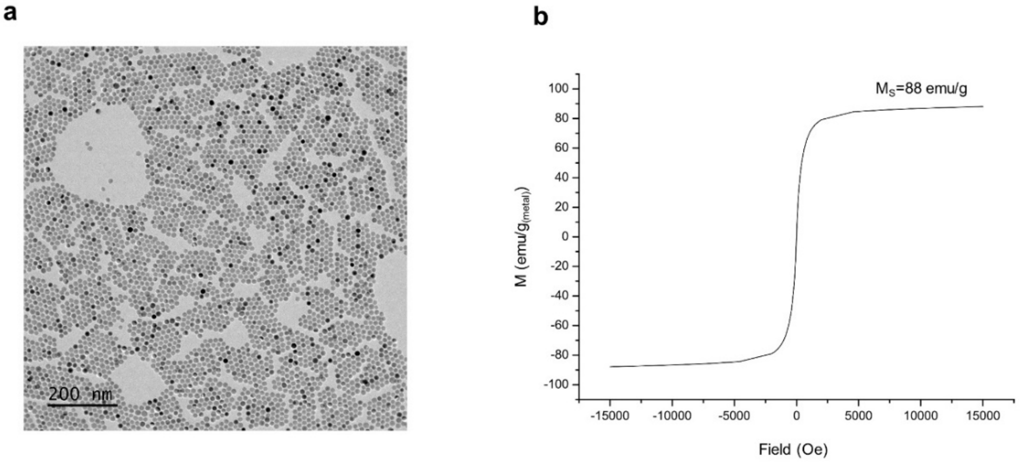

Supplementary Figure 4.S5 Characterization of core-shell nanoparticles. a Transmission electron microscope (TEM) image and **b** magnetic measurement of core-shell nanoparticles. TEM observation were made using the JEM-2100Plus (JEOL) under the acceleration voltage of 200 kV. Magnetic property was measured using vibrating sample magnetometer (Lake Shore Cryotronics, Inc.) and mass of metal was measured using inductively-coupled plasma optical emission spectroscopy (Thermofisher).

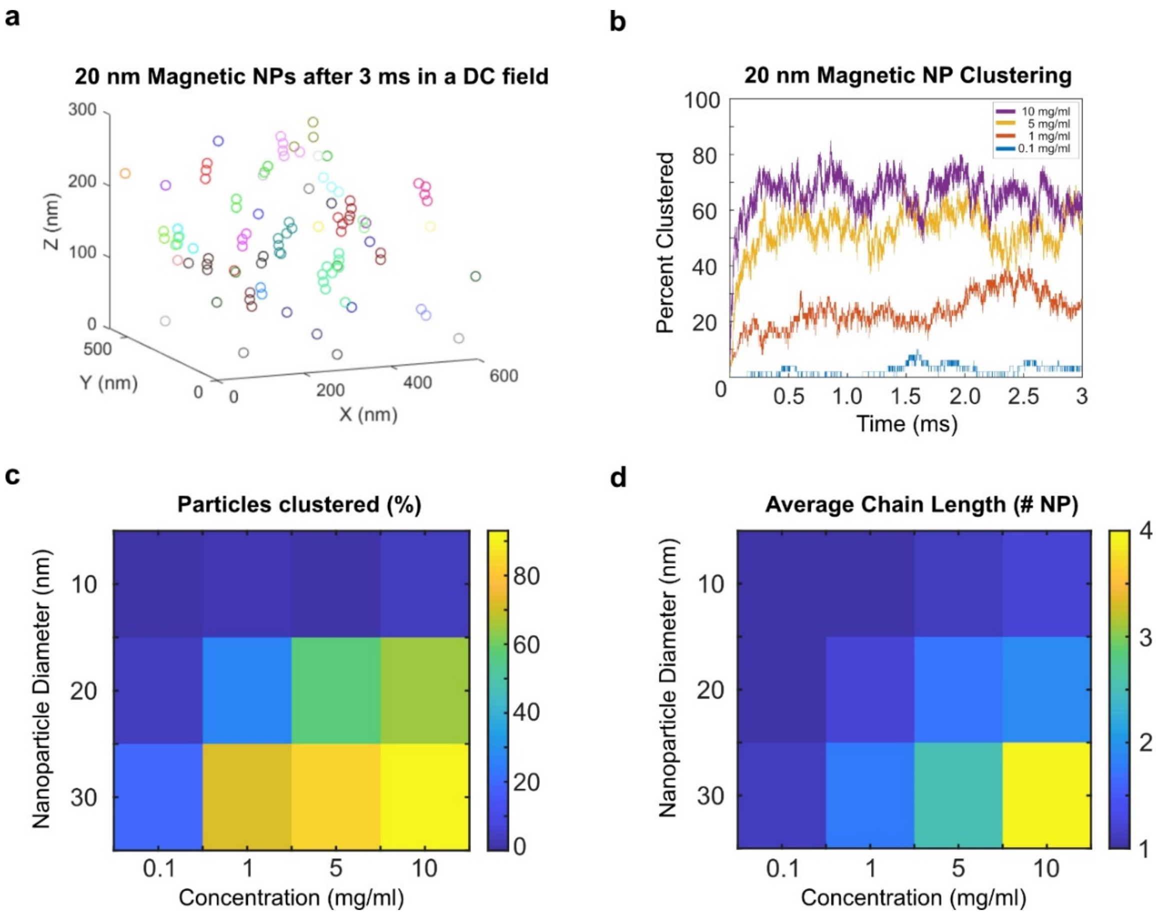

Supplementary Figure 4.S6 Monte Carlo Simulation of magnetic nanoparticle clustering in a bias field. a Chains of 20 nm magnetic nanoparticles formed after applying a 25 kA/m bias field in the +z direction for 3 ms. The particles in this simulation were at a concentration of 10 mg/ml. **b** Percent of particles that have clustered with at least one other particle as a function of time after the onset of a 25 kA/m DC bias field in a 10 mg/ml ferrofluid of 20 nm particles. **c** Percent of particles that have clustered with at least one other particle after 3 ms in a 25 kA/m bias field as a function of concentration and particle diameter. **d** Average chain size after 3 ms in a 25 kA/m bias field as a function of concentration and particle diameter. Particle density and mass magnetization is 5.17 g/cc and 80 emu/g for all simulations.

4.6 Supplementary Tables

	20 nm	10 nm	CS
Fraction D550 Signal in FT	0.181	0.003	0.089
Max Release Induced Error (K)	0.005	<.001	0.009

Table 4.S1. Error from dye release for 20 nm magnetite (20 nm), 10 nm magnetite (10 nm), and MnCoFe core-shell nanoparticles (CS). A small amount of nonspecifically bound Dylight 550 was released from the nanoparticle surface during stimulus. Due to the strong quenching of dye conjugated to the nanoparticle surface, this released Dylight 550 can account for a substantial fraction of the overall measured Dylight 550 fluorescence. In order to ensure that this did not confound our results, we measured the fractional contribution of released Dylight 550 to the overall Dylight 550 signal. We did so by separating the nanoparticle-bound dye from dissolved dye after completion of the standard RF-AMF stimulus (20 one-min stimuli at 420 kHz and 25 kA/m with 9 min in between stimuli) for each synthetic magnetic particle sample type using 10 kDa size exclusion filters (Amicon). The retentate was diluted with PBS to match the original particle concentration. An equivalent concentration of unlabeled nanoparticles was added to the flow-through to account for the nanoparticle's optical attenuation. The fluorescence of the retentate and flow through (FT in table) were then measured at 570 nm (530 nm excitation) using a Molecular Devices spectrophotometer. Assuming the nanoparticle surface and surrounding fluid maintained two distinct temperatures, the overall Dylight 550 signal would be a weighted

average of the two environments. As a result, it is possible to approximate the error induced by the released dye:

$$Dylight\ Temp. = (1 - Released\ Frac.) * Surface\ Temp + Released\ Frac. * DY521\ Temp.$$

$$Surface\ Temp. = (Dylight\ Temp. - Released\ Frac. * DY521\ Temp)/(1 - Released\ Frac.)$$

$$Max\ Error = \max\{Surface\ Temp. - Dylight\ Temp.\}$$

Here *Dylight 550 Temp.* is the Dylight 550 temperature measured in our fluorometer during RF-AMF application, *Released Frac.* is the fraction of the total D550 signal in the flow through after size-exclusion filtration, *DY521 Temp.* is the DY-521XL temperature measured during RF-AMF application, and *Surface Temp.* is the actual temperature at the nanoparticle surface.

Bibliography

1. Giustini, A.J. et al. MAGNETIC NANOPARTICLE HYPERTHERMIA IN CANCER TREATMENT. *Nano LIFE* **1** (2010).
2. Brown, W.F. Thermal Fluctuations of a Single-Domain Particle. *Physical Review* **130**, 1677-1686 (1963).
3. Landau, L. & Lifshitz, E. in Perspectives in Theoretical Physics. (ed. L.P. Pitaevski) 51-65 (Pergamon, Amsterdam; 1992).
4. Rosensweig, R.E. Heating magnetic fluid with alternating magnetic field. *Journal of Magnetism and Magnetic Materials* **252**, 370-374 (2002).
5. Sukhov, A. & Berakdar, J. Temperature-dependent magnetization dynamics of magnetic nanoparticles. *Journal of Physics: Condensed Matter* **20**, 125226 (2008).
6. Stoner Edmund, C. & Wohlfarth, E.P. A mechanism of magnetic hysteresis in heterogeneous alloys. *Philosophical Transactions of the Royal Society of London. Series A, Mathematical and Physical Sciences* **240**, 599-642 (1948).
7. Usadel, K.D. & Usadel, C. Dynamics of magnetic single domain particles embedded in a viscous liquid. *Journal of Applied Physics* **118**, 234303 (2015).
8. Nowak, U., Mryasov, O., Wieser, R., Guslienko, K. & Chantrell, R. Spin dynamics of magnetic nanoparticles: Beyond Brown's theory, Vol. 72. (2005).
9. Chalopin, Y., Bacri, J.-C., Gazeau, F. & Devaud, M. Nanoscale Brownian heating by interacting magnetic dipolar particles. *Scientific Reports* **7**, 1656 (2017).
10. Huang, H., Delikanli, S., Zeng, H., Ferkey, D.M. & Pralle, A. Remote control of ion channels and neurons through magnetic-field heating of nanoparticles. *Nature Nanotechnology* **5**, 602 (2010).
11. Stanley, S.A. et al. Radio-Wave Heating of Iron Oxide Nanoparticles Can Regulate Plasma Glucose in Mice. *Science* **336**, 604-608 (2012).
12. Chen, R., Romero, G., Christiansen, M.G., Mohr, A. & Anikeeva, P. Wireless magnetothermal deep brain stimulation. *Science* **347**, 1477-1480 (2015).
13. Piñol, R. et al. Joining Time-Resolved Thermometry and Magnetic-Induced Heating in a Single Nanoparticle Unveils Intriguing Thermal Properties. *ACS Nano* **9**, 3134-3142 (2015).
14. Dong, J. & Zink, J.I. Taking the Temperature of the Interiors of Magnetically Heated Nanoparticles. *ACS Nano* **8**, 5199-5207 (2014).
15. Munshi, R. et al. Magnetothermal genetic deep brain stimulation of motor behaviors in awake, freely moving mice. *eLife* **6**, e27069 (2017).
16. Stanley, S.A., Sauer, J., Kane, R.S., Dordick, J.S. & Friedman, J.M. Remote regulation of glucose homeostasis in mice using genetically encoded nanoparticles. *Nature Medicine* **21**, 92 (2014).
17. Meister, M. Physical limits to magnetogenetics. *eLife* **5** (2016).
18. Berciaud, S., Lasne, D., Blab, G.A., Cognet, L. & Lounis, B. Photothermal heterodyne imaging of individual metallic nanoparticles: Theory versus experiment. *Physical Review B* **73**, 045424 (2006).
19. Honda, M., Saito, Y., Smith, N.I., Fujita, K. & Kawata, S. Nanoscale heating of laser irradiated single gold nanoparticles in liquid. *Opt. Express* **19**, 12375-12383 (2011).

20. Merabia, S., Shenogin, S., Joly, L., Keblinski, P. & Barrat, J.-L. Heat transfer from nanoparticles: A corresponding state analysis. *Proceedings of the National Academy of Sciences* **106**, 15113 (2009).
21. Baral, S., Rafiei Miandashti, A. & Richardson, H.H. Near-field thermal imaging of optically excited gold nanostructures: scaling principles for collective heating with heat dissipation into the surrounding medium. *Nanoscale* **10**, 941-948 (2018).
22. Romero, G., Christiansen, M.G., Stocche Barbosa, L., Garcia, F. & Anikeeva, P. Localized Excitation of Neural Activity via Rapid Magnetothermal Drug Release. *Advanced Functional Materials* **26**, 6471-6478 (2016).
23. Ge, Z., Cahill, D.G. & Braun, P.V. AuPd Metal Nanoparticles as Probes of Nanoscale Thermal Transport in Aqueous Solution. *The Journal of Physical Chemistry B* **108**, 18870-18875 (2004).
24. Shin, T.-H. et al. A magnetic resonance tuning sensor for the MRI detection of biological targets. *Nat. Protoc.* **13**, 2664 (2018).
25. Chen, R., Christiansen, M.G. & Anikeeva, P. Maximizing hysteretic losses in magnetic ferrite nanoparticles via model-driven synthesis and materials optimization. *ACS Nano* **7**, 8990-9000 (2013).
26. Harrison, P. The ferritins: molecular properties, iron storage function and cellular regulation. *Biochimica et Biophysica Acta (BBA) - Bioenergetics* **1275**, 161-203 (1996).
27. Koralewski, M., Pochylski, M. & Gierszewski, J. Magnetic properties of ferritin and akaganeite nanoparticles in aqueous suspension. *Journal of nanoparticle research : an interdisciplinary forum for nanoscale science and technology* **15**, 1902-1902 (2013).
28. Schäfer-Nolte, E. et al. Tracking Temperature-Dependent Relaxation Times of Ferritin Nanomagnets with a Wideband Quantum Spectrometer. *Physical Review Letters* **113**, 217204 (2014).
29. Fantechi, E. et al. A Smart Platform for Hyperthermia Application in Cancer Treatment: Cobalt-Doped Ferrite Nanoparticles Mineralized in Human Ferritin Cages. *ACS Nano* **8**, 4705-4719 (2014).
30. Polo-Corrales, L. & Rinaldi, C. Monitoring iron oxide nanoparticle surface temperature in an alternating magnetic field using thermoresponsive fluorescent polymers. *Journal of Applied Physics* **111**, 07B334 (2012).
31. Huang, H., Delikanli, S., Zeng, H., Ferkey, D.M. & Pralle, A. Remote control of ion channels and neurons through magnetic-field heating of nanoparticles. *Nature Nanotechnology* **5**, 602-606 (2010).
32. Wilson, R.J. et al. Formation and properties of magnetic chains for 100 nm nanoparticles used in separations of molecules and cells. *Journal of magnetism and magnetic materials* **321**, 1452-1458 (2009).
33. Branquinho, L.C. et al. Effect of magnetic dipolar interactions on nanoparticle heating efficiency: Implications for cancer hyperthermia. *Scientific Reports* **3**, 2887 (2013).
34. Paulo, P.M.R. et al. Photothermal Correlation Spectroscopy of Gold Nanoparticles in Solution. *The Journal of Physical Chemistry C* **113**, 11451-11457 (2009).
35. Gupta, A., Kane, R.S. & Borca-Tasciuc, D.-A. Local temperature measurement in the vicinity of electromagnetically heated magnetite and gold nanoparticles. *Journal of Applied Physics* **108**, 064901 (2010).

36. Ge, Z., Kang, Y., Taton, T.A., Braun, P.V. & Cahill, D.G. Thermal Transport in Au-Core Polymer-Shell Nanoparticles. *Nano Letters* **5**, 531-535 (2005).
37. Riedinger, A. et al. Subnanometer Local Temperature Probing and Remotely Controlled Drug Release Based on Azo-Functionalized Iron Oxide Nanoparticles. *Nano Letters* **13**, 2399-2406 (2013).